NORTHWESTERN UNIVERSITY

Achiral Noncentrosymmetric Racemates

A DISSERTATION

SUBMITTED TO THE GRADUATE SCHOOL

IN PARTIAL FULFILLMENT OF THE REQUIREMENTS

for the degree

DOCTOR OF PHILOSOPHY

Field of Chemistry

By

Matthew Lander Nisbet

EVANSTON, ILLINOIS

June 2021

ABSTRACT

Achiral Noncentrosymmetric Racemates

Matthew Lander Nisbet

Chirality and polarity describe orthogonal mechanisms of inversion symmetry breaking, which is the origin of valuable properties in crystalline materials including nonlinear optical activity, ferroelectricity, and piezoelectricity. Noncentrosymmetric (NCS) materials have numerous applications yet opportunities remain for cooperative coupling between chiral and polar basic building units to realize high-performance materials. Enantiomerically pure samples of chiral molecules have been exploited as structure-directing agents based on the fact that a single enantiomer must crystallize without inversion symmetry. However, this strategy does not control the bulk polarity, which is required for ferroelectricity and associated with superior nonlinear optical properties, meaning that additional studies are needed to optimize interactions between chiral and polar structural moieties. Racemic compounds, which contain both enantiomers of a chiral molecule, offer an underappreciated opportunity for achieving noncentrosymmetry in crystalline solids.

In this work, we describe our efforts to arrange polar building units, namely d^0 early transition metal fluorides and oxide-fluorides, and racemic combinations of chiral Δ- and Λ-$Cu(bpy)_2(H_2O)^{2+}$ building units in achiral NCS structures via hydrothermal synthesis.

Our investigation found that hydrogen bonding and nonparallel $\pi - \pi$ stacking dictate inversion symmetry breaking in the $[Cu(bpy)_2(H_2O)][MF_6]\cdot 1.5H_2O$ (M = Ti, Zr, Hf; bpy = 2,2'-bpiyridine; space group: $Pna2_1$) structural family.

The first step of this study was finding the appropriate set of conditions to synthesize the Ti- and Zr- analogues of the compound $[Cu(bpy)_2(H_2O)][HfF_6]\cdot 1.5H_2O$. Our investigation of the relevant composition space revealed a phase competition between the NCS compounds and centrosymmetric compounds with the general formula $[Cu(bpy)(H_2O)_2(MF_6)]_n$ (M = Ti, Zr, Hf) in each system that is strongly dependent on the identity of the early transition metal ion. Machine learning modeling was applied to generate an interpretable decision tree model which indicates that phase selection is driven primarily by the bpy:Cu molar ratio for reactions containing Zr or Hf and captures the additional requirement that the amount of HF present be decreased to raise the pH for reactions containing Ti. Ligand K-edge X-ray absorption spectroscopy allowed for the observation of strong ligand-to-metal π bonding that is unique to the TiF_6^{2-} anion among the M = Ti, Zr, Hf series.

Next, a series of compounds with the general formula $[Cu(phen)_2(H_2O)][MF_6]\cdot xH_2O$ (M = Ti, Zr, Hf ; phen = 1,10-phenanthroline) was synthesized to probe the role of $\pi-\pi$ stacking interactions in the $[Cu(bpy)_2(H_2O)][HfF_6]\cdot 1.5H_2O$ (M = Ti, Zr, Hf) system by comparing the intermolecular interactions of $Cu(phen)_2(H_2O)^{2+}$ and $Cu(bpy)_2(H_2O)^{2+}$ complexes. This study demonstrated that local inversion symmetry breaking by non-parallel heterochiral $\pi-\pi$ stacking is a necessary but insufficient condition for inversion symmetry breaking.

Finally, two additional centrosymmetric compounds, $[Cu(bpy)_2(H_2O)][SiF_6]\cdot 4H_2O$ and $[Cu(bpy)(H_2O)_2(SnF_6)]_n$, were synthesized to compare the main group anions SiF_6^{2-} and SnF_6^{2-} to their group IV early transition metal counterparts. The SiF_6^{2-} anion was found to direct the Δ- and Λ-$Cu(bpy)_2(H_2O)^{2+}$ complexes to adopt distinct hydrogen bonding

networks and homochiral $\pi - \pi$ stacking owing to the increased amount of hydrating water relative to the polar $[Cu(bpy)_2(H_2O)][MF_6]\cdot 1.5H_2O$ (M = Ti, Zr, Hf) phase. In contrast, $[Cu(bpy)(H_2O)_2(SnF_6)]_n$ is isostructural to $[Cu(bpy)(H_2O)_2(HfF_6)]_n$.

Thesis Advisor: Kenneth R. Poeppelmeier

Acknowledgments

First, I would like to thank my research advisor, Prof. Kenneth Poeppelmeier, for his invaluable guidance and generous kindness over the years. Learning about solid-state chemistry with a mentor and friend like Ken has been an incredible experience and has made me a better researcher, writer, and teacher.

I thank my committee members, Prof. Mercouri Kanatzidis and Prof. James Rondinelli for their insights, feedback, and time over the course of my thesis. I would also like to thank Prof. Omar Farha for serving as the chair of my qualify exam committee.

Science is a team sport, and it has been an immense privilege to work with an amazing ensemble of people during my time in Poeppelmeier lab. I especially thank Allison Wustrow and Fenghua Ding for their mentorship and friendship throughout graduate school. I also thank Emily Hiralal for her curiosity and dedication since joining the group. I thank Ella Wang for being my oxide-fluorides partner-in-crime. I thank Kent Griffith for his guidance, Steven Flynn and Justin Hancock for being outstanding downstairs office-mates, and Ryan Paull and Zach Mansley for their humor and willingness to play soccer with me. In addition, I am incredibly thankful to have had the opportunity to work and share many fond memories with Chi Zhang, Jaye Harada, Robert Kennedy, Emily Greenstein, Ian Peczak, Michael Yeung, Jackie Cantwell, and Anita Chen.

I thank Prof. Alex Norquist and Dr. Ian Pendleton of Haverford College as well as Prof. Jordi Cabana and Dr. Gene Nolis from the University of Illinois at Chicago for fruitful and

enjoyable collaboration. I thank Charlotte Stern and Christos Malliakas for teaching me many aspects of X-ray diffraction and for their helpful advice during my visits to IMSERC.

I consider myself to be incredibly fortunate to have worked with excellent research advisors prior to coming to Northwestern, including Prof. R.J. Hinde and my graduate student mentor Dr. Ashleigh Barnes at the University of Tennessee, Knoxville, and Prof. John Anthony at the University of Kentucky.

I am deeply indebted to the Centre College community for their support and guidance. I thank the James Graham Brown Foundation for giving me the opportunity to explore my interests and engage in scientific research. I am immensely grateful to the many teachers and mentors from my time at Centre who prepared me for the path ahead.

Outside of lab, I thank the friends with whom many adventures have been shared. I especially thank Suyog Padgaonkar, Nathan Flanders, Dawning Liu, and Daylan Sheppard for their fellowship in Rogers Park. I thank all of the teammates who shared the championships won (and many more lost) on the soccer field with me as part of the Give 'Em El soccer team. I would also like to thank Christian Contreras for allowing me to win several free t-shirts with the Peanuts ultimate frisbee team. I would also like to thank the other members of my cohort, including Jake Rothbaum, Shawn Zhao, Justin Hoffman, Becca McClain, Alex Tamerius, Ariel Leonard, Elamar Hakim Moully, Naomi Dalchand, Sarah Anderson, Nic Watkins, Sylvia Hanna, and many others whose friendship has been invaluable throughout graduate school.

Most importantly, I thank my family, Mom, Dad, Will, and Sarah, for their ardent support despite my failures to explain what exactly it is that I do. I thank Maggie for being a constant source of joy in my life. I thank my grandparents, cousins, aunts, and uncles for their support every step of the way, for which I am extremely grateful.

Finally, I would like to thank the National Science Foundation for providing financial support for my graduate research under DMR-1904701. Single-crystal and powder X-ray diffraction data and solid-state NMR spectra were acquired at IMSERC at Northwestern University, which has received support from the Soft and Hybrid Nanotechnology Experimental (SHyNE) Resource (NSF ECCS-1542205), the State of Illinois, the International Institute for Nanotechnology (IIN), and the National Science Foundation (DMR-0521267). This work made use of the J. B. Cohen X-ray Diffraction Facility supported by the MRSEC program of the National Science Foundation (DMR-1720139).

List of Abbreviations

CS: centrosymmetric

ETM: early transition metal

NCS: noncentrosymmetric

NLO: nonlinear optical

SOJT: second-order Jahn–Teller

XAS: X-ray absorption spectroscopy

XRD: X-ray diffraction

Table of Contents

List of Tables

List of Figures

CHAPTER 1

Introduction

1.1. Symmetry in Racemic Compounds

Polarity and chirality are orthogonal mechanisms of inversion symmetry breaking that lead to useful properties in noncentrosymmetric (NCS) solids, which lack crystallographic inversion symmetry.[1,2] As summarized in Figure 1.1, broken inversion symmetry allows for properties such as second-order nonlinear optical activity (including second harmonic generation), piezoelectricity, pyroelectricity, ferroelectricity, circular dichroism, and optical rotation. Given the technological utility of these properties, the design and synthesis of NCS materials is of immense interest to the solid-state chemistry community. Despite the ubiquity of chirality and polarity in cutting-edge NCS materials, the opportunity remains for the development of functional materials that rely on the synergistic combination of chiral and polar entities to achieve enhanced properties and potentially novel functionality .

The introduction of chiral species in crystalline materials imparts certain limitations on the symmetry of the resulting structure because chiral molecules cannot occupy sites that are inversion symmetric. The most extreme example of a restriction of this kind is found in the case of enantiomerically pure samples (containing molecules which all share the same handedness), which must crystallize in enantiomorphic NCS point groups. Although great strides have been made to realize ferroelectric and nonlinear optical materials following this approach,[3–16] obtaining enantiomerically pure samples of chiral molecules presents a distinct experimental challenge.[17] The vast majority of reactions which produce a chiral center are

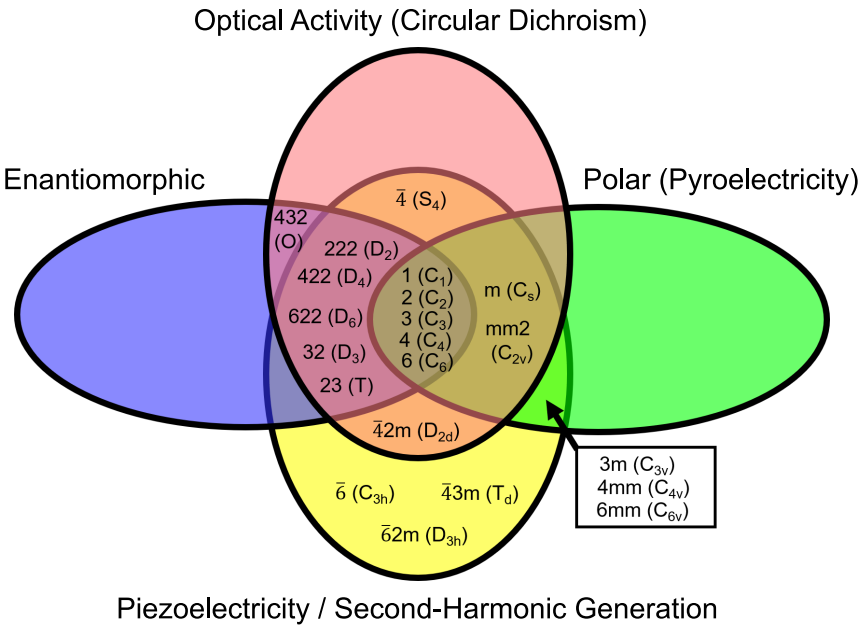

Figure 1.1. Visual summary of the symmetry-dependent structure-property relationships in NCS materials. Adapted from (Halasyamani and Poeppelmeier, 1998).

not stereoselective, meaning that racemic mixtures, which contain equal numbers of both enantiomers, of chiral reagents are commonly generated *in situ* whereas enantiomerically pure samples of chiral reagents require tedious separation or resolution. Further, controlling the alignment of polar building units remains as an obstacle for discovering new technologically useful NCS materials even when enantiomerically pure reagents are involved, as the crystallization of polar units in the presence of chiral molecules can result in nonpolar or weakly polar structures.[18–21] Here, we seek to expand the set of known NCS compounds by using racemic mixtures of chiral molecules rather than enantiomerically pure samples to form NCS structures. The ability to align polar units with racemic combinations of chiral units would circumvent the limitations of relying on enantiomerically pure chiral molecules and provide fundamental insight toward controlling interactions between chirality and polarity in the solid state to optimize the alignment of polar groups.[22,23]

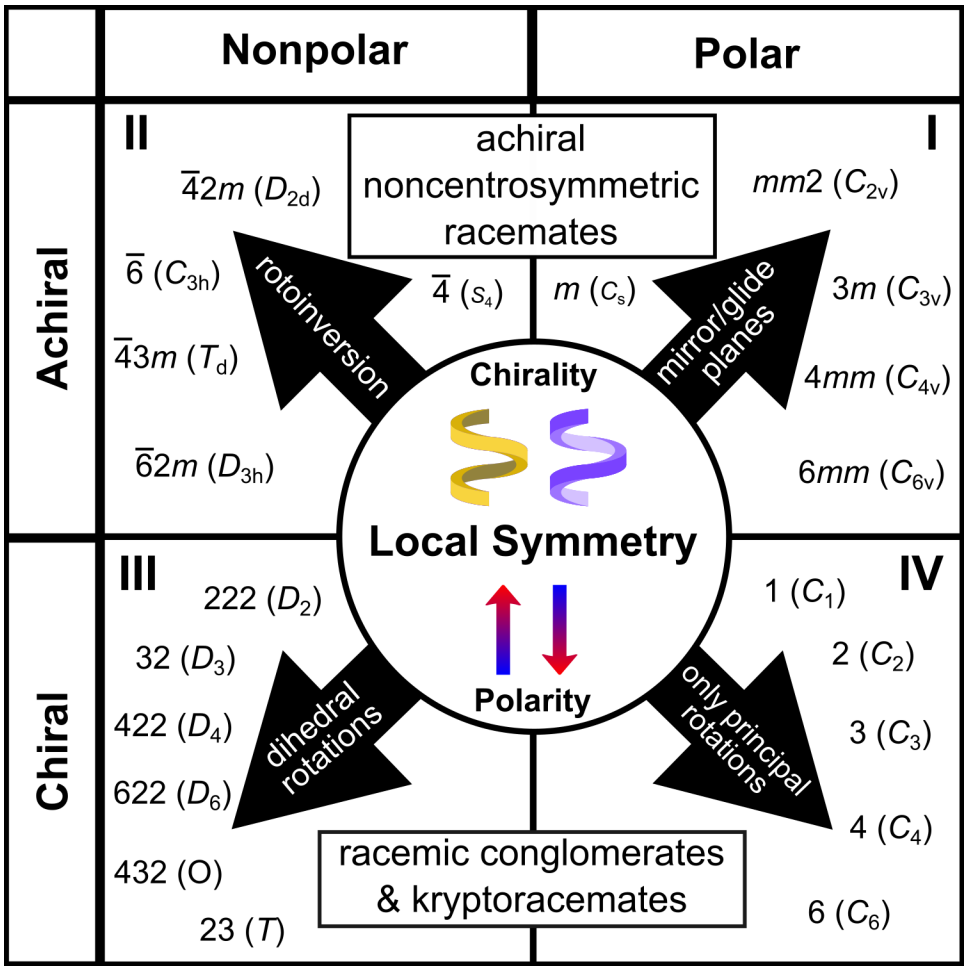

Figure 1.2. Schematic representation of symmetry relationships between chiral molecules in racemic compounds. Inversion symmetry breaking in racemates occurs when opposite enantiomers are related only by mirror planes, glide planes, or rotoinversion. Adapted from (Gautier, 2012) and (Halasyamani and Poeppelmeier, 1998).

Racemates, or racemic compounds, are defined as compounds in which opposite enantiomers are related by symmetry. Racemic compounds may only crystallize in point groups that include improper symmetry operations, which can relate enantiomers: inversion centers, mirror/glide planes, and rotoinversion axes.[24,25] While the most common crystallization outcome from racemic mixture is the formation of a centrosymmetric racemic compound, several

cases allow for crystallization without inversion symmetry, as show in Figure 1.2. Quadrants I and II represent the class of achiral noncentrosymmetric (AN) racemates, which is the primary focus of the present work. AN racemates are an understudied group of materials that possess potential for useful functionality.[26] These AN racemic compounds are permitted by symmetry to possess properties that are dependent on broken inversion symmetry, including surprising optical activity, which is conventionally thought to be forbidden in racemic compounds. Although many examples of AN racemic organic compounds have been identified from the Cambridge Structural Database, the rational synthesis of AN racemates remains a challenge as such compounds are typically formed serendipitously. For example, the amino acids are among the most studied molecules and yet no clear rationalization exists for why DL-alanine and DL-tyrosine crystallize in NCS structures while the other eighteen amino acids crystallize with centrosymmetry.[27–29] DL-alanine is an especially notable example because the racemate displays higher SHG efficiency than its single-enantiomer counterparts as well as promising piezoelectric properties.[30–32]

Quadrants III and IV of Figure 1.2 contain two distinct classes of compounds: racemic conglomerates and kryptoracemates. A racemic conglomerate is defined as a physical mixture of enantiomorphic crystals with an equal number of crystals containing each enantiomer. Although racemic conglomerates display NCS structures, the situation is analogous to that of separating a racemic mixture in solution in that great care must be taken to isolate each enantiomer. Kryptoracemates are rare compounds characterized by the incorporation of molecules of two different handednesses within the same crystal that are not related by crystallographic symmetry.[33–35] In this case, although a clear parallel exists between kryptoracemates and racemic compounds, the chiral molecules do not precisely meet the definition of enantiomers, which stipulates that the molecules with opposite chirality be

mirror images, and therefore kryptoracemates are not considered as racemic compounds within the scope of this work.

Symmetry breaking in the AN racemate $[Cu(bpy)_2(H_2O)]_2[HfF_6]_2{\cdot}3H_2O$ (Hf-NCS) (bpy = 2,2'-bipyridine) offers a new route to control the polar alignment of distorted early transition metal (ETM) fluorides and oxide-fluorides with racemic combinations of chiral build units.[22] Hf-NCS is a molecular crystal containing weakly polar HfF_6^{2-} units and a racemic combination of Δ- and Λ-$[Cu(bpy)_2(H_2O)]^{2+}$ units. By symmetry this material is achiral but optically active, representing an unconventional case of an optically active racemate. The goal of the present investigation is to connect molecular and crystallographic symmetry to elucidate the factors that distinguish compounds that crystallize in each of the four quadrants show in Figure 1.2 as well as those that crystallize with inversion symmetry.

1.2. Second-order Jahn-Teller Effects in Early Transition Metal Fluorides and Oxide-Fluorides

Following the theory of anionic groups developed by Chen, the majority contribution to nonlinear susceptibility, which describes the efficiency of polarization-dependent properties in NCS materials, comes from mobile electrons found in anionic groups, whereas electrons of cations are more tightly bound and therefore make negligible contributions to the nonlinear susceptibility.[36,37] Thus, controlling the arrangement of anionic groups is the first priority in the design of functional NCS solids. Here, we examine the crystal chemistry of distorted d^0 ETM octahedra, which undergo polarizing out-of-center distortions that give rise to remarkable properties in NCS materials.

Polarity in inorganic materials became the subject of intense study after the discovery of ferroelectricity in barium titanate $BaTiO_3$.[38–40] Detailed structural characterization revealed

that the polarity of $BaTiO_3$ originates from the distortion of the Ti^{4+} ion out of the center of its octahedral coordination environment, in apparent defiance of electrostatic forces that favor high symmetry in the cubic perovskite parent structure. The favorable combination of chemical stability and efficient nonlinear properties soon led to broad applications of $BaTiO_3$ and other polar oxides, including lead zirconate titanate Pb(Zr,Ti)O_3 (PZT),[41] potassium titanyl phosphate $KTiOPO_4$ (KTP),[42,43] and lithium niobate $LiNbO_3$ (LN).[44]

The spontaneous out-of-center distortions of ETM ions in $BaTiO_3$ and other materials based on d^0 early transition metal octahedra are described by the second-order, or pseudo-, Jahn-Teller (SOJT) effect.[45–51] According to the SOJT theory, symmetry-breaking distortions allow for vibronic coupling between otherwise nonbonding states, resulting in added covalency and energetic stabilization.[48,49] If an energetically favorable atomic displacement is present, such as that shown in Figure 1.3, a distortion will occur and the interaction between these orbitals will change from nonbonding to bonding. The overall result amounts to vibronic coupling between the atomic/group orbitals, which is mathematically described in brief below. For full details of the relevant derivations, we refer the reader to the numerous relevant publications by Bersuker and coworkers, of which several are cited here.[49–51]

Let K be the curvature of the adiabatic potential energy surface (APES) for some polyatomic system with energy E under a symmetrized atomic displacement Q such that $K = \frac{\partial^2 E}{\partial Q^2}$. Substituting $E = \langle \Psi | H | \Psi^* \rangle$, we can express K as follows:

$$K = \langle\ \Psi_0\ |\ (\frac{\partial^2 H}{\partial Q^2})\ |\ \Psi_0 \rangle - 2 \sum_n \frac{|\langle\ \Psi_0\ |\ (\frac{\partial H}{\partial Q})\ |\ \Psi_n\ \rangle|^2}{E_n - E_0}$$

We now define K_0 as the first term in the above expression and K_v as the second term such that $K = K_0 + K_v$. Physically, K_0 represents the restorative electrostatic force, which

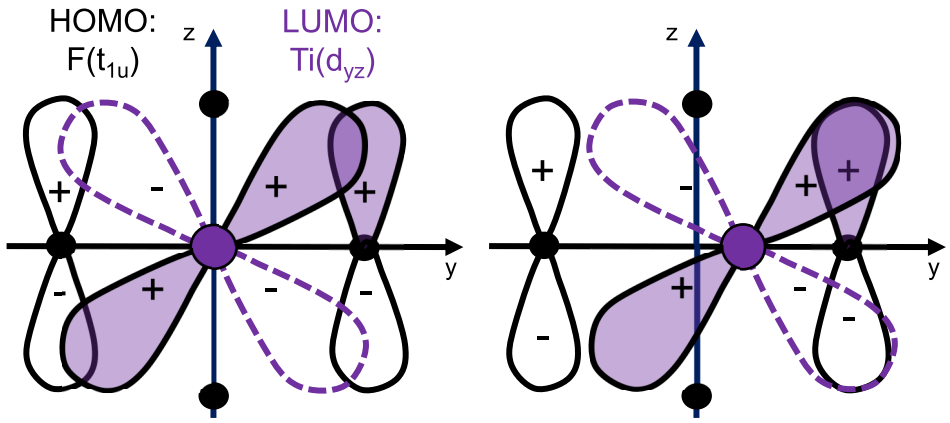

Figure 1.3. Depiction of added covalency through vibronic coupling between otherwise non-bonding metal d and ligand p orbitals, as described by the second-order Jahn-Teller effect. (left) In the high-symmetry configuration (octahedral in this case), the HOMO and LUMO orbitals are strictly non-bonding owing to their mismatched symmetry. (right) The symmetry-breaking out-of-center distortion allows for bonding between the HOMO and LUMO orbitals, and represents the added covalency offered by vibronic coupling of these states. Adapted from (Bersuker, 2021).

has been shown to always be positive for high-symmetry polyatomic systems. This result implies that the vibronic coupling term K_v is the only possible source of instability. Otherwise stated, the K_v term must be negative and larger in magnitude than K_0 if $K < 0$.

In the specific case of an octahedrally-coordinated d^0 ETM ion, TiO_6 in this instance, the form of the APES is determined by the following expression:

$$\Delta \gtrless \frac{8F^2}{K_0}$$

where 2Δ is the difference in energy between the oxygen $2p_z$ (HOMO) orbitals, which contribute to a set of group orbitals with t_{1u} symmetry, and Ti $3d_{yz}$ (LUMO) orbitals, which have t_{2g} symmetry, and F is the vibronic coupling constant for the oxygen $2p_z$ and Ti $3d_{yz}$

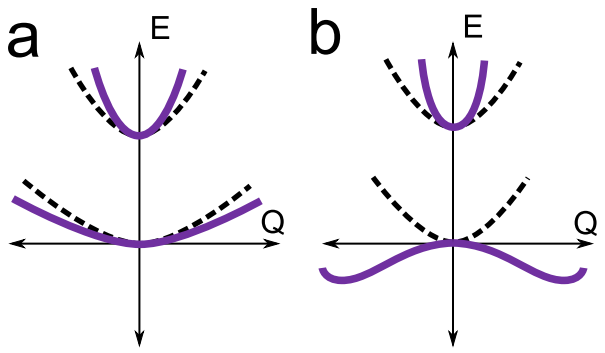

Figure 1.4. Schematic representation of the influence of the SOJT effect on the potential energy of a system with (a) weak SOJT effect and (b) strong SOJT effect. The dashed lines represent the system without vibronic coupling and the purple solid lines represent the system with vibronic coupling. Adapted from (Bersuker, 2021).

orbitals and has the form:

$$F = \langle\ 2p_z(O)\ |\ (\frac{\partial H}{\partial Q_y})\ |\ 3d_{yz}\ \rangle$$

where Q_y refers to a displacement along the y direction, as shown in Figure 1.3.

In the limit of weak vibronic coupling for some distortion Q, the following inequality holds: $\Delta > \frac{8F^2}{K_0}$. In this case, a single minimum is present at the center of the octahedron and no out-of-center displacement occurs. This scenario is depicted schematically in Figure 1.4a.

If the inequality holds in the opposite direction, $\Delta < \frac{8F^2}{K_0}$, strong vibronic coupling occurs and the APES adopts the form described by Bersuker as follows:

> [T]he surface has a maximum (meaning instability) when the Ti ion is in the center of the octahedron, eight equivalent minima placed along the four trigonal axes, in which the Ti ion is displaced toward three oxygen ions (away from the other three); higher-in-energy 12 equivalent saddle points along the six C_{2v} axes, at which the Ti ion is displaced toward two oxygen ions (at the

> top of the lowest barrier between two near-neighbor minima); and next six higher-in-energy equivalent saddle points, at which the Ti ion is displaced to one of the oxygen ions along the fourfold axes.[51]

In this limit, the ETM ion moves out of the center of the octahedron and the ground state configuration is altered as shown in Figure 1.4b. A notable consequence of this theory, which is born out experimentally, is that the Ti ion in $BaTiO_3$ is locally distorted even in the cubic paraelectric phase.[52]

ETM fluorides and oxide-fluorides offer a molecular platform from which to control the structural environment of out-of-center distorted d^0 ETM octahedra. The out-of-center distortions of d^0 early transition metals can be exploited to form molecular homoleptic anions with the formula MF_6^- (M = Nb, Ta) or MF_6^{2-} (M = Ti, Zr, Hf) and ordered heteroleptic anions with the general formula $MO_xF_{6-x}^{2-}$ (M = V, Nb, Ta, Mo, W). Homoleptic MF_6^- and MF_6^{2-} show variable out-of-center distortions due to the SOJT effect similar to those in $BaTiO_3$, with the distinction that in this molecular case the observed distortion is facilitated by secondary contacts with the extended structure and therefore strongly dependent on the structural environment, whereas the ordering of distortions in $BaTiO_3$ varies strictly as a function of temperature.[53,54]

Symmetry breaking in heteroleptic ETM oxide-fluorides occurs as a consequence of the more favorable orbital energy matching between oxygen p orbitals and ETM d orbitals compared to that of fluorine p orbitals and ETM d orbitals (smaller Δ, larger F). The more favorable orbital energy matching allows for bonding interactions between these states in the lower symmetry configuration, which would be nonbonding in the high-symmetry O_h configuration, resulting in a primary electronic distortion of the ETM ion toward the oxygen ligand to form shorter M-O bonds and longer M-F bonds. When oxygen and fluorine

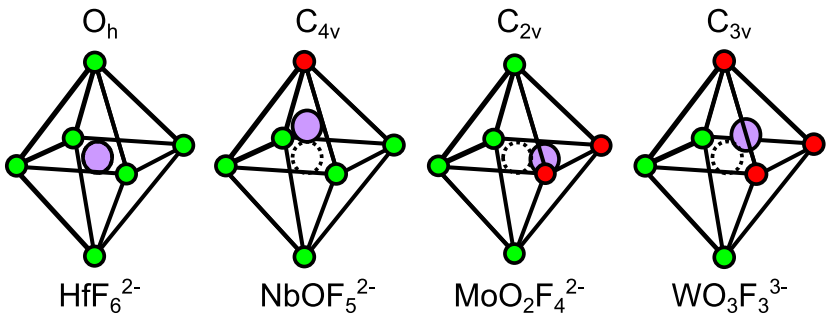

Figure 1.5. Schematic diagram of symmetry-breaking out-of-center distortions in early transition metal oxide-fluorides.

are ordered around the ETM ion, the local symmetry is reduced from O_h to C_{2v}, C_{3v}, or C_{4v} depending on the number of oxide ligands present. The reduced symmetry allows for increased covalency as described by the SOJT effect.

Polar structures are associated with ferroelectricity and superior NLO performance, making polarity an important design target for NCS materials.[37] The realization of polar crystal structures can be challenging, however, as polar molecules tend to adopt centrosymmetric arrangement owing to the favorable dipole-dipole interactions between positive and negative regions of polar molecules.[61] Since the realization of molecular ETM oxide-fluorides,[55–63] recent investigations have focused on controlling the alignment of ETM oxide-fluorides to achieve noncentrosymmetric and polar structures.[23,57,64–67] The ordered nature of ETM oxide-fluorides leads to specific struture-directing properties that are dependent on contacts between the most nucleophilic ligands and the surrounding environment following the principle of valence matching between the most nucleophilic ligands and the most electrophilic environment within the structure.[57,59]

1.3. Hydrothermal Pouch Method for Crystal Growth

Hydrothermal conditions are characterized by temperatures above the boiling point of water (>100°C) and pressures above atmospheric levels (>1 bar). Although these conditions were first employed to mimic the geothermal conditions for mineral formation as early as 1845, the hydrothermal method was widely adopted for the growth of quartz crystals after a shortage of natural crystals arose during World War II.[68] Hydrothermal crystal growth does not require a seed crystal, which allows for the use of hydrothermal techniques in the exploratory synthesis of crystalline materials.

The primary requirements for a hydrothermal reaction are an appropriate container and solvent. In the present thesis, all reactions were carried out in stainless steel Parr acid digestion vessels (Model 4748) with PTFE Teflon liners. The solvent of choice is water, with aqueous HF added as a mineralizer and fluorinating agent. The Teflon liner was chosen for its chemical resistance to HF and thermal stability under the relevant conditions (up to 150°C).

Whereas conventional hydrothermal reactions are carried out a single set of conditions at a time, the pouch method developed by Stucky and coworkers allows for reactions to be carried out in parallel across a range of chemical compositions.[69] The reaction scheme, shown in Figure 1.6, involves sealing solid reagents in Teflon pouches along with various solvents, including hydrofluoric acid. The advantages of this technique are the containment of hydrofluoric acid, which limits the risk of dangerous exposure, and the ability to perform many reactions in parallel within a single autoclave. Up to six pouches can be placed in a single autoclave, allowing for efficient examination of composition space.

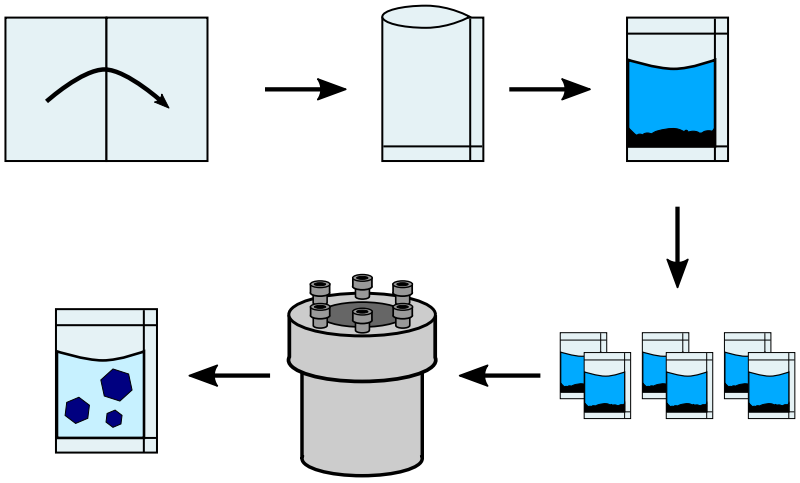

Figure 1.6. Schematic outline of the hydrothermal pouch method.

The hydrothermal pouch method offers the optimal set of conditions for the formation of ETM fluorides and oxide-fluorides while also allowing for efficient exploration of composition space by systematically varying reactant concentrations within each pouch. The hydrothermal pouch method has been employed to great effect in realizing novel NCS solids based on ETM fluorides and oxide-fluorides and elucidating the structure-directing properties of this family of anions, as described in section 1.2. Furthermore, the precise control over the reaction environment in each individual pouch means that the hydrothermal pouch method can be readily employed in tandem with data-driven approaches such as machine learning to efficiently examine and understand ensembles of reactions.

1.4. Scope and Organization

The following chapters detail our efforts to understand how racemic combinations of molecular chiral building units can be applied to facilitate the synthesis of noncentrosymmetric (NCS) materials. The previously reported NCS polar racemic compound Δ- and Λ-$[Cu(bpy)_2(H_2O)][HfF_6]\cdot 1.5H_2O$ (bpy = 2,2'-bipyridine) was used as a starting point to

elucidate how factors such as hydrogen bonding, π-π interactions, anion charge, cation symmetry, and identity of the anion contribute to inversion symmetry breaking.[22]

Chapter 2 describes how machine learning methods were combined with high-throughput hydrothermal synthesis and X-ray absorption spectroscopy to synthesize four new compounds, including the M = Zr, Ti members of the Δ- and Λ-$[Cu(bpy)_2(H_2O)][HfF_6]\cdot 1.5H_2O$ structure family, and rationalize the observed phase competition between the NCS compounds and CS structures in each system. Chapter 3 presents the results of substituting 1,10-phenanthroline for 2,2'-bipyridine as a means to probe the role of π-π stacking interactions in breaking inversion symmetry in a series of racemic compounds. In Chapter 4, we discuss the importance of charge and electronic structure in studying the synthesis and structures of compounds based on $Cu(bpy)_2(H_2O)^{2+}$ cations and TaF_6^-, SiF_6^{2-}, and SnF_6^{2-} anions. Chapter 5 includes the synthesis and structures of three compounds based on novel inorganic Λ-shaped molecules. A series of compounds designed as a platform from which to systematically study the local structure and dynamics of early transition metal fluorides and oxide-fluorides is presented in Chapter 6. The concluding Chapter 7 proposes future directions for investigations to understand general aspects of symmetry breaking in racemic compounds.

CHAPTER 2

Machine-learning-assisted Synthesis of Polar Racemates

This chapter was adapted with permission from:

Nisbet, M. L.; Pendleton, I. M.; Nolis, G. M.; Griffith, K. J.; Schrier, J.; Cabana, J.; Norquist, A. J.; Poeppelmeier, K. R. Machine-Learning-Assisted Synthesis of Polar Racemates. *J. Am. Chem. Soc.* **2020**, 142 (16), 7555–7566. https://doi.org/10.1021/jacs.0c01239.

2.1. Abstract

Racemates have recently received attention as nonlinear optical and piezoelectric materials. Here, a machine-learning-assisted composition space approach was applied to synthesize the missing M = Ti, Zr members of the Δ,Λ-[Cu(bpy)$_2$(H$_2$O)][MF$_6$]·1.5H$_2$O (M = Ti, Zr, Hf; bpy = 2,2'-bipyridine) family (space group: $Pna2_1$). In each (CuO, MO$_2$)/bpy/HF(aq) (M = Ti, Zr, Hf) system, the polar noncentrosymmetric racemate (M-NCS) forms in competition with a centrosymmetric one-dimensional chain compound (M-CS) based on alternating Cu(bpy)(H$_2$O)$_2$$^{2+}$ and MF$_6$$^{2-}$ basic building units (space groups: Ti-CS ($Pnma$), Zr-CS ($P\bar{1}$), Hf-CS ($P2/n$)). Machine learning models were trained on reaction parameters to gain unbiased insight into the underlying statistical trends in each composition space. A human-interpretable decision tree shows that phase selection is driven primarily by the bpy:Cu molar ratio for reactions containing Zr or Hf, and predicts that formation of the Ti-NCS compound requires that the amount of HF present be decreased to raise the pH, which we verified experimentally. Predictive leave-one-metal-out (LOO) models further confirm that

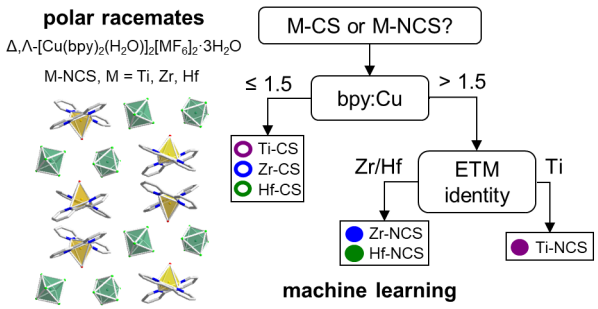

Figure 2.1. Two achiral noncentrosymmetric racemates were discovered by adopting a machine-learning-assisted composition space investigation.

behavior in the Ti system is distinct from that of the Zr and Hf systems. The chemical origin of this distinction was probed via fluorine K-edge X-ray absorption spectroscopy. Pre-edge features in the F1s X-ray absorption spectra reveal the strong ligand-to-metal π bonding between Ti($3d$ – t_{2g}) and F($2p$) states that distinguishes the TiF_6^{2-} anion from the ZrF_6^{2-} and HfF_6^{2-} anions.

2.2. Introduction

Noncentrosymmetric (NCS) materials are of wide commercial and academic interest owing to exciting properties, including ferroelectricity, piezoelectricity, and nonlinear optical activity, that are only allowed in materials lacking inversion symmetry.[1,2] Synthesis of NCS materials involves assembling functional basic building units (BBUs) and controlling their packing into an NCS crystal structure. In prominent NCS materials, such as $KTiOPO_4$,[42,70] $BaTiO_3$,[71] and $LiNbO_3$,[72] inversion symmetry breaking originates from the cooperative alignment of second-order Jahn–Teller (SOJT) distortions in d^0 early transition metal (ETM) octahedra.[45–47,49,73,74] Developing new NCS materials derived from d^0 ETM octahedra is a challenge, however, as polar ETM octahedra tend to anti-align and adopt centrosymmetric arrangements. Although chiral templating agents have often been introduced to guarantee

inversion symmetry breaking, further work is required to optimize and control interactions between polar and chiral BBUs to realize NCS materials with efficient properties.[3,18–21,75–77]

Recent reports indicate that racemic compounds, which contain both left- and right-handed enantiomers of a chiral BBU, can possess nonlinear optical and piezoelectric properties comparable to those of commercial NCS materials.[30,31] Racemates have long been observed to crystallize in NCS structures and are by no means rare, yet synthetic examinations of inversion symmetry breaking in racemic compounds have been limited.[24,26,27,78–82] Here, we present the targeted synthesis of a series of polar racemates based on d^0 ETM octahedra and racemic combinations of chiral copper-bipyridine (bpy) coordination complexes.

We applied a composition space approach to target the M = Ti, Zr members of the Δ- and Λ-[Cu(2,2'-bpy)$_2$(H_2O)][MF_6]·1.5H_2O (M = Ti, Zr, Hf;[22,83,84] space group $Pna2_1$) family. Composition space diagrams are useful tools for planning reactions and understanding reaction outcomes in terms of chemical trends by plotting reaction outcomes as a function of two or more variables, commonly the initial reactant mole fractions.[85,86] By examining the composition space of three (CuO, MO_2)/bpy/HF(aq) (M = Ti, Zr, Hf) systems, we were able to locate the crystallization field, or region of selective crystallization, of each racemic compound and structurally characterize compounds that form under similar conditions.

In tandem with our experimental approach, supervised machine learning (ML) models were trained on reaction parameters to gain unbiased insight into each system. Supervised ML models are functions mapping between a set of features (i.e., model inputs), such as descriptions of a chemical experiment, to a known output (e.g., the reaction outcome). The data used to train the model must be representative of the problem as a whole, requiring sampling of the relevant dimensions of chemical space. This includes sampling the chemical properties, reagent concentrations, and reaction conditions in order to capture reactivity

variations.[87,88] In practice, the datasets generated for use in ML need to be prepared and normalized such that they can be easily read into statistical analysis software packages. Models such as decision tree classifiers provide an unbiased prediction based upon underlying statistical patterns in the datasets using a human-interpretable function that can confirm or improve scientific insight.[89]

Following this approach, we found that polar Δ- and Λ-$[Cu(bpy)_2(H_2O)][MF_6]\cdot 1.5H_2O$ compounds (M = Ti, Zr, Hf), denoted as M-NCS, form in competition with a series of one-dimensional chain compounds with the formula $[Cu(bpy)(H_2O)_2(MF_6)]_n$ (M = Ti ($Pnma$), Zr ($P\bar{1}$), Hf ($P2/n$)), denoted as M-CS. Decision tree classification of reaction outcomes indicates that phase selection in each system is driven by the molar ratio of 2,2'-bipyridine (bpy) to Cu^{2+}, with M-CS phases forming when bpy:Cu is less than 1.5 and M-NCS forming when bpy:Cu is greater than 1.5 for reactions containing Zr and Hf. This parameter does not accurately capture the crystallization boundary between Ti-CS and Ti-NCS, however, as Ti-NCS only forms when bpy:Cu is greater than 1.5 and less than 0.0025 moles of HF are present. Predictive models trained using a leave-one-metal-out (LOO) strategy were able to predict the outcomes of reactions containing Zr or Hf with high performance but had low performance when predicting reaction outcomes in the (CuO, TiO_2)/bpy/HF(aq) system. Fluorine K-edge X-ray absorption spectroscopy was performed to experimentally discern the distinction between reactions carried out with Ti and those with Zr and Hf. Examination of pre-edge features in the F1s spectra reveals significant π bonding between Ti($3d$–t_{2g}) and F($2p$) states,[90,91] which also manifests in the diffraction data as short Ti–F bond distances and in the NMR data as a high frequency ^{19}F shift relative to Zr–F and Hf–F. This strong π bonding in TiF_6^{2-} is emblematic of a suitably small energy gap that facilitates SOJT activity, giving the TiF_6^{2-} anion distinct behavior compared to ZrF_6^{2-} and HfF_6^{2-}.

2.3. Methods

Caution. Hydrofluoric acid (HF) is toxic and corrosive! HF must be handled with extreme caution and the appropriate protective gear.

2.3.1. Materials

TiO_2 (Aldrich, 99.9+%) , ZrO_2 (Alfa Aesar, 99.978%), HfO_2 (Aldrich, 98%), CuO (Sigma-Aldrich, $\geq$ 99.0%), 2,2'-bipyridine (bpy) (Sigma-Aldrich, $\geq$ 99%), and HF(aq) (Sigma-Aldrich, 48% wt. in H_2O, $\geq$ 99.99% trace metals basis) were used as received. Reagent amounts of deionized water were used.

2.3.2. Hydrothermal Synthesis

Reactions were carried out following the hydrothermal pouch method.[69] The composition spaces of the (CuO, MO_2)/bpy/HF(aq) (M = Ti, Zr, Hf) systems were explored by varying the amounts of bpy and HF(aq) used in each reaction, while the amounts of CuO and MO_2 (M = Ti, Zr, Hf) were held constant. Deionized water was added to each pouch to achieve a final solution volume of 1.1 mL. Full details of the reactions can be found in a spreadsheet included as Supporting Information. After heat sealing, six pouches were placed into a 125 mL Teflon-lined Parr autoclave with 40 mL distilled water as backfill. This larger pressure vessel was heated at a rate of 5 °C/min to 150 °C and held at 150 °C for 24 h, then allowed to cool at a rate of 6 °C/h. Solid products were recovered via vacuum filtration.

2.3.3. Powder X-ray Diffraction

Powder X-ray diffraction was used to assign reaction outcomes and assess phase purity. Measurements were carried out using Cu Kα1 (λ = 1.5418 Å) radiation on STOE STADI-P and Rigaku IV Ultima diffractometers.

2.3.4. Single-Crystal X-ray Diffraction

Single-crystal X-ray diffraction was used to determine the structure of crystalline products. Diffraction patterns were recorded on Bruker-APEX II CCD diffractometers at 100 K with Mo Kα (λ = 0.71073 Å) radiation. Structures were solved with SHELXS and SHELXT and refined with SHELXL.[92] The diffraction data was integrated using SAINT.[93] Multi-scan absorption corrections were applied with SADABS.[94] No higher symmetry was found using symmetry checks in PLATON.[95] Hydrogen atom positions were located from difference maps and refined freely for the three M-CS structures. Hydrogen atoms bound to carbon atoms in 2,2'-bipyridine were attached in Olex2 using a riding model.[96] Hydrogen atoms of free water molecules and water molecules bound to $Cu(bpy)_2(H_2O)^{2+}$ units in the three M-NCS compounds could not be located from the difference maps and were omitted.

2.3.5. Machine Learning

The dataset used here consists of 51 experiments transcribed from laboratory notebook records, using the ESCALATE "entity, materials, actions, observations" ontology.[97] In addition to this raw experimental data, additional calculated stoichiometric properties and computed electronic structure properties were added. Stoichiometric features, such as molar amounts and molar ratios, were calculated directly from the experimental observations.

Electronic structure calculations were performed on the TiF_6^{2-}, ZrF_6^{2-}, and HfF_6^{2-} anionic building units to provide data on geometry, energetics, and charges using Gaussian 09, Revision D.01.[98] The B3LYP/LANL2DZ model chemistry was used as it provides good estimations (± 10 pm) for bond lengths of transition metal oxides and halides.[99] Atomic charges were assessed for the optimized geometries using Mulliken, Hirshfeld, CM5,[100] Natural Bond Orbital (NBO), and electrostatic potential fitting (Merz–Singh–Kollman using UFF radii, MKUFF) methods. The optimized geometries and output files are in the Supplementary Information. The optimized geometries were used for bond valence sum calculations. Features that are constant in all experiments, such as HF(aq) concentration, or those that are potentially misleading, such as the mass of the early transition metal were removed before performing ML calculations, reducing the number of features from 76 to 33. To improve model clarity, we performed feature selection using ANOVA F-value analysis using the f_classif function in SciKitLearn to isolate the three most important features: bipyridine-to-copper molar ratio, fluorine average NBO, and bpy normalized molar amount. The decision tree trained using only the top three features outperformed one trained on the full feature set on precision, accuracy, and recall. Other more sophisticated models are always provided the full feature set. Additional results and discussion can be found in the Supporting Information.

ML modeling was performed using SciKitLearn version-0.21.2.[101] The relevant hyperparameters (e.g., tree depth, leaf sample splits, and minimum samples per leaf for decision trees) were optimized through a permuted grid search varying and compared across two different hold-out regimes. In a standard test train split (STTS) hold-out regime, a 5-fold cross validation strategy is used; for each of the five cycles of the cross validation, 80% of the data are used for training the model (i.e., the model is given inputs AND outputs) and 20% is

used for testing the model predictions. In a leave-one-metal-out (LOO) hold-out regime, the dataset is divided into three groups based on the metal (Ti, Zr, Hf); two metals are used for training and the remaining metal is used for testing. For example, in one iteration of LOO model testing, Zr and Hf data is used to train the model and the performance is tested on how well the model predicted the outcomes of Ti. Model performance is reported using the average performance across all of the 'unseen' test groups (i.e., the left-out metal for LOO or the test samples for STTS).

Class imbalances, meaning divergent observation rates for different outcomes, can lead to challenges when relying upon model efficacy parameters such as precision and accuracy because they can be deceptive for datasets with imbalanced outcomes, such as the prevalence of M-CS or M-NCS phases in this dataset. Instead, Matthews correlation coefficients (MCC) are reported, as this metric is not affected by class imbalances. Models that only predict the majority class will have an MCC of zero; an MCC of '1' corresponds to perfect prediction of both M-CS and M-NCS. To establish the quality of the model we considered four performance baselines, corresponding to predicting the majority class for every task ('Majority (B)'), randomly guessing with the probability as the training data ('Probability (B)'), a support vector classification (SVC) model trained on randomly shuffled data ('Shuffled, SVC (B)'), and a model that uses the closest example in the training set as a proxy for memorization ('kNN, k=1'). A detailed description can be found in the Supporting Information.

2.3.6. X-ray Absorption Spectroscopy

X-ray absorption spectroscopy measurements were performed at Argonne National Laboratory Advanced Photon Source beamline 4-ID-C. The fluorine K-edge was scanned from 680 to 710 eV. Data was collected in both the total-electron-yield and total-fluorescence-yield

mode utilizing photocurrent for the electron yield and a silicon drift diode detector for the fluorescence yield. For all samples, the fluorescence yield produced more signal than the electron yield and was more reliable between runs. Three scans were performed on each sample and averaged to maximize the signal-to-noise ratio.

2.3.7. Solid-State Nuclear Magnetic Resonance Spectroscopy

^{1}H and ^{19}F solid-state nuclear magnetic resonance (NMR) spectra were recorded in a static magnetic field of 9.4 T with a Bruker Avance III spectrometer. The samples were packed into 1.6 mm diameter zirconia rotors and spectra were recorded at 40 kHz magic-angle spinning (MAS) in a Phoenix narrow-bore 1.6 mm HFX probe. T_1 (spin–lattice) relaxation was measured with a saturation recovery pulse. ^{1}H spectra were measured with a rotor-synchronized Hahn-echo ($\pi/2 - \tau - \pi - \tau-$acquire) pulse sequence using a 90°RF pulse of 1.22 µs and a recycle delay of 15 s. ^{19}F spectra were measured with the same pulse sequence with a 90°RF pulse of 1.3–1.75 µs and a recycle delay of 0.02 s. ^{19}F spectra were also collected with a recycle delay of 15 s and no difference was observed. For each ^{1}H measurement, 64 scans were co-added; for ^{19}F, 1024 scans were co-added. Variable temperature spectra were collected with a Bruker Cooling Unit (BCU) and heater. ^{1}H and ^{19}F spectra were externally referenced to adamantane at +1.8 ppm and the center of the doublet in $NaPF_6$ at –82.5 ppm, respectively. The actual sample temperature under MAS and external temperature control was calibrated with the ^{207}Pb shift of lead nitrate.[102,103] Frictional heating at 40 kHz MAS leads to an internal sample temperature of 44 °C. Temperatures under heating and cooling are given in the figures.

2.4. Results

2.4.1. Structure Descriptions

2.4.1.1. Noncentrosymmetric Polar Racemates. The Δ- and Λ -$[Cu(bpy)_2(H_2O)][MF_6]\cdot 1.5H_2O$ (M = Ti, Zr, Hf[22]) family of isostructural racemic compounds crystallizes in the polar space group $Pna2_1$. These compounds are denoted as M-NCS (M = Ti, Zr, Hf). The structure class (Figure 2.2) contains both Δ- and Λ-$Cu(bpy)_2(H_2O)^{2+}$ molecular cations and MF_6^{2-} (M = Ti, Zr, Hf) anions that are arranged via hydrogen bonding and $\pi - \pi$ stacking interactions. Two independent BBUs of each type are present in the asymmetric unit, with all atoms located on general positions. Homochiral pairs of $Cu(bpy)_2(H_2O)^{2+}$ cations pack in an alternating fashion with pairs of MF_6^{2-} BBUs along the *b* direction (Figure 2.2). These homochiral columns are related only by glide planes to columns containing $Cu(bpy)_2(H_2O)^{2+}$ cations with the opposite handedness. Hydrogen bonding contacts with each MF_6^{2-} unit give rise to differences in M–F bond lengths (between 1.799 Å and 1.889 Å for Ti–F bonds, 1.938 Å and 2.024 Å for Zr–F bonds, and 1.942 Å and 2.021 Å for Hf–F bonds). The differences in bond lengths result in small polar distortions, with the central M atom being displaced less than 0.006 Å from the center of each octahedron (Table 2.3). The polar moments of the MF_6^{2-} anions are partially aligned along c.

2.4.1.2. Centrosymmetric Chain Compounds. Three distinct centrosymmetric compounds were observed in this work, denoted as M-CS (M = Ti, Zr, Hf). In contrast to the three M-NCS compounds described above, $[Cu(bpy)(H_2O)_2(TiF_6)]_n$ (Ti-CS),[67] $[[Cu(bpy)(H_2O)_2]_2[Zr_2F_{12}]]_n$ (Zr-CS), and $Cu(bpy)(H_2O)_2(HfF_6)_n$ (Hf-CS) are not isostructural, although the M-CS compounds do share two structural motifs: (1) each Cu center is

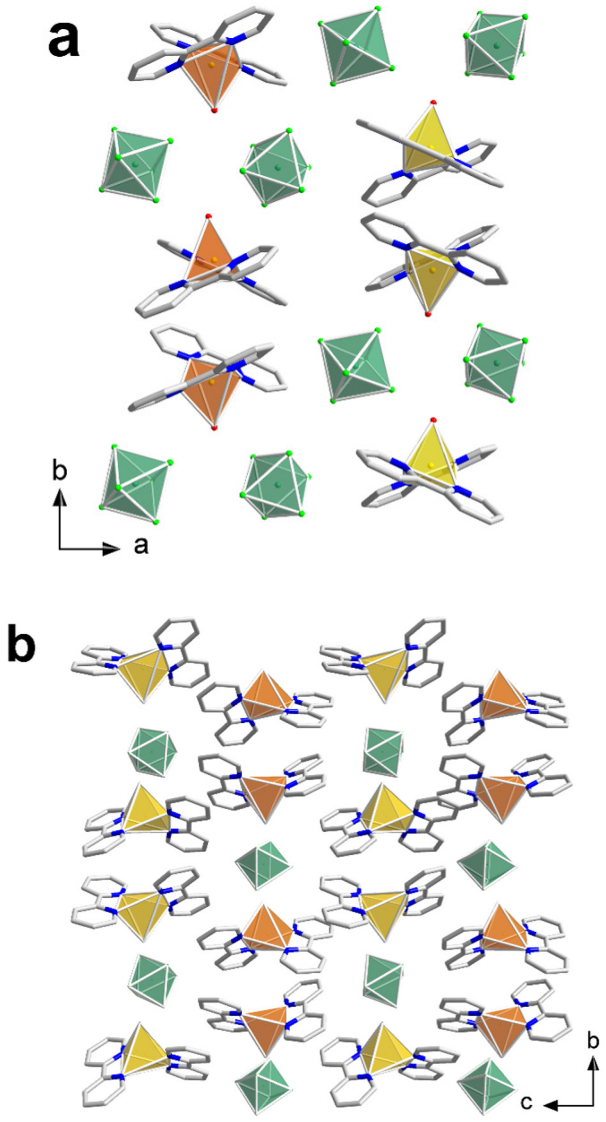

Figure 2.2. (a) The crystal structure of Δ,Λ-[Cu(bpy)$_2$(H$_2$O)][MF$_6$]·1.5H$_2$O (M-NCS, M = Ti, Zr, Hf) viewed along the c axis. The polar structure is composed of chiral Δ- and Λ-Cu(bpy)$_2$(H$_2$O)$^{2+}$ (Δ – orange, Λ – yellow) cations and weakly polar MF$_6{}^{2-}$ (green) anions. Free water molecules and all hydrogen atoms have been omitted for clarity. (b) View of the M-NCS structure viewed along the a axis. Free water molecules and all hydrogen atoms have been omitted for clarity.

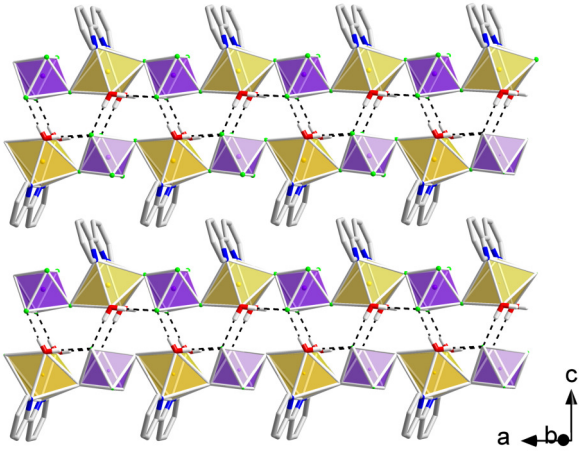

Figure 2.3. The crystal structure of $[Cu(bpy)(H_2O)_2(TiF_6)]_n$ (Ti-CS) features polar one-dimensional chains. Orange and purple polyhedra represent $Cu(bpy)(H_2O)_2{}^{2+}$ and $TiF_6{}^{2-}$ building units, respectively.

bound to a single bpy ligand and (2) each of the three M-CS phases contains one-dimensional chains of alternating $Cu(bpy)(H_2O)_2{}^{2+}$ and ETM-fluoride BBUs.

The structure of $[Cu(bpy)(H_2O)_2(TiF_6)]_n$ (Ti-CS) (Figure 2.3), originally reported in 2013, contains polar zigzag chains composed of alternating $Cu(bpy)(H_2O)_2{}^{2+}$ and $TiF_6{}^{2-}$ units.[67] Ti-CS crystallizes in the space group *Pnma* and is a member of an isostructural series of 1D chain compounds with the general formula $A(bpy)(H_2O)_2A'O_xF_{6-x}$ (A/A' = Cu/Ti, Cu/V, Cu/Nb, Cu/Mo, Zn/Mo, Zn/W).[67] Differences in Ti–F bond distances in the $TiF_6{}^{2-}$ anion reveal a C_2-type second-order Jahn–Teller (SOJT) distortion of the Ti atom toward the edge of the coordination octahedron. The central Ti atom of the $TiF_6{}^{2-}$ unit is displaced 0.011 Å out of the center of the coordination octahedron. The displacement occurs perpendicular to the chain direction, resulting in two short Ti–F1 bonds with distances of 1.7945(7) Å and two long Ti–F2 bonds with distances of 1.9414(7) Å. The Ti–F3 bonds along the chain have distances of 1.8749(9) Å and 1.8600(10) Å. The distortion is facilitated by inter- and intrachain hydrogen bonding interactions with F2 and water molecules in

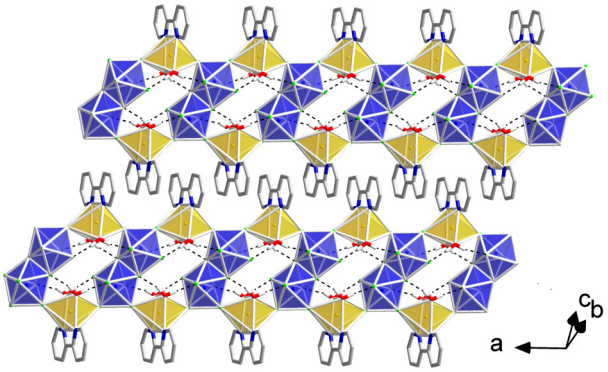

Figure 2.4. Crystal structure of Zr-CS (formula: $[[Cu(bpy)(H_2O)_2]_2[Zr_2F_{12}]]_n$). Zr-CS features 1D chains composed of $Cu(bpy)(H_2O)_2^{2+}$ (orange) and $Zr_2F_{12}^{4-}$ (blue) units.

$Cu(bpy)(H_2O)_2^{2+}$ units, with O1–F2 distances of 2.639 Å and 2.700 Å, respectively. Adjacent chains are arranged in the ac plane via hydrogen bonding interactions without stacking of bpy ligands.

Zr-CS crystallizes in the space group $P\bar{1}$ and has the formula $[[Cu(bpy)(H_2O)_2]_2[Zr_2F_{12}]]_n$. The structure of Zr-CS (Figure 2.4) features bridged "ladder" chains based on alternating $Cu(bpy)(H_2O)_2^{2+}$ and $Zr_2F_{12}^{4-}$ BBUs. The anionic $Zr_2F_{12}^{4-}$ cluster is similar to the $V_2O_2F_8^{2-}$ cluster found in $[Cu(bpy)(H_2O)]_2[V_2O_2F_8]$, which contains bridged chains wherein each cluster is involved in six bridging V–F–Cu linkages.[104] The $Zr_2F_{12}^{4-}$ clusters in Zr-CS bridge between $Cu(bpy)(H_2O)_2^{2+}$ units to form chains through four Zr–F–Cu linkages. Unlike the $V_2O_2F_8^{2-}$ cluster, which features edge-sharing VOF_5^{2-} octahedra, the $Zr_2F_{12}^{4-}$ cluster contains edge-sharing pentagonal bipyramidal ZrF_7^{3-} units. The Zr–F bond distances range from 2.0021(7) to 2.2050(7) Å. The central Zr atom is displaced 0.016 Å from the center of the pentagonal bipyramid as a result of cation-cation repulsion between neighboring Zr atoms in the edge-sharing $Zr_2F_{12}^{4-}$ cluster. Hydrogen bonding interactions are present along the chain direction linking the $Zr_2F_{12}^{4-}$ clusters and the coordinated water

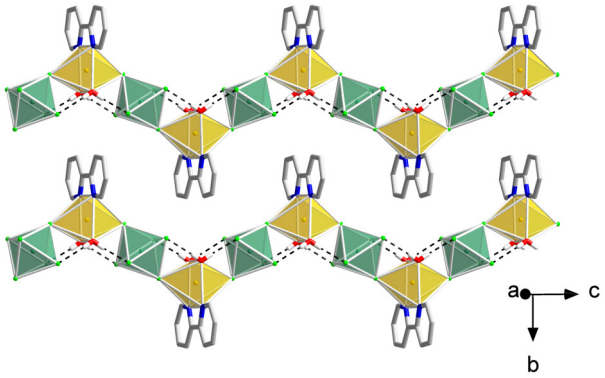

Figure 2.5. Crystal structure of $[Cu(bpy)(H_2O)_2(HfF_6)]_n$ (Hf-CS). Hf-CS contains nonpolar zig-zag chains based on $Cu(bpy)(H_2O)_2^{2+}$ (orange) and HfF_6^{2-} (green) basic building units.

molecules in $Cu(bpy)(H_2O)_2^{2+}$, with O–F distances of 2.593 and 2.639 Å. Adjacent chains are interlocked to form sheets via face-on $\pi - \pi$ stacking contacts.

The structure of $[Cu(bpy)(H_2O)_2(HfF_6)]_n$ (Hf-CS) (Figure 2.5) features nonpolar zigzag chains composed of alternating $Cu(bpy)(H_2O)_2^{2+}$ and HfF_6^{2-} units. The octahedral HfF_6^{2-} anion is undistorted with Hf–F bond distances between 1.9992(11) and 2.0052(10) Å and the Hf atom occupying an inversion center. Each equatorial fluorine participates in two hydrogen bonding interactions along the chain with O–F distances of 2.628 and 2.646 Å.

2.4.2. Solid-State NMR

Solid-state ^{19}F MAS NMR measurements were performed to analyze the local environment of the MF_6^{2-} anions in each structure. ^{19}F MAS NMR spectra of the isostructural paramagnetic M-NCS (M = Ti, Zr, Hf) compounds are shown in Figure 2.6. All three compounds show two resonances separated by about 10 ppm that integrate to 1:1 with a less than 0.5% error (Figure 2.6a). According to the crystal structure, there are 12 unique F atoms. Thus, the two ^{19}F signals are assigned to the two distinct TiF_6^{2-} octahedra, each signal

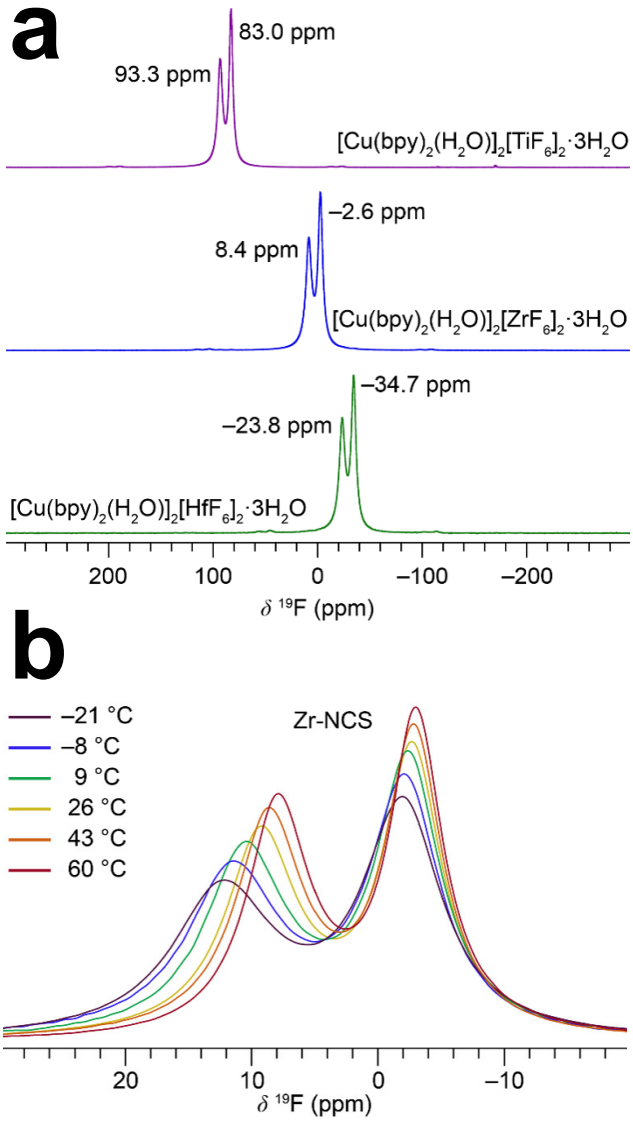

Figure 2.6. (a) ^{19}F solid-state MAS NMR spectra for the three M-NCS (M = Ti, Zr, Hf) compounds. (b) Variable temperature ^{19}F solid-state MAS NMR spectra for Zr-NCS.

representing six crystallographically-unique but motionally-averaged fluorine atoms. This hypothesis is supported by variable-temperature ^{19}F MAS NMR spectra measured from -21 to +60 °C (Figure 2.6b, Figure 2.12), which show that the linewidth decreases from low to high temperatures. Furthermore, the small spinning sidebands (Figure 2.6a) in the ^{19}F

spectra indicate that the chemical shift anisotropy (CSA) is almost completely suppressed by dynamic averaging even at ambient temperature. Spectral fitting suggests a CSA of no more than ±35 ppm, while typical early transition metal fluoride CSAs are much larger: e.g., 170 ppm in β-ZrF_4,[105] 300 ppm in NbF_5 and TaF_5,[106] and 900 ppm in TiF_4.[107] The ^{19}F resonances systematically shift to lower frequency from Ti to Zr to Hf. In each case, the two ^{19}F resonances are separated by 10–11 ppm, which is most likely attributable to the difference in average bond distance within the MF_6^{2-} octahedra (always about 0.005–0.01 Å) that arise from differences in hydrogen bonding between the two sites. These ^{19}F spectra indicate that the local environments and dynamic behavior of the MF_6^{2-} anions in the three M-NCS compounds are identical, consistent with the single crystal structures. The motional dynamics of the isolated octahedra will likely influence the properties of these materials, which may be of interest for future studies. The ^{1}H spectra of all three NCS compounds are identical, displaying broad resonances centered around 11 and 16 ppm (Figure 2.13), and do not vary with temperature (Figure 2.14).

The situation in the non-isostructural paramagnetic M-CS phases is considerably different. Evidently the paramagnetic effects are so strong in Ti-CS that neither ^{1}H (Figure 2.13) nor ^{19}F (Figure 2.15) signals were observed. In the ^{19}F NMR of Zr-CS, four resonances of equal integrated intensity were observed. The compound has six distinct fluorine sites in the asymmetric unit; however, two of these fluorine atoms are directly bound to copper as Zr–F–Cu bridges whereas three are terminal Zr–F and one is bridging Zr–F–Zr. The Zr–F–Cu fluorine atoms are likely not observed due to rapid paramagnetic relaxation while the terminal F are assigned to the three resonances at 37, 25, and 15 ppm and the signal at -63 ppm is assigned to Zr–F–Zr. These assignments are made on the basis of the bond

lengths; shorter M–F bonds (such as terminal fluorine) experience a larger paramagnetic contribution to shielding and thus appear at higher frequencies than longer M–F bonds (such as bridging fluorine).[105] N.B. the paramagnetic term described here is not directly related to Cu, rather it is the second-order paramagnetic contribution to the local magnetic field from the orbital motion of valence electrons as originally described by Ramsey, Saika, and Slichter.[108,109] Finally, in the Hf-CS compound, there are three distinct fluorine sites, again one is bridging Hf–F–Cu while two are terminal Hf–F. It appears that the two distinct terminal fluorine are overlapping with an isotropic shift of 2 ppm. The ^{19}F Hf-CS assignment is based on the nearly identical bond distances of Hf–F2 (1.9992(11) Å) and Hf–F3 (1.9994(11) Å), the similarity to the shifts of the terminal Zr–F, and the broader linewidth of the Hf-CS ^{19}F signal as compared to the individual terminal ^{19}F signals in Zr–F. Zr-CS and Hf-CS both showed three broad proton signals from 10 to 70 ppm.

Given the presence of d^9 Cu(II), paramagnetic shifts and paramagnetic relaxation enhancement are expected. The ^{1}H shifts are well outside the normal shift range though the ^{19}F signals that are observable are within the range of diamagnetic fluoride compounds. The spin–lattice relaxation of all ^{1}H and ^{19}F compounds was below 20 ms, which is consistent with the expected dipolar relaxation rate for d^9 Cu(II).[110]

2.4.3. Composition Space Analysis

Machine learning efforts can provide considerable insight into the domain under inspection. This process beings with an evaluation of the dataset, which was manifested in two ways in the work presented here. First, a series of visualizations were created to help evaluate the extent of the explorations. Second, working with the experimental data allowed for the

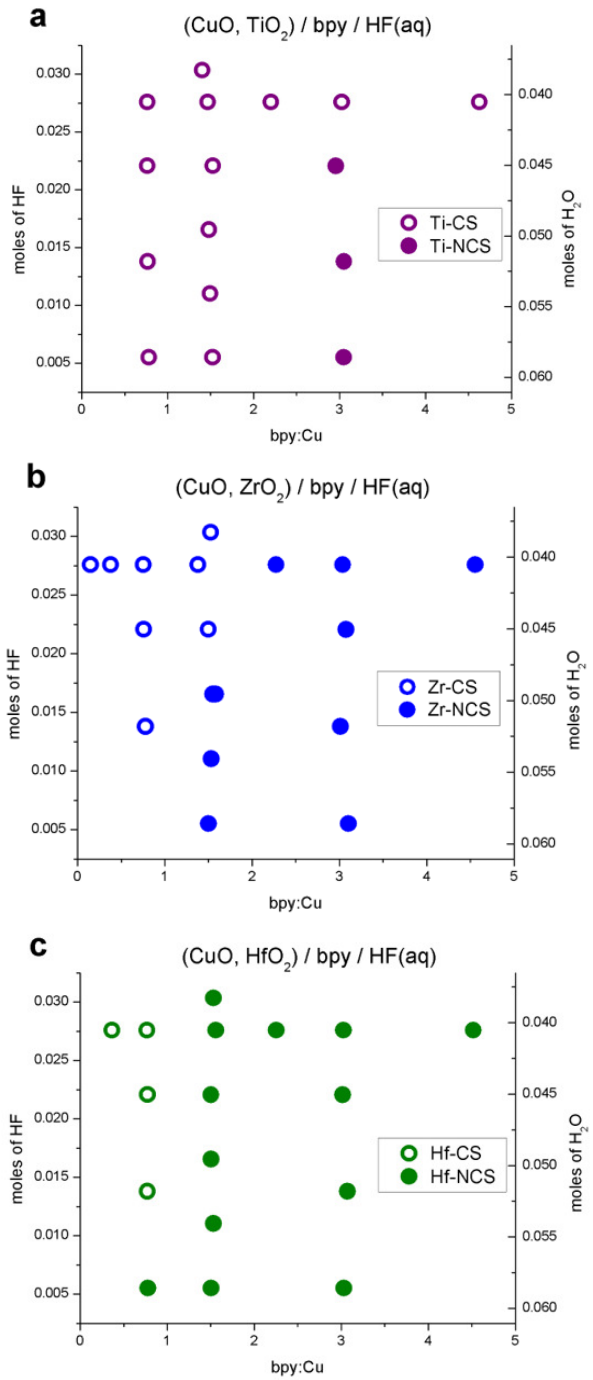

Figure 2.7. Composition space diagrams for the (CuO, MO_2)/bpy/HF(aq) (M = (a) Ti, (b) Zr, (c) Hf) systems.

identification of outliers and provided insight into data input errors, which has improved the future reusability and relevance of the dataset for use in larger machine learning projects.

The formation of $Cu(bpy)_2^{2+}$ species is favored either by increasing pH or raising the bpy:Cu molar ratio, as seen in the relevant distribution diagrams from previous studies of aqueous copper-bipyridine systems.[111] The initial experiments investigated the independent roles of the bpy:Cu ratio and pH in each (CuO, MO_2)/bpy/HF(aq) (M = Ti Zr, Hf) system, which lead to the synthesis of Ti-CS, Zr-NCS, Zr-CS, Hf-NCS, and Hf-CS. Visualizing this data revealed the need for additional experiments where both the bpy:Cu ratio and the amount of HF were varied. Ultimately the Ti-NCS compound was discovered in the region of composition space with simultaneously high bpy:Cu ratio and high pH (low amount of HF) as a direct result of the data visualizations that were performed, and enabled the subsequent machine learning work to probe the formation of this additional phase.

In the preliminary data visualizations, outlier experiments consisting of isolated reaction products surrounded by other phases were observed. A re-analysis of the powder X-ray diffraction phase identification revealed incorrect phase identity determinations, which would have negatively impacted the resulting machine learning models. The cleaned and curated dataset has also been provided along with the relevant characterization in a machine readable format on the materials data facility.[112–114]

Composition space diagrams (Figure 2.7) were constructed for each (CuO, MO_2)/bpy/HF(aq) (M = Ti, Zr, Hf) system. A total of 51 reactions were conducted across the three systems, with varying HF and bpy concentrations targeted for exploration. Identification of the dominant solid product for each individual reaction led to the observation of both a polar racemate (M-NCS) and a centrosymmetric one-dimensional chain compound (M-CS) (M =

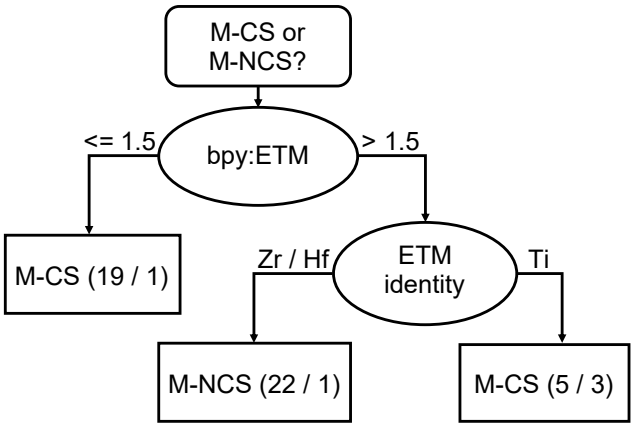

Figure 2.8. Decision tree classification of M-CS versus M-NCS. The three entries in terminal leaves indicate the symmetry of largest class in the leaf (either CS or NCS), along with the number of correct predictions and the number of incorrect predictions, respectively.

Ti, Zr, Hf) in each system. The crystallization fields for these six compounds vary in terms of both position and breadth.

A decision tree algorithm was employed to provide interpretable quantification of key experimental properties and the associated numerical cutoffs. The decision tree model shown in Figure 2.8 was fit on bipyridine-to-copper ratio, fluorine average NBO, and bpy normalized molar amount; these were the three features selected algorithmically through feature selection to avoid overfitting (see methods section). The model targeted classification of each experiment based on whether it produced M-NCS or M-CS.

The decision tree model (Figure 2.8) captures the primary division in the dataset; M-CS compounds are observed when the ratio of bipyridine to copper is less than or equal to 1.5, with 19 of the 20 reactions performed with a bpy:Cu ratio less than 1.5 being correctly classified as producing M-CS. Continuing to the right internal node, the identity of the transition metal distinguishes the reaction outcome when the bpy:Cu ratio is above 1.5. The identity of the metal was described via the metal-NBO feature, the numerical value of

which corresponds to the charge on the MF_6^{2-} metal center. All electronic structure features related to the MF_6^{2-} anions are linearly correlated (see Feature Covariance Matrix Figure 2.16), indicating that the predominant characteristic of the feature is not the numerical value but rather the correspondence to a given metal. The decision tree correctly classifies 22 out of 23 reactions involving Zr and Hf with bpy:Cu >1.5 as producing M-NCS. For Ti reactions, however, five out of the eight reactions classified in this leaf produced Ti-CS, meaning that the tree does not produce a leaf in which the majority phase is Ti-NCS. Therefore, the decision tree model is able to effectively classify reactions for Zr and Hf but does not fully capture the crystallization boundary between Ti-CS and Ti-NCS.

The limited efficacy of the decision tree for differentiating the boundary between Ti-CS and Ti-NCS motivated us to develop and compare against three other more sophisticated ML algorithms (i.e., support vector classifiers [SVCs], random forests, and k-nearest neighbors [kNN]), as well as different hold-out regimes including leave-one-metal-out in addition to the five-fold test-train split (STTS) (see Methods for details). The leave-one-out (LOO) models are denoted as "extrapolative" as they are constructed using data from two early transition metals as the training set and predicting crystallization outcomes for the third metal that was "left out" as the test set. Standard test train split models are denoted as 'interpolative' owing to the high degree of overlap between the data within each fold of the cross-validation. Interpolative STTS models are generally expected to perform better than comparable 'extrapolative' LOO models. Baseline models are denoted with a "(B)" and are explained in the methods section. MCC for each fold of the leave-one-metal out models are shown in Table 1 and Figure 2.9.

Evidence for a distinction between the Ti reactions with respect to the Zr and Hf reactions is found in the decision tree shown in Figure 2.8, as discussed above. This evidence is found

in the presence of a node that separates Ti from the Zr and Hf reactions. Support for this distinction can also be found in the LOO models. Models trained through LOO hold-out regimes generally perform slightly worse when predicting reaction outcomes when Ti is the target, better for Hf, and best for Zr as the target (Figure 2.9). For the LOO task, the decision tree has the highest MCC of 0.78 for Zr, 0.59 for Hf, and 0.48 for Ti. From these analyses we conclude that the interpretable decision tree model is competent at differentiating M-CS and M-NCS and is statistically competitive with other more sophisticated models for LOO training regimes.

In contrast with the LOO models, the interpolative STTS models are trained with data from all three early transition metals (Ti, Zr, Hf) and consequently are expected to perform better than LOO models across all metrics. A plot detailing the MCCs for the STTS models is shown in Table 2. The highest observed MCCs, 0.78 $\pm$ 0.15 for kNN k = 1 and 0.79 $\pm$ 0.17 for linear SVC, were similar to the performance of the interpretable decision tree, which yielded an MCC of 0.74 $\pm$ 0.29, but with a lower standard deviation. The similar predictive power of other ML methods compared with decision tree performance indicates that three features (bipyridine-to-copper molar ratio, fluorine average NBO, and moles of bipyridine) are sufficient to describe this dataset and there is no loss in predictive power by using an interpretable decision tree model. This confirms what is observed via human inspection, namely that phase selection is primarily driven by the bpy:Cu ratio but that this parameter does not fully describe the phase boundary between Ti-NCS and Ti-CS. Furthermore, all tested models outperform the benchmarks with the exception of the memorization benchmark, which indicates that the search space is sufficiently sampled to distinguish the crystallization boundary between the M-NCS and M-CS phases using solely the most similar previous reactions.

Table 2.1. Matthews correlation coefficient (MCC) for each leave-one-metal-out (LOO) model. "B" in the model name signifies a baseline comparison.

Model Name	Ti	Zr	Hf
Majority (B)	0.00	0.00	0.00
Probability (B)	-0.02	0.29	0.12
Shuffled, SVC (B)	0.25	-0.12	-0.03
kNN, k = 1 (B)	0.42	0.44	0.59
kNN, k = 5	0.42	0.61	0.59
Linear SVC	0.42	0.44	0.59
Decision Tree	0.48	0.78	0.59
Random Forest	0.37	0.68	0.31

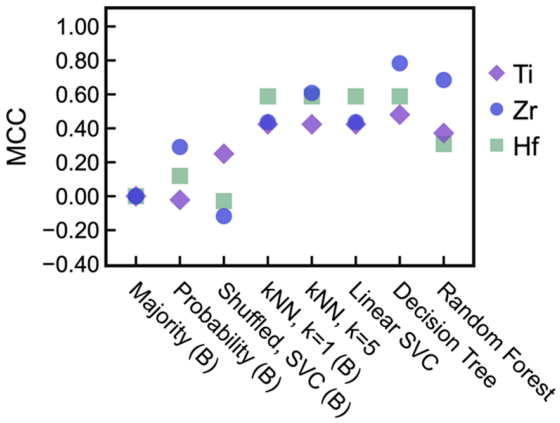

Figure 2.9. Visualization of the Matthews correlation coefficient (MCC) for extrapolative leave-one-metal-out (LOO) models. "B" in the model name signifies a baseline comparison.

Table 2.2. Matthews correlation coefficient (MCC) for each standard test train split (STTS) model. "B" in the model name signifies a baseline comparison.

Model Name	MCC
Majority (B)	0.00
Probability (B)	-0.05 ± 0.18
Shuffled, SVC (B)	-0.14 ± 0.25
kNN, k = 1 (B)	0.78 ± 0.15
kNN, k = 5	0.52 ± 0.16
Linear SVC	0.79 ± 0.17
Decision Tree	0.74 ± 0.29
Random Forest	0.31 ± 0.36

2.4.4. X-ray Absorption Spectroscopy

Fluorine K-edge X-ray absorption spectroscopy measurements were performed to examine covalency in each MF_6^{2-} anion (Figure 2.10).[91,115–118] Previous studies have shown that fluorine K-edge spectroscopy, which probes electronic transitions from the filled F($1s$) orbitals to empty orbitals with F(np) character, can be used to probe metal-ligand covalency.[116] Because the F($1s$) orbital is highly localized, excitations to empty metal d states can only be observed when the metal d orbitals are hybridized with F($2p$) orbitals.[117]

In these spectra, two regions can be distinguished. First are the features in the pre-edge region (<690 eV) corresponding to F($2p$) orbitals hybridizing with empty Ti($3d$), Zr($4d$), and Hf($5d$) states. And second, in the main edge region (>690 eV), these features correspond to F($3p$) orbitals hybridizing with empty Ti($4sp$), Zr($5sp$), and Hf($6sp$) states, and, at higher energies, multiple scattering events of the completely unbound electron. Since the transition metals are octahedrally coordinated, features in the pre-edge region provide direct evidence of crystal field splitting effects on the metal d orbitals.

F1s spectra for the Ti-based compounds, Ti-NCS and Ti-CS, are in good agreement with previous measurements of the F K-edge in K_2TiF_6.[119–121] The pre-edge peak at 685 eV (A) represents covalent mixing between Ti($3d$–t_{2g}) and F($2p$) states, while the pre-edge peak at 687 eV (B) represents covalent mixing between Ti($3d$–e_g) and F($2p$) states. The presence of pre-edge features A and B indicates significant σ and π character in the bonding of the TiF_6^{2-} anion.

Examining the spectra recorded for Zr- and Hf-based compounds, a dominant pre-edge feature B at 687 eV (B) is observed. For Zr-NCS, Hf-NCS, and Hf-CS, which contain octahedral ZrF_6^{2-} and HfF_6^{2-} anions, the strong pre-edge peak B is consistent with Zr($4d$

– e_g) and Hf($5d$ – e_g) hybridization with F($2p$) states. The presence of a weak pre-edge peak at 685 eV illustrates the limited hybridization between Zr($4d$ – t_{2g})/Hf($5d$ – t_{2g}) and F($2p$) states. There was too much noise in the spectrum of Hf-NCS to observe any pre-edge feature at 685 eV. Peak B is dominant in Zr-NCS, Hf-CS, and Hf-NCS because orbital overlap is higher for the primary σ crystal field splitting interactions in octahedral configurations, which occur along the bonding axis (e_g), compared to π bonding interactions (t_{2g}). The dominant pre-edge feature B in the spectrum for Zr-CS is consistent with the presence of σ interactions through the primary crystal field splitting in a 7-coordinate pentagonal bipyramidal environment via mixing of Zr($4d$ – a_1') and F($2p$) states.[122] The low intensity of the feature at 685 eV indicates the limited hybridization of the Zr($4d$ – e_2') and Zr($4d$ – e_1") orbitals with F($2p$) states. The observations clearly indicate that the π interactions are much weaker for the Hf and Zr compounds compared to Ti,[123] leading to t_{2g} states that have little F character.

The spectra remain consistent for both structures containing each anion, indicating that the electronic interactions are inherent to each MF_6^{2-} BBU. These spectra indicate qualitative differences in the electronic structure of the TiF_6^{2-} anion compared to the ZrF_6^{2-} and HfF_6^{2-} anions, with TiF_6^{2-} featuring strong σ and π bonding while ZrF_6^{2-} and HfF_6^{2-} have strong σ bonding and weak π bonding.

2.5. Discussion

Visualization of each composition space aided by machine learning modeling captures the unique character of the TiF_6^{2-} anion. The decision tree classification and predictive machine learning models capture statistical differences in the three composition spaces examined in

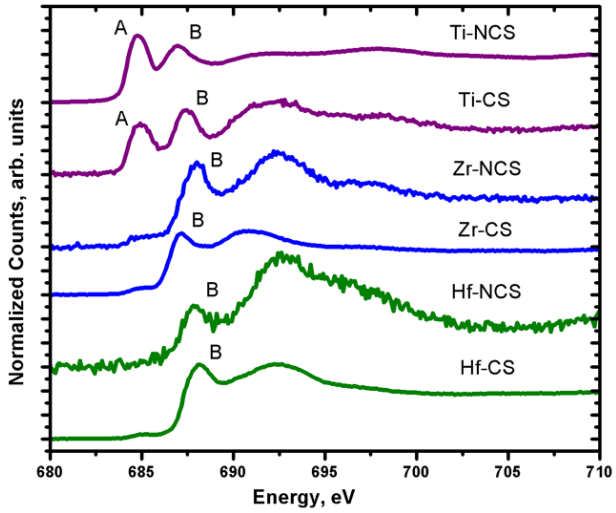

Figure 2.10. F1s absorption spectra for Ti-NCS, Ti-CS, Zr-NCS, Zr-CS, Hf-NCS, and Hf-CS. The pre-edge feature A represents M(nd – t_{2g}) – F(2p) covalency, while the pre-edge feature B represents M(nd – e_g) – F(2p) covalency.

this study that point to chemical differences between reactions containing Ti and those containing Zr or Hf.

XAS measurements provide experimental evidence that the MF_6^{2-} (M = Ti, Zr, Hf) anions are distinguished by the strength of ligand-to-metal π bonding. Pre-edge features in the fluorine K-edge XAS spectra demonstrate that the TiF_6^{2-} anion possesses strong π bonding interactions that are weak in the ZrF_6^{2-} or HfF_6^{2-} anions. The strong ligand-to-metal π bonding gives the TiF_6^{2-} anion second-order Jahn–Teller (SOJT) character, as the energy gap between filled F(2p) orbitals and empty Ti(3d – t_{2g}) orbitals is small enough to allow for mixing to occur between these states.[48,49] Conversely, weak π bonding in the ZrF_6^{2-} and HfF_6^{2-} anions reflects the fact that these anions lack SOJT activity because the energy gap between filled F(2p) and unoccupied Zr(4d – t_{2g})/Hf(5d – t_{2g}) states is too large.

The SOJT character of the TiF_6^{2-} anion allows for out-of-center distortions to occur in a suitable structure.[48,56] Therefore, interactions with the extended structure must be

considered to understand the presence or absence of distortions in the TiF_6^{2-} anion. Previous studies have shown that TiF_6^{2-} anions may experience distortions of the central Ti atom toward an edge (C_2-type), face (C_3-type), or vertex (C_4-type), or remain undistorted, depending on the nature of hydrogen bonding interactions and other contacts with the extended structure.[53] To understand the interplay of structural and electronic factors in the Ti-CS and Ti-NCS compounds, we will compare the structures of Ti-CS and Ti-NCS with Hf-CS and Hf-NCS. We limit the following discussion to Ti and Hf because the 7-coordinate environment of Zr-CS complicates direct comparison with the other M-CS structures. In the structure of Zr-CS, the edge-sharing nature of the $Zr_2F_{12}^{4-}$ anion gives rise to distortions from cation-cation repulsion that are not present for Ti-CS or Hf-CS.

The structure of Ti-CS features a C_2-type distortion in the TiF_6^{2-} anion, which is supported by the asymmetric distribution of hydrogen bonding contacts on one side of the octahedron (Figure 2.11a). These contacts mitigate the large residual charge on the two fluoride ligands away from which the central Ti atom is displaced, making the Ti-CS structure suitable for SOJT activity in the TiF_6^{2-} anion. Hf-CS and Ti-CS reflect the structural differences that arise from the SOJT activity of the TiF_6^{2-} anion. Hf-CS features the same connectivity as Ti-CS yet the environment of the HfF_6^{2-} anion is undistorted, as the Hf($5d$)–F($2p$) energy gap is too large to allow for SOJT activity (Figure 2.11b).

The structures of Ti-NCS and Hf-NCS, on the other hand, feature small distortions in the MF_6^{2-} anions that are comparable in magnitude for TiF_6^{2-} and HfF_6^{2-} (Figure 2.11b). In both cases, the central M atom is displaced less than 0.006 Å from the center of the octahedron (Table 2.3). As the distortions are comparable for SOJT-active TiF_6^{2-} and SOJT-inactive HfF_6^{2-}, the distortions in the M-NCS structures result from hydrogen bonding interactions rather than SOJT activity.[22] The small distortion in Ti-NCS indicates

that the arrangement of hydrogen bonding interactions in this structure does not support the SOJT activity of the TiF_6^{2-} anion.

Our machine-learning-assisted composition space investigation revealed that behavior in each (CuO, MO_2)/bpy/HF(aq) (M = Ti, Zr, Hf) system is strongly dependent on the choice of ETM. Analysis of each composition space shows that phase selection in the three (CuO, MO_2)/bpy/HF(aq) (M = Ti, Zr, Hf) systems is driven by the bpy:Cu ratio, with lower values of bpy:Cu favoring the formation of $Cu(bpy)(H_2O)_2^{2+}$ cations in M-CS compounds and higher values of bpy:Cu favoring the formation of Δ- and Λ-$Cu(bpy)_2(H_2O)^{2+}$ cations in M-NCS compounds. Phase selection for M = Zr and Hf can be achieved by modifying reaction stoichiometry to reflect the ratio of the desired phase, as Zr-NCS and Hf-NCS feature a bpy:Cu ratio of 2 while Zr-CS and Hf-CS have a bpy:Cu ratio of 1. The presence of the TiF_6^{2-} anion shifts the speciation equilibrium toward the formation of $Cu(bpy)(H_2O)_2^{2+}$ species and away from Δ- and Λ-$Cu(bpy)_2(H_2O)^{2+}$ complexes, as demonstrated by the formation of Ti-NCS only when bpy:Cu greater than 1.5 and the amount of HF is less than 0.0025 moles. The shift in speciation equilibrium indicates an increase in the stability of Ti-CS relative to Zr-CS and Hf-CS. Ti-CS is stabilized by two factors: (1) increased covalency via the out-of-center SOJT distortion and (2) hydrogen bonding interactions that compensate for the decrease in covalency in the two long Ti–F bonds. The stability of the Ti-CS structure shifts speciation to favor $Cu(bpy)(H_2O)_2^{2+}$ cations and form the one-dimensional polar chains that allow for the SOJT distortion to occur, rather than Δ- and Λ-$Cu(bpy)_2(H_2O)2+$ cations that form the Ti-NCS structure and do not allow for a SOJT distortion. These factors make Ti-CS more competitive with Ti-NCS during crystallization than the Zr-CS and Hf-CS counterparts.

Using ML on the experimental data provided many advantages. First, the data visualization efforts resulted in additional experiments, during which Ti-NCS was first synthesized.

Additionally, these data visualizations enabled the identification of outlier points, which were addressed using data cleaning techniques. Working with the experimental data also provided insight into data input errors which has improved reproducibility and replicability of the experiments reported. Second, modeling the experiments provided unbiased statistical support to human intuition in the form of visualizations, an interpretable decision tree, and predictive LOO models that emphasize distinct properties of Ti compared to Hf and Zr. The machine learning models presented here provide statistical significance to the qualitative data inferences made by human inspection and can quantify traditionally qualitative arguments. We emphasize that these models are not intended to be generalizable to M-CS and M-NCS prediction for a broader range of early transition metals. Instead, the models were used to demonstrate how interpretable ML can capture the salient phase boundary information in small experimental datasets. These results support the distinction between composition spaces outlined for Ti and those for Zr and Hf, a point which is further corroborated from data visualization and decision tree analysis.

2.6. Conclusion

A strategy combining high-throughput hydrothermal synthesis with machine learning was employed to synthesize two new polar compounds, Ti-NCS and Zr-NCS, based on racemic combinations of Δ- and Λ-Cu(bpy)$_2$(H$_2$O)$^{2+}$ cations, as well as two related centrosymmetric compounds, Zr-CS and Hf-CS. Machine-learning analysis of reaction outcomes shows that phase selection between M-NCS and M-CS phases in each (CuO, MO_2)/bpy/HF(aq) (M = Ti, Zr, Hf) composition space is primarily driven by the bpy:Cu molar ratio for reactions containing Zr and Hf, while phase selection between Ti-NCS and Ti-CS shows an additional dependence on the amount of HF present in the reaction. Fluorine K-edge XAS reveals

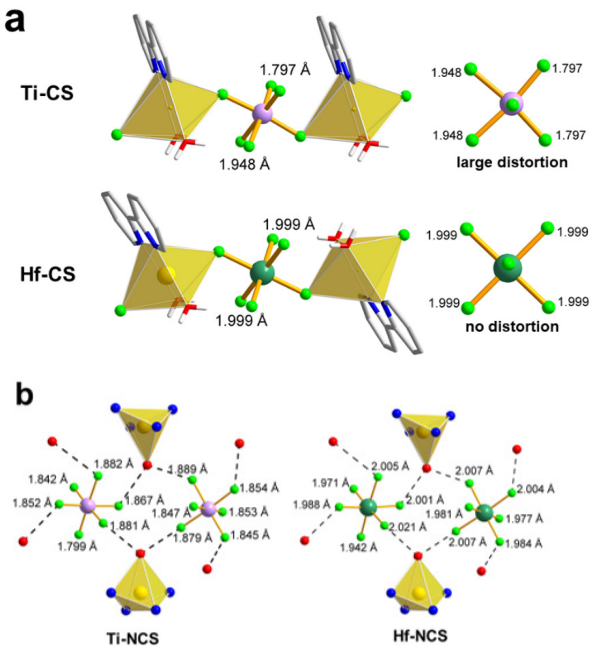

Figure 2.11. (a) Configurations of octahedral MF_6^{2-} units in Ti-CS and Hf-CS. The large structural distortion of TiF_6^{2-} in Ti-CS reflects the presence of SOJT effects in the TiF_6^{2-} anion, while the lack of a distortion in Hf-CS is consistent with a lack of SOJT effects in the HfF_6^{2-} anion. (b) Smaller octahedral distortions are present in both Ti-NCS and Hf-NCS as a result of hydrogen bonding interactions (shown as dashed lines). Bond lengths of M–F bonds are labeled. Bipyridine ligands and hydrogen atoms have been omitted for clarity.

that strong ligand-to-metal π bonding between Ti($3d$ – t_{2g}) and F(2p) states distinguishes TiF_6^{2-} from ZrF_6^{2-} and HfF_6^{2-}. Crystallographic data and ^{19}F NMR spectra are consistent with this distinction. Furthermore, the solid-state NMR data indicate rapid motion in the isolated MF_6^{2-} octahedra for all three compounds in the M-NCS series. The present study illustrates the value of combining synthetic methods with data visualization, which improves reproducibility and replicability of the experiments reported, and machine learning techniques that provide unbiased insight from ensembles of experiments. With these findings

Table 2.3. Out-of-Center Distortions in M-CS and M-NCS (M=Ti, Zr, Hf) Compounds. Out of center displacements ($d_{centroid}$) were calculated as the distance from the central metal atom to the centroid of the surrounding fluoride ligands.

Compound Label	Metal Label	Δ_d	$d_{centroid}$
Ti-NCS	Ti1	0.13623	0.00469
Ti-NCS	Ti2	0.07407	0.00245
Zr-NCS	Zr1	0.12434	0.00575
Zr-NCS	Zr2	0.03001	0.00224
Hf-NCS	Hf1	0.15058	0.00412
Hf-NCS	Hf2	0.04604	0.00224
Ti-CS	Ti1	0.31884	0.0114
Zr-CS	Zr1	*	0.0164
Hf-CS	Hf1	0	0

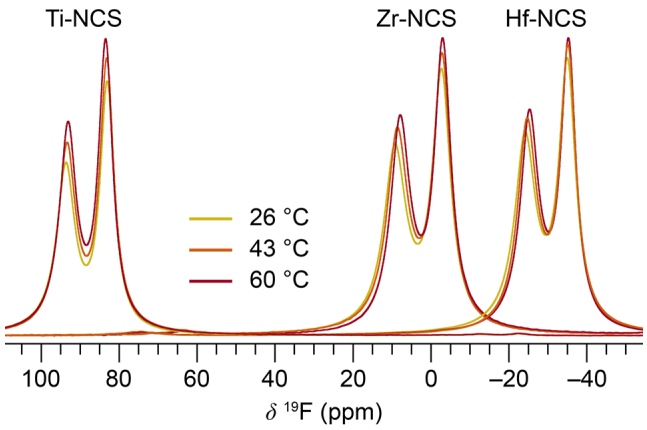

Figure 2.12. Elevated temperature ^{19}F MAS NMR of M-NCS phases (M = Ti, Zr, Hf). All three spectra evolve in a similar manner with the resonances shifting to lower frequency and narrowing as the temperature increases, indicative of rotational dynamics of the TiF_6^{2-} octahedra. The MAS rate was 40 kHz.

we hope to stimulate interest in racemic compounds with important properties that are dependent on the lack of crystallographic inversion symmetry.

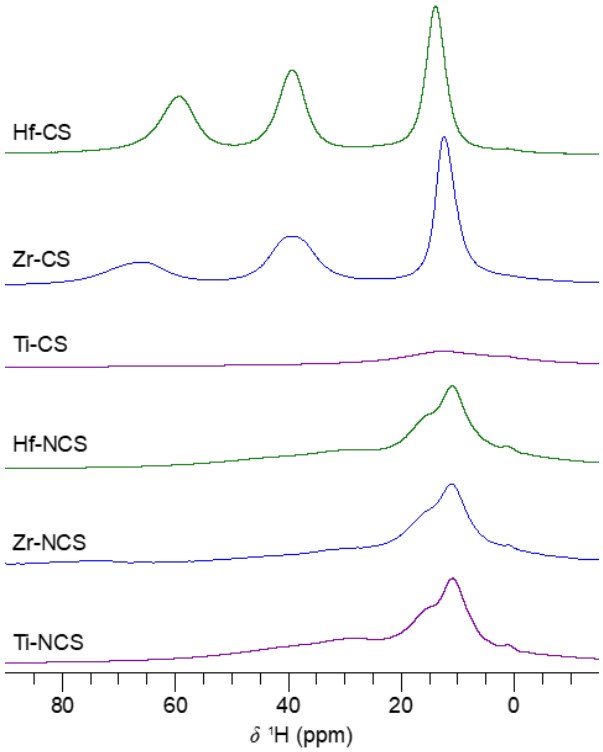

Figure 2.13. ^{1}H solid-state MAS NMR spectra of all M-CS and M-NCS phases (M = Ti, Zr, Hf). The MAS rate was 40 kHz and no spinning sidebands are visible in this window; small sidebands are present further out.

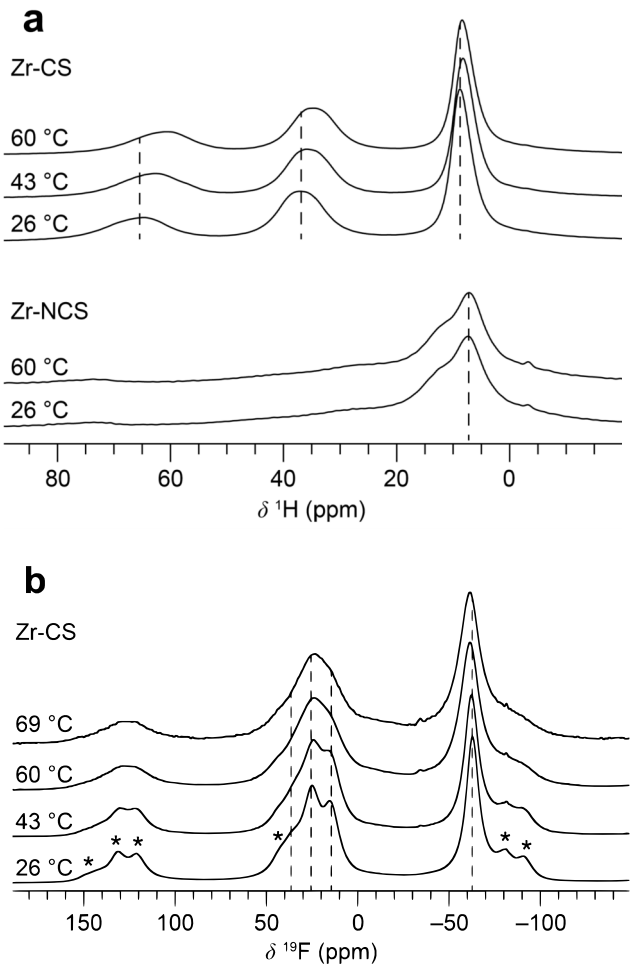

Figure 2.14. Elevated temperature (a) ^{1}H MAS NMR of the Zr-CS and Zr-NCS compounds and (b) ^{19}F MAS NMR of the Zr-CS compound. The Zr-CS ^{1}H and ^{19}F NMR showed shifts to lower frequencies with increasing temperature for the high frequency resonances; in both cases, the lowest frequency signals shifted slightly to higher frequency. No lineshape changes were observed in the ^{1}H spectra but the Zr-CS ^{19}F resonances between 10 and 40 ppm began to merge, which may be indicative of exchange. None of the M-NCS proton spectra changed with temperature (Zr-NCS shown here). The MAS rate was 40 kHz. Dashed lines serve as guides to the eye.

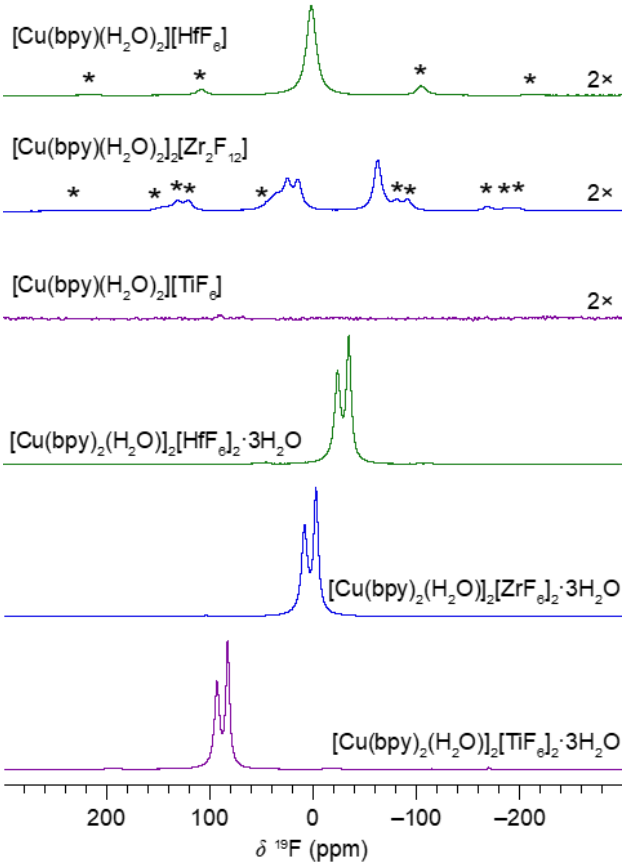

Figure 2.15. ^{19}F solid-state MAS NMR spectra of all M-CS and M-NCS phases (M = Ti, Zr, Hf). The CS compounds exhibit broader peaks—extremely broad in the Ti-CS case—so their intensity is scaled up by a factor of two for visualization. The MAS rate was 40 kHz and spinning sidebands are denoted with asterisks(*).

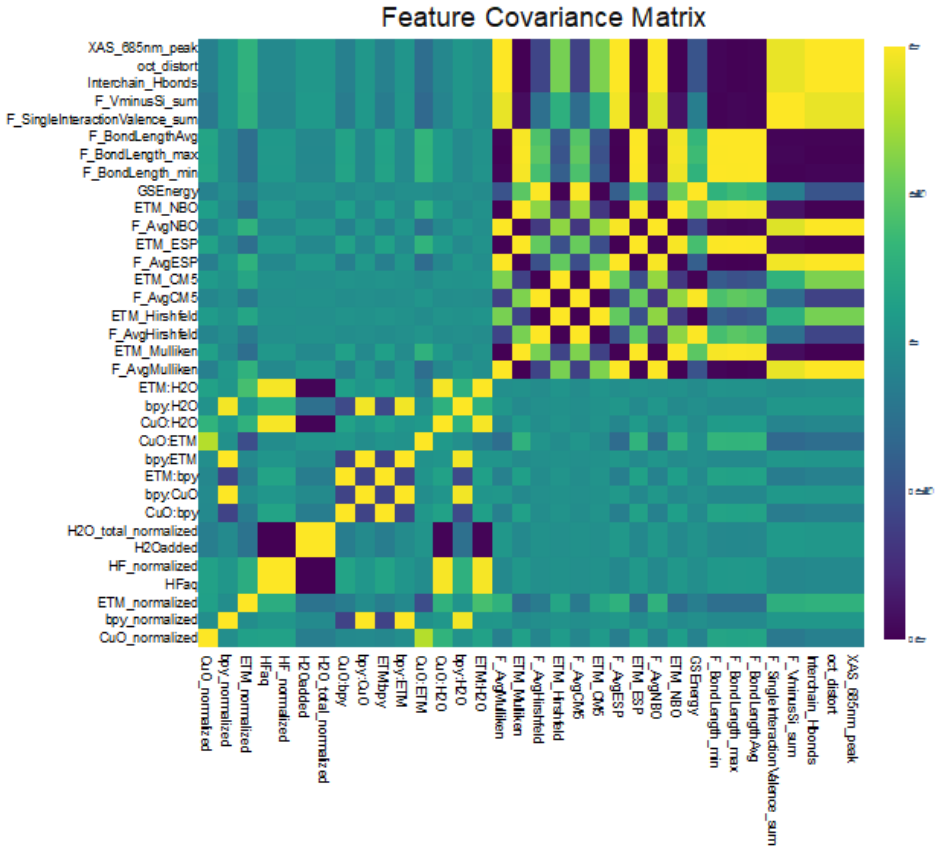

Figure 2.16. Feature covariance plotted using Pearson correlation coefficient. A value of "1" signifies positive linear correlation, "-1" signifies negative linear correlation, 0 indicates no correlation.

CHAPTER 3

Symmetry-Dependent Intermolecular π–π Stacking Directed by Hydrogen Bonding in Racemic Copper-Phenanthroline Compounds

This chapter was adapted with permission from:

Nisbet, M. L.; Wang, Y.; Poeppelmeier, K. R. Symmetry-Dependent Intermolecular $\pi - \pi$ Stacking Directed by Hydrogen Bonding in Racemic Copper-Phenanthroline Compounds. *Cryst. Growth Des.* **2021**, 21 (1), 552–562. https://doi.org/10.1021/acs.cgd.0c01355.

3.1. Abstract

We examine the role of molecular symmetry and hydrogen bonding in determining heterochiral intermolecular π–π stacking motifs in four racemic compounds with the formula $[Cu(phen)_2(H_2O)][MF_6]\cdot xH_2O$ (M = Ti, Zr, Hf ; phen = 1,10-phenanthroline) and two racemic compounds with the formula $Cu(phen)_2MF_6\cdot H_2O$ (M = Zr, Hf). In this work, equimolar combinations of C_2-symmetric Δ- and Λ-$Cu(phen)_2(H_2O)^{2+}$ complexes were found to organize via only face-to-face π–π stacking interactions to adopt a new horizontal packing motif in a series of compounds with the formula $[Cu(phen)_2(H_2O)][MF_6]\cdot xH_2O$ (M = Ti, Zr, Hf). Previously, Δ- and Λ-$Cu(phen)_2(H_2O)^{2+}$ complexes had been observed to pack with only parallel displaced π–π stacking interactions in a diagonal packing motif or with both face-to-face and parallel displaced π–π stacking interactions in a zigzag packing motif. The horizontal arrangement reported here is associated with the formation of hydrogen bonding

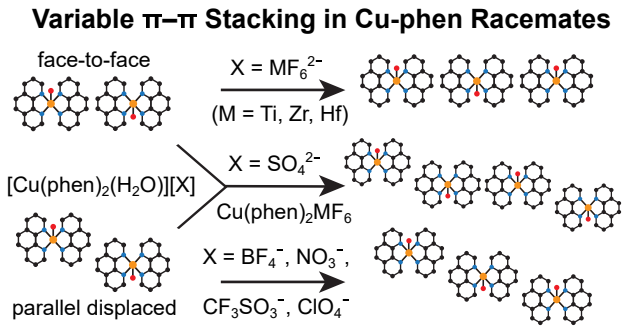

Figure 3.1. Racemic copper-phenanthroline compounds adopt three distinct intermolecular π–π packing motifs (horizontal, zigzag, and diagonal), which are dependent on composition, molecular symmetry, and hydrogen bonding interactions.

networks that link cations, anions, and hydrating water molecules within these structures. Equimolar combinations of neutral Δ- and Λ-$Cu(phen)_2MF_6$ (M = Zr, Hf) molecules organize in a zigzag stacking pattern that originates from the presence of both parallel displaced and face-to-face π–π stacking interactions. The symmetry of the $Cu(phen)_2MF_6$ molecule is reduced to C_1 by tilting of the bound MF_6^{2-} octahedron, which renders the two phen ligands symmetrically inequivalent.

3.2. Introduction

Noncovalent interactions such as π–π stacking and hydrogen bonding play a key role in determining structure, properties, and intermolecular symmetry in many systems.[124–130] In the design of noncentrosymmetric (NCS) materials, these interactions often dictate the presence or absence of inversion symmetry, which in turn determines nonlinear optical activity, piezoelectricity, and other properties.[2,53,131] The synthesis of NCS materials focuses on controlling the alignment of acentric functional building units, such as polar early transition metal (ETM) octahedra, conjugated planar groups, or tetrahedra.[37] Isolated ETM fluorides and oxide-fluorides can be synthesized in concentrated HF, which gives improved synthetic

control over the environment of these anions to optimize structure and properties in NCS structures.[66] The introduction of enantiomerically pure chiral templating agents (CTAs) ensures inversion symmetry breaking, but this method is limited by the requirement for enantiomeric purification.[17] Further, such a strategy does not control the cooperative polar alignment of FBUs, meaning that improved synthetic methods must be developed to precisely control the alignment of chiral and polar FBUs with noncovalent interactions.[18–21,77]

The use of racemic mixtures, or equimolar combinations of both enantiomers, of CTAs has been demonstrated as an emerging strategy for the synthesis of NCS materials.[22,26,30] While enantiomerically pure reagents require tedious separation and purification,[17,132,133] racemic mixtures of chiral molecules may be easily generated *in situ*. Notably, equimolar combinations of Δ- and Λ-$Cu(bpy)_2(H_2O)^{2+}$ complexes cooperatively align the polar moments of MF_6^{2-} (M= Ti, Zr, Hf; bpy = 2,2'-bipyridine) octahedra, which undergo polarizing out-of-center distortions owing to second-order Jahn-Teller effects.[22,49,112] Although most racemates crystallize with inversion symmetry and the chemical origins of inversion symmetry breaking in racemic compounds remain unclear, previous studies of materials based on ETM octahedra and chiral Δ- and Λ-$M(bpy)_x(H_2O)_y$ (M = Cu, Ni, Zn; x = 2, 3; y = 0, 1, 2) coordination complexes indicate that the racemic $[Cu(bpy)_2(H_2O)][MF_6]$ compounds possess a unique combination of cation symmetry and hydrogen bonding networks that give rise to polar NCS structures.[22,23] However, whereas the $[Cu(bpy)_2(H_2O)][MF_6]\cdot 1.5H_2O$ (M = Ti, Zr, Hf) compounds form polar NCS structures, centrosymmetry is always observed in the case of racemic Cu–phen compounds reported here.

Here, we elucidate the role of intermolecular π–π interactions in breaking inversion symmetry in racemic compounds by comparing the differences in π–π stacking between analogous complexes with bpy and phen ligands. Intermolecular π-π stacking interactions can

be understood in terms of four principle components: repulsion, induction, dispersion, and electrostatic interactions.[134,135] Examination of π–π stacking interactions in square planar metal complexes of 2,2'-bipyridine and 1,10-phenanthroline via both statistical analysis of observed stacking geometries and density functional theory calculations revealed that the strength of the stacking interaction increases as the surface area overlap increases when these ligands are bound to metal atoms.[136,137] However, factors such as the steric bulk of other ligands and other strong interactions in the structure often lead to geometries other than the most stable π–π stacking configuration being observed.

We report the structures of four racemic compounds based on Δ- and Λ-$Cu(phen)_2(H_2O)^{2+}$ cations and ETM fluoride MF_6^{2-} (M = Ti, Zr, Hf) anions and two racemic compounds based on neutral bridged Λ-shaped Δ- and Λ-$Cu(phen)_2(MF_6)$ (M = Zr, Hf) complexes. The $[Cu(phen)_2(H_2O)][MF_6]$ (M = Ti, Zr, Hf) compounds represent the first examples of C_2-symmetric Δ- and Λ-$Cu(phen)_2(H_2O)^{2+}$ units arranged exclusively by face-to-face stacking interactions to adopt a horizontal stacking pattern. This novel stacking motif occurs in the presence of extended hydrogen bonding networks between cations, anions, and free water molecules. Previously, only diagonal and zigzag arrangements had been observed, which are associated with the presence of only parallel displaced or both paralleled displaced and face-to-face stacking, respectively. Structures with only parallel displaced stacking geometries are observed in the presence of singly charged anions, which do not allow for the formation of extended hydrogen bonding networks, as seen in $[Cu(phen)_2(H_2O)][X]_2$, where X = BF_4^-, NO_3^-, $CF_3SO_3^-$, ClO_4^-.[138–140] Zigzag stacking occurs when both parallel displaced and face-to-face geometries are present in the same structure, which occurs in the two $Cu(phen)_2MF_6 \cdot H_2O$ (M = Zr, Hf) compounds reported here, as well as in the known compounds $[Cu(phen)_2(H_2O)][SO_4] \cdot 4H_2O$ and $[Cu(phen)_2(SO_4)](H_2O)_2$(dmf).[131] In these

structures, the symmetry of the chiral copper(II) complex is reduced from C_2 to C_1 by the tilting of the apical ligand, which renders the two phen ligands to be symmetrically inequivalent.

By comparing the structures of the racemic compounds reported in this work with the known compounds based on Δ- and Λ-Cu(phen)$_2$(H$_2$O)$^{2+}$ and Δ- and Λ-Cu(bpy)$_2$(H$_2$O)$^{2+}$ complexes, we identify the importance of non-parallel stacking between bpy ligands as a necessary albeit insufficient factor in breaking inversion symmetry within the bulk structure.

3.3. Methods

Caution: Hydrofluoric acid (HF) is toxic and corrosive! HF must be handled with extreme caution and the appropriate protective gear.

3.3.1. Materials

TiO_2 (Aldrich, 99.9+%), ZrO_2 (Alfa Aesar, 99.978%), HfO_2 (Aldrich, 98%), CuO (Sigma-Aldrich, ≥99.0%), 1,10-phenanthroline (phen) (Fisher, 99%), HF(aq) (Sigma-Aldrich, 48% wt. in H_2O, ≥99.99+% trace metals basis) were used as received. Reagent amounts of deionized water were used.

3.3.2. Hydrothermal Synthesis

The compounds reported here were synthesized via the hydrothermal pouch method.[69] In each reaction, reagents were heat sealed in Teflon pouches. Groups of six pouches were then placed into 125 mL Parr autoclaves with 40 mL distilled water as backfill. The autoclaves were heated at a rate of 5 °C/min to 150 °C and held at 150 °C for 24 h. The autoclaves

were allowed to cool to room temperature at a rate of 6 °C/h. Solid products were recovered by vacuum filtration.

Compound 3.1 $[Cu(phen)_2(H_2O)][TiF_6]\cdot H_2O$ was synthesized in a Teflon pouch containing 1.69 mmol CuO, 1.69 mmol TiO_2, 2.56 mmol phen, 1.0 mL (27.6 mmol) HF(aq), and 0.1 mL (5.6 mmol) H_2O.

Compound 3.2 $[Cu(phen)_2(H_2O)]_2[HfF_6]_2\cdot xH_2O$ was synthesized in a Teflon pouch containing 1.69 mmol CuO, 1.69 mmol HfO_2, 7.68 mmol phen, 1.0 mL (27.6 mmol) HF(aq) , and 0.1 mL (5.6 mmol) H_2O.

Compound 3.3 $[Cu(phen)_2(H_2O)][ZrF_6]\cdot 0.64H_2O$ was synthesized in a Teflon pouch containing 1.69 mmol CuO, 1.69 mmol ZrO_2, 2.56 mmol phen, 0.4 mL (11.0 mmol) HF(aq) , and 0.7 mL (38.9 mmol) H_2O.

Compound 3.4 $[Cu(phen)_2(H_2O)][HfF_6]\cdot 0.87H_2O$ was synthesized in a Teflon pouch containing 1.69 mmol CuO, 1.69 mmol HfO_2, 2.56 mmol phen, 0.2 mL (5.5 mmol) HF(aq), and 0.9 mL (50.0 mmol) H_2O.

Compound 3.5 $Cu(phen)_2ZrF_6\cdot H_2O$ was synthesized in a Teflon pouch containing 1.69 mmol CuO, 1.69 mmol ZrO_2, 5.12 mmol phen, 1.0 mL (27.6 mmol) HF(aq), and 0.1 mL (5.5 mmol) H_2O.

Compound 3.6 $Cu(phen)_2HfF_6\cdot H_2O$ was synthesized in a Teflon pouch containing 1.69 mmol CuO, 1.69 mmol HfO_2, 2.56 mmol phen, 0.8 mL (22.1 mmol) HF (aq), and 0.3 mL (16.7 mmol) H_2O.

3.3.3. Single-Crystal X-ray Diffraction

Single-crystal X-ray diffraction was used to determine the structure of each reported compound. Diffraction data for compounds 3.1, 3.2, 3.3, 3.5, and 3.6 was recorded on Bruker-APEX II CCD diffractometers at 100 K with monochromated Mo Kα radiation ($\lambda = 0.71073$ Å). SAINT was used for integration and multiscan absorption corrections were applied with SADABS.[93,94]

Diffraction data for compound 3.4 was recorded at 100 K on a Rigaku XtaLAB Synergy HyPix diffractometer with monochromated Mo Kα radiation ($\lambda = 0.71073$ Å). CrysAlisPro 1.171.40.68a was used for integration and scaling of the data.[141] A numerical absorption correction was applied based on Gaussian integration over a multifaceted crystal model with an empirical absorption correction using spherical harmonics, as implemented in the SCALE3 ABSPACK scaling algorithm.

All structures were solved with SHELXT and refined with SHELXL.[92] Hydrogen atom positions were assigned from difference map peaks where possible and omitted otherwise, with the exception of hydrogen atoms of 1,10-phenanthroline, which were constrained to ride at distances of 0.93 Å from the associated C atoms with $U_{iso}(H) = 1.5\ U_{eq}(C)$ within Olex2.[96] In cases where both hydrogen atoms of free water molecules could not be determined, we have reported only the oxygen atom position. No additional symmetry was found when checking for higher symmetry using PLATON..[95]

3.3.4. Descriptors for Intermolecular Interactions

Pairwise centroid–centroid distances were calculated for each pair of rings in adjacent phen ligands (e.g. phenyl–phenyl (d_{ph-ph}), pyridine–phenyl (d_{py-ph}), pyridine–pyridine (d_{py-py}))[131]

to classify π–π stacking arrangements between $Cu(phen)_2(H_2O)^{2+}$ or $Cu(phen)_2(MF_6)$ (M = Zr, Hf) fragments as either face-to-face or parallel displaced. The shorter distance is reported for structures with multiple values of d_{py-py} and d_{ph-py}. Figure 3.2 depicts representative face-to-face and parallel displaced interactions. Calculated centroid–centroid distances can be found in Table 3.4. A full listing of calculated descriptors for Compounds 1-6 and known $Cu(phen)_2(H_2O)^{2+}$ and $Cu(bpy)_2(H_2O)^{2+}$ compounds is given in Table 3.4, Table 3.6, and Table 3.7. We note that the measured interplanar distances between bpy and phen ligands fall within the range from 3.3 to 3.76 Å, which is near the center of the distribution of known interplanar distances in bpy and phen metal complexes.[136,137] The packing motif of a structure is assigned as horizontal if only face-to-face interactions are present, zigzag if both face-to-face and parallel displaced stacking interactions are present, and diagonal if only parallel displaced stacking interactions are present. A general schematic of the horizontal, zigzag, and diagonal packing motifs is shown in Figure 3.9.

Descriptors for hydrogen bonding interactions in Compounds 3.1–3.6 are provided in Table 3.5. A search of O–H$\cdots$F interactions among entries in the Cambridge Structural Database reveals an average O–F distance of 2.788 Åand a median distance of 2.802 Å.[142]

3.4. Results and Discussion

3.4.1. Structure Descriptions

Examination of the three (CuO, MO_2) / phen / HF(aq) (M = Ti, Zr, Hf) systems revealed four compounds based on racemic combinations of chiral Δ- and Λ-$Cu(phen)_2(H_2O)^{2+}$ cations.

Compound 3.1 has the formula $[Cu(phen)_2(H_2O)][TiF_6]\cdot H_2O$ and crystallizes in the space group $C2/c$. The structure of Compound 3.1 contains racemic combinations of C_2-symmetric

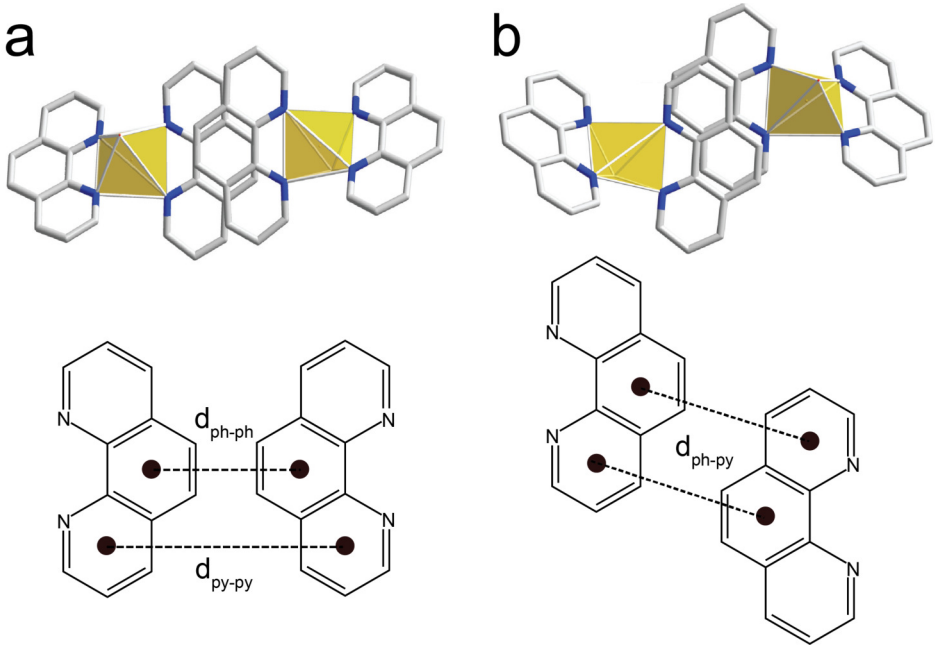

Figure 3.2. (a) Representative face-to-face $\pi - \pi$ stacking interaction between adjacent $Cu(phen)_2(H_2O)^{2+}$ cations. Interactions of this type can be identified by short d_{ph-ph} distances. (b) Representative parallel displaced $\pi - \pi$ stacking interaction between adjacent $Cu(phen)_2(H_2O)^{2+}$ cations. Interactions of this type can be identified by short d_{ph-py} distances.

Δ- and Λ-$Cu(phen)_2(H_2O)^{2+}$ complexes, which are organized into layers that stack along the *b* axis by homochiral and heterochiral π-π stacking interactions as well as hydrogen bonding with TiF_6^{2-} anions (3.3a). Adjacent layers of Δ- and Λ-$Cu(phen)_2(H_2O)^{2+}$ complexes are aligned in register such that parallel rows of Δ- and Λ-$Cu(phen)_2(H_2O)^{2+}$ complexes form along *a*. Each TiF_6^{2-} anion participates in hydrogen bonding with two $Cu(phen)_2(H_2O)^{2+}$ units of the same handedness and the free water molecule located between layers of $Cu(phen)_2(H_2O)^{2+}$ units. Two distinct face-to-face heterochiral stacking contacts are observed. These heterochiral stacking interactions result in the formation of extended Δu–Λd–Δu–Λd and Δd–Λu–Δd–Λu chains (u = up and d = down describe the orientation of these

Table 3.1. Crystallographic Data for Compounds 3.1 and 3.2

	Compound 3.1	Compound 3.2
Empirical formula	$C_{24}H_{20}CuF_6N_4O_2Ti$	$C_{24}H_{18}CuF_6N_4OHf$
Formula weight	621.88	734.45
Temperature/K	99.99	100.04
Crystal system	monoclinic	triclinic
Space group	$C2/c$	$P\bar{1}$
a/Å	19.6498(3)	12.6902(17)
b/Å	16.7910(2)	14.2854(19)
c/Å	14.0998(2)	16.910(2)
α/°	90	88.959(6)
β/°	95.7300(10)	70.804(6)
γ/°	90	67.426(6)
Volume/Å^3	4628.84(11)	2652.6(6)
Z	8	4
ρ_{calc} / g/cm^3	1.785	1.839
μ/mm^{-1}	1.345	4.778
F(000)	2504	1412
Crystal size/mm^3	0.11 × 0.081 × 0.056	0.198 × 0.149 × 0.11
Radiation	MoKα (λ = 0.71073 Å)	MoKα (λ = 0.71073 Å)
2θ range for data collection/°	3.198 to 61.188	2.57 to 62.006
Index ranges	-28 ≤ h ≤ 26, -24 ≤ k ≤ 23, -20 ≤ l ≤ 19	-18 ≤ h ≤ 18, -20 ≤ k ≤ 20, -24 ≤ l ≤ 24
Reflections collected	27520	193041
Independent reflections	7129 [R_{int} = 0.0430, R_{sigma} = 0.0404]	16583 [R_{int} = 0.0361, R_{sigma} = 0.0156]
Data/restraints/parameters	7129/0/359	16583/0/703
Goodness-of-fit on F^2	1.028	1.044
Final R indexes [I≥2σ (I)]	R_1 = 0.0383, wR_2 = 0.0948	R_1 = 0.0296, wR_2 = 0.0658
Final R indexes [all data]	R_1 = 0.0513, wR_2 = 0.1012	R_1 = 0.0315, wR_2 = 0.0669
Largest diff. peak/hole / e Å^{-3}	0.60/-0.78	3.38/-5.97

cations along the b direction). These stacking chains in which cations alternate in orientation and chirality have been shown to allow for optimal near-parallel stacking, while other arrangements with a single chirality or orientation give less favorable stacking interactions.[22] Homochiral π-π stacking between chains results in the formation of Δ–Δ and

Table 3.2. Crystallographic Data for Compounds 3.3 and 3.4

	Compound 3.3	Compound 3.4
Empirical formula	$C_{24}H_{18}CuF_6N_4O_{1.64}Zr$	$C_{24}H_{18}CuF_6N_4O_{1.87}Hf$
Formula weight	657.34	748.33
Temperature/K	100	100.01(10)
Crystal system	monoclinic	monoclinic
Space group	*P2/n*	*P2/n*
a/Å	11.6643(7)	11.7715(3)
b/Å	16.9423(10)	16.9235(3)
c/Å	12.8320(7)	12.8110(3)
α/°	90	90
β/°	109.6293(10)	109.839(3)
γ/°	90	90
Volume/Å^3	2388.5(2)	2400.67(10)
Z	4	4
ρ_{calc} / g/cm^3	1.828	2.070
μ/mm^{-1}	1.403	5.284
F(000)	1304	1440
Crystal size/mm^3	0.359 × 0.208 × 0.162	0.287 × 0.182 × 0.139
Radiation	MoKα (λ = 0.71073 Å)	MoKα (λ = 0.71073 Å)
2θ range for data collection/°	2.404 to 59.176	4.064 to 67.708
Index ranges	-15 ≤ h ≤ 16, -22 ≤ k ≤ 23, -16 ≤ l ≤ 17	-18 ≤ h ≤ 16, -25 ≤ k ≤ 24, -19 ≤ l ≤ 18
Reflections collected	26104	36266
Independent reflections	6698 [R_{int} = 0.0368, R_{sigma} = 0.0350]	8504 [R_{int} = 0.0339, R_{sigma} = 0.0329]
Data/restraints/parameters	6698/0/417	8504/4/401
Goodness-of-fit on F^2	1.030	1.046
Final R indexes [I≥2σ (I)]	R_1 = 0.0344, wR_2 = 0.0821	R_1 = 0.0341, wR_2 = 0.0857
Final R indexes [all data]	R_1 = 0.0482, wR_2 = 0.0883	R_1 = 0.0444, wR_2 = 0.0903
Largest diff. peak/hole / e Å^{-3}	0.54/-0.78	2.24/-1.99

Λ–Λ dimers, which display non-parallel stacking of both phen ligands bound to adjacent $Cu(phen)_2(H_2O)^{2+}$ complexes (Figure 3.3b). For the homochiral stacking interactions, one pair of phen ligands stacks in a face-to-face arrangement, while the other pair stacks in a displaced fashion.

Table 3.3. Crystallographic Data for Compounds 3.5 and 3.6

	Compound 3.5	Compound 3.6
Empirical formula	$C_{24}H_{16}CuF_6N_4OZr$	$C_{24}H_{16}CuF_6N_4OHf$
Formula weight	645.17	732.44
Temperature/K	100.04	99.99
Crystal system	monoclinic	monoclinic
Space group	$P2_1/n$	$P2_1/n$
a/Å	8.4159(2)	8.4064(10)
b/Å	14.3659(5)	14.3531(18)
c/Å	18.2917(6)	18.264(2)
α/°	90	90
β/°	99.9720(10)	99.946(3)
γ/°	90	90
Volume/Å^3	2178.09(12)	2170.5(5)
Z	4	4
ρ_{calc} / g/cm^3	1.967	2.241
μ/mm^{-1}	1.535	5.839
F(000)	1276	1404
Crystal size/mm^3	0.116 × 0.107 × 0.1	0.398 × 0.332 × 0.332
Radiation	MoKα (λ = 0.71073 Å)	MoKα (λ = 0.71073 Å)
2θ range for data collection/°	3.626 to 61.13	3.63 to 63.202
Index ranges	$-12 \leq h \leq 11$, $-18 \leq k \leq 20$, $-26 \leq l \leq 26$	$-12 \leq h \leq 8$, $-12 \leq k \leq 21$, $-19 \leq l \leq 26$
Reflections collected	19983	20665
Independent reflections	6649 [R_{int} = 0.0234, R_{sigma} = 0.0250]	7255 [R_{int} = 0.0134, R_{sigma} = 0.0145]
Data/restraints/parameters	6649/0/334	7255/0/334
Goodness-of-fit on F^2	1.034	1.169
Final R indexes [I$\geq 2\sigma$ (I)]	R_1 = 0.0229, wR_2 = 0.0599	R_1 = 0.0178, wR_2 = 0.0390
Final R indexes [all data]	R_1 = 0.0250, wR_2 = 0.0609	R_1 = 0.0198, wR_2 = 0.0395
Largest diff. peak/hole / e Å^{-3}	0.52/-0.67	0.63/-1.08

Compound 3.2 has the formula $[Cu(phen)_2(H_2O)][HfF_6]\cdot xH_2O$ and crystallizes in the space group $P\bar{1}$. The structure is analogous to the structure of 3.1 in that it contains racemic combinations of Δ- and Λ-$Cu(phen)_2(H_2O)^{2+}$ arranged into Δu–Λd–Δu–Λd and Δd–Λu–Δd–Λu chains and Δ–Δ and Λ–Λ dimers via π–π stacking and hydrogen bonding

Table 3.4. Heterochiral stacking interaction descriptors for Compounds 3.1–3.6. Two distinct stacking interactions were observed for each structure. The distances used to classify each phen–phen interaction are bolded for emphasis.

Compound #	d_{ph-py} (Å)	d_{py-py} (Å)	d_{ph-ph} (Å)	Stacking Type
3.1	3.7195(11)	4.2989(10)	**3.5112(10)**	face-to-face
	4.1429(11)	4.7265(11)	**3.5269(11)**	face-to-face
3.2	3.9877(17)	4.4328(16)	**3.5109(16)**	face-to-face
	3.8039(18)	4.6337(18)	**3.6242(17)**	face-to-face
3.3	3.9089(15)	4.4715(14)	**3.5123(14)**	face-to-face
	3.8695(13)	4.5123(13)	**3.5130(13)**	face-to-face
3.4	3.917(2)	4.459(2)	**3.507(2)**	face-to-face
	3.893(2)	4.536(2)	**3.523(2)**	face-to-face
3.5	3.7884(8)	3.7286(8)	**3.5527(8)**	face-to-face
	3.6019(8)	**3.7109(8)**	4.3379(8)	parallel displaced
3.6	3.7844(11)	3.7217(11)	**3.5508(11)**	face-to-face
	3.5976(11)	**3.7051(11)**	4.3306(11)	parallel displaced

(Figure 3.4). Whereas the layers of Δ- and Λ-$Cu(phen)_2(H_2O)^{2+}$ are aligned to form parallel rows of Δ- and Λ-$Cu(phen)_2(H_2O)^{2+}$ complexes in Compound 3.1, adjacent layers are shifted along c in an offset fashion in Compound 3.2 to give an alternating "brickwork" arrangement. Two distinct HfF_6^{2-} anions are present in the asymmetric unit. Each HfF_6^{2-} anion participates in two hydrogen bonds with two $Cu(phen)_2(H_2O)^{2+}$ units of the same handedness. The $Hf(2)F_6^{2-}$ anion displays disorder on the F11 and F12 sites. A solvent mask was applied during the refinement to model disordered free water molecules present in the structure. These free water molecules are packed between the hydrogen-bonded layers of $Cu(phen)_2(H_2O)^{2+}$ and HfF_6^{2-} units. Compound 3.2 contains two types of heterochiral face-to-face stacking interactions. Both homochiral stacking interactions exhibit a displaced arrangement.

Compound 3.3 has the formula $[Cu(phen)_2(H_2O)][ZrF_6]\cdot 0.64H_2O$ and crystallizes in the space group $P2/n$. Hydrogen bonding and π-π stacking interactions dictate the assembly

Table 3.5. Hydrogen bonding interactions in Compounds 3.1-3.6.

Compound 3.1

D	**H**	**A**	**d(D-H)/Å**	**d(H-A)/Å**	**d(D-A)/Å**	**D-H-A/°**
O1	H1A	F1	0.79(3)	1.79(4)	2.574(2)	170(3)
O1	H1B	F3	0.80(3)	1.82(3)	2.619(2)	176(3)
O2	H2A	F4	0.97(4)	1.81(4)	2.755(2)	162(3)

Compound 3.2

D	**H**	**A**	**d(D-H)/Å**	**d(H-A)/Å**	**d(D-A)/Å**	**D-H-A/°**
O1	H1A	F8	0.70(6)	1.90(6)	2.602(3)	175(6)
O1	H1B	F1	0.75(5)	1.90(5)	2.643(3)	172(5)
O2	H2A	F10	0.76(5)	1.89(5)	2.655(3)	175(5)
O2	H2B	F3	0.74(5)	1.90(5)	2.638(3)	171(5)

Compound 3.3

D	**H**	**A**	**d(D-H)/Å**	**d(H-A)/Å**	**d(D-A)/Å**	**D-H-A/°**
O1	H1A	F3B	0.75(3)	1.72(4)	2.470(5)	171(3)
O1	H1A	F3A	0.75(3)	1.98(4)	2.695(7)	160(3)
O1	H1B	F2B	0.70(3)	2.02(4)	2.72(3)	177(3)
O1	H1B	F2A	0.70(3)	1.77(4)	2.46(2)	168(4)
O2	-	F6A	-	-	2.724(5)	-
O3	-	F5B	-	-	2.59(6)	-

Compound 3.4

D	**H**	**A**	**d(D-H)/Å**	**d(H-A)/Å**	**d(D-A)/Å**	**D-H-A/°**
O1	H1A	F4A	0.843(19)	1.69(2)	2.499(7)	161(5)
O1	H1A	F4B	0.843(19)	1.90(2)	2.722(12)	164(4)
O1	H1B	F1	0.817(19)	1.784(19)	2.598(4)	174(4)
O2	-	F6B	-	-	2.716(7)	-
O3	-	F3A	-	-	2.661(12)	-

Compound 3.5

D	**H**	**A**	**d(D-H)/Å**	**d(H-A)/Å**	**d(D-A)/Å**	**D-H-A/°**
O1	-	F2	-	-	2.4454(16)	-

Compound 3.6

D	**H**	**A**	**d(D-H)/Å**	**d(H-A)/Å**	**d(D-A)/Å**	**D-H-A/°**
O1	-	F2	-	-	2.442(2)	-

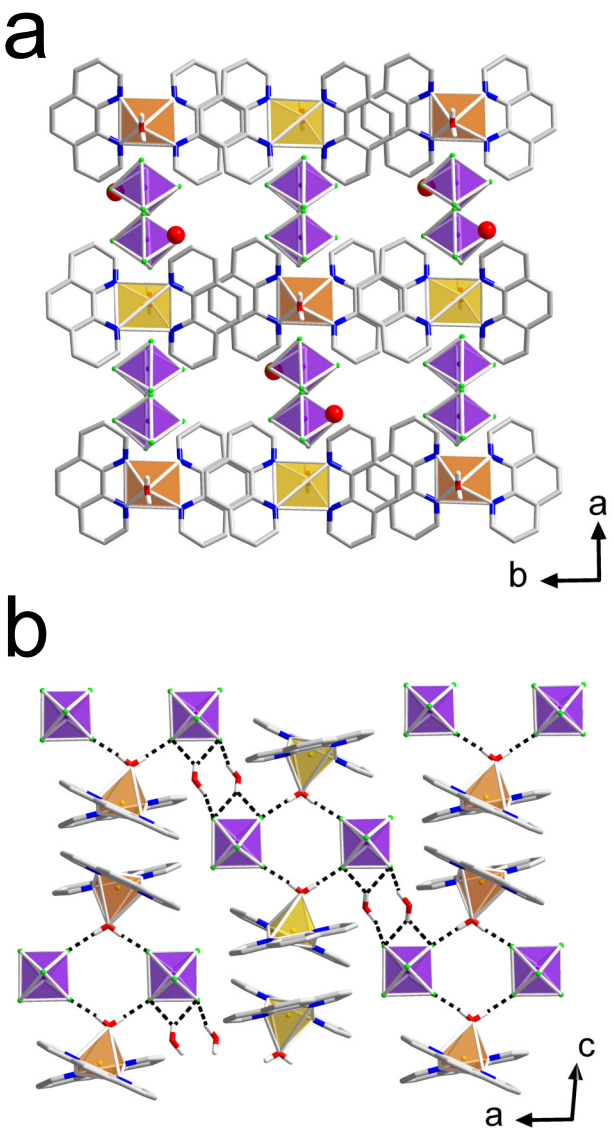

Figure 3.3. (a) Structural diagram showing the face-to-face stacking interactions in the structure of Compound 3.1. (b) Hydrogen bonds within the structure are depicted as dashed lines. Orange polyhedra represent Λ-Cu(phen)$_2$(H$_2$O)$^{2+}$ cations, gold polyhedra represent Δ-Cu(phen)$_2$(H$_2$O)$^{2+}$ cations, and purple polyhedra represent TiF_6^{2-} anions.

of Cu(phen)$_2$(H$_2$O)$^{2+}$ and ZrF_6^{2-} units within the structure of 3.3 into both Δu–Λd–Δu–Λd and Δd–Λu–Δd–Λu chains and Δ–Δ and Λ–Λ dimers (Figure 3.5). Layers of Δ- and Λ-Cu(phen)$_2$(H$_2$O)$^{2+}$ complexes are aligned in register, as seen in Compound 3.1. Disorder

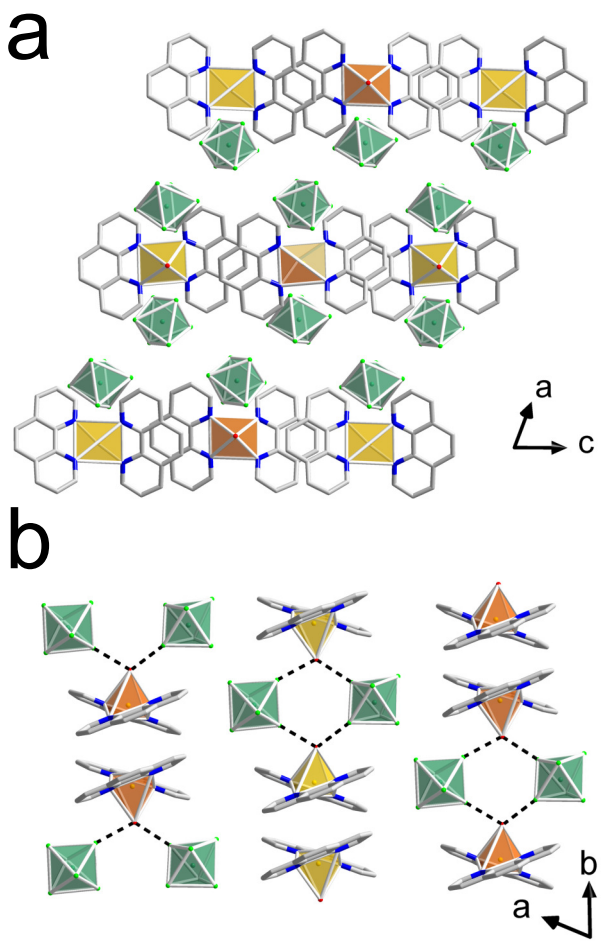

Figure 3.4. (a) Structural diagram showing the face-to-face stacking interactions in the structure of Compound 3.2. (b) Hydrogen bonds within the structure are depicted as dashed lines. Orange polyhedra represent Λ-$Cu(phen)_2(H_2O)^{2+}$ cations, gold polyhedra represent Δ-$Cu(phen)_2(H_2O)^{2+}$ cations, and green polyhedra represent HfF_6^{2-} anions.

is present at 3 F sites in the ZrF_6^{2-} octahedron. In this structure, the ZrF_6^{2-} anions participate in two hydrogen bonds with $Cu(phen)_2(H_2O)^{2+}$ units of the same handedness and two hydrogen bonds with free water molecules. The free O2 water molecule is fully occupied, while the free O3 water molecule has a partial occupancy of 0.14. Two distinct heterochiral stacking interactions with face-to-face configurations are observed within Δu–Λd–Δu–Λd and

Δd–Λu–Δd–Λu chains in 3. The homochiral stacking interactions include one face-to-face contact and one slightly displaced contact.

Compound 3.4 has the formula $[Cu(phen)_2(H_2O)][HfF_6]\cdot 0.87H_2O$ and is isostructural to Compound 3.3 with the exception of the difference in occupancy of free O3 water molecule, which has a partial occupancy of 0.37 in Compound 3.4.

In addition to the four racemic compounds based on $Cu(phen)_2(H_2O)^{2+}$ cations, our investigation also produced two isostructural racemates with the formula $Cu(phen)_2MF_6\cdot H_2O$ (M = Zr, Hf) in which the $MF_6{}^{2-}$ octahedron is directly bound in the apical site of the neutral Δ- and Λ-$Cu(phen)_2MF_6$ complexes.

Compound 3.5 has the formula $Cu(phen)_2ZrF_6\cdot H_2O$ and crystallizes in the space group $P2_1/n$. The structure of 3.5 contains racemic combinations of Δ- and Λ-$Cu(phen)_2ZrF_6$ units, which adopt bent Λ-shaped configurations, and a free water molecule (Figure 3.6).[143] Each $Cu(phen)_2ZrF_6$ unit participates in hydrogen bonding with a free water molecule. $Cu(phen)_2ZrF_6$ units are involved in face-to-face and parallel displaced heterochiral stacking interactions and form Δu–Λd–Δu–Λd chains. Notably, the apical $ZrF_6{}^{2-}$ octahedron is tilted toward the phenanthroline ligand that participates in a face-to-face stacking interaction (Figure 3.10). Homochiral stacking is absent from the structure, and thus Δ–Δ and Λ–Λ dimers do not form. Previous studies of stacking in square planar metal complexes of phen indicate that the formation of π–π stacking chains, in which each phen ligand participates in two stacking interactions, are heavily favored over stacking dimers, in which each phen ligand participates in only one stacking interaction, in known structures. However, in Compound 3.5, the steric bulk of the bound $MF_6{}^{2-}$ octahedron disrupts the stacking landscape such that each phen ligand only participates in one stacking interaction.

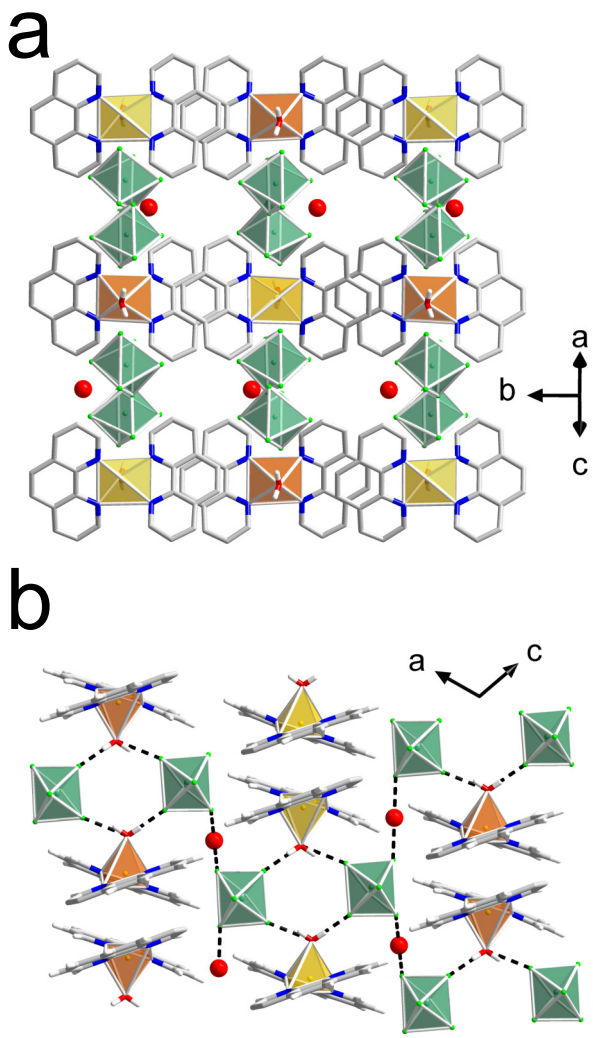

Figure 3.5. (a) Structural diagram showing the face-to-face stacking interactions in the structure of Compounds 3.3 and 3.4. (b) Hydrogen bonds within the structure are depicted as dashed lines. Orange polyhedra represent Λ-$Cu(phen)_2(H_2O)^{2+}$ cations, gold polyhedra represent Δ-$Cu(phen)_2(H_2O)^{2+}$ cations, and green polyhedra represent HfF_6^{2-} anions.

Compound 3.6 has the formula $Cu(phen)_2HfF_6 \cdot H_2O$ and is isostructural to compound 3.5.

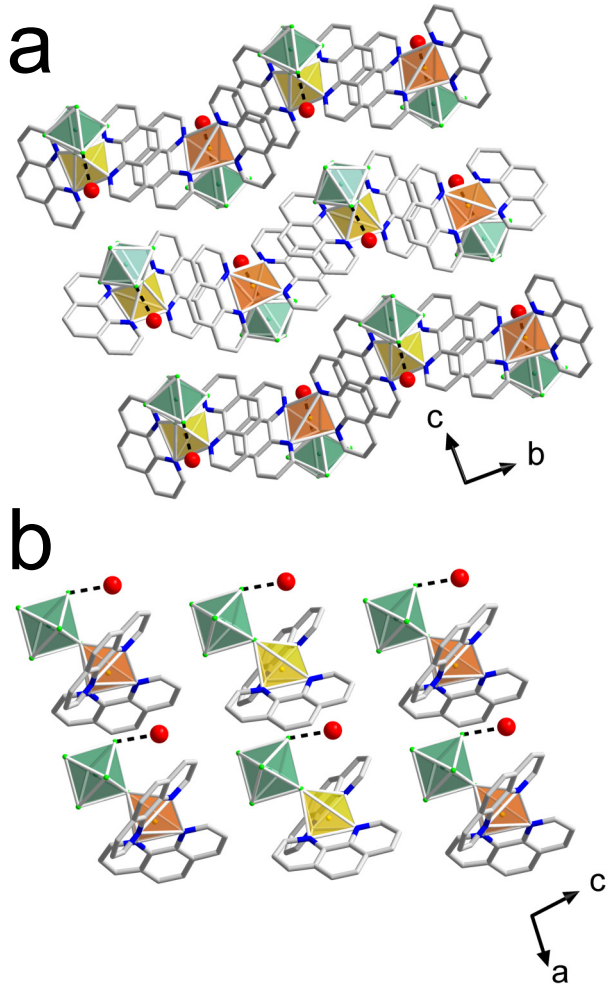

Figure 3.6. Structural diagram showing the face-to-face and parallel displaced stacking interactions in the structure of Compounds 3.5 and 3.6. (b) Hydrogen bonds within the structure are depicted as dashed lines. Orange polyhedra represent Λ-$Cu(phen)_2(H_2O)^{2+}$ cations, gold polyhedra represent Δ-$Cu(phen)_2(H_2O)^{2+}$ cations, and green polyhedra represent HfF_6^{2-} anions.

3.4.2. $\pi - \pi$ Stacking Motifs in Racemic Copper-Phenanthroline Compounds

In addition to the structures reported above, we examined the five other known compounds based on racemic combinations of $Cu(phen)_2(H_2O)^{2+}$ units to understand stacking motifs in these racemic compounds: $[Cu(phen)_2(H_2O)][SO_4]\cdot 4H_2O$ (CSD refcode: MUNHUA),[131]

$[Cu(phen)_2(H_2O)][NO_3]_2$ (CSD refcode: APENCU),[138] $[Cu(phen)_2(H_2O)][ClO_4]_2$ (CSD refcode: KOWFEH),[140] $[Cu(phen)_2(H_2O)][BF_4]_2$ (CSD refcode: APOLCU),[139] and $[Cu(phen)_2(H_2O)][CF_3SO_3]_2$ (CSD refcode: NEHXAZ).[140]

Stacking patterns in racemic Cu-phen compounds can be classified into three general categories: horizontal, zigzag, and diagonal. Horizontal stacking (shown in Figure 3.3) occurs when only face-to-face stacking interactions are present, as seen in Compounds 3.1, 3.2, 3.3, and 3.4. Zigzag configurations are found when both face-to-face and parallel displaced interactions are present in the same structure (Figure 3.6), as seen here in Compounds 3.5 and 3.6 and in the known compound MUNHUA. Diagonal stacking (Figure 3.7) occurs when only parallel displaced stacking interactions are present and is observed in the known APENCU, KOWFEH, APOLCU, and NEHXAZ compounds listed above.

Diagonal and horizontal packed structures can be distinguished by the absence or presence of extended hydrogen bonding networks, respectively. Hydrogen bonding in these structures is largely dependent on the charge of the anion. In $Cu(phen)_2(H_2O)^{2+}$ compounds with MF_6^{2-} or SO_4^{2-} anions, cations and anions are present in a 1:1 ratio. In contrast, compounds with NO_3^-, $CF_3SO_3^-$, BF_4^-, and ClO_4^- anions have a cation:anion ratio of 1:2. This distinction has profound consequences on the hydrogen bonding in the structure, which can be understood in terms of the numbers of hydrogen bond donors and acceptors present. In all known compounds that include $Cu(phen)_2(H_2O)^{2+}$, each bound water molecule participates in two hydrogen bonding interactions. In compounds with a 1:1 cation:anion ratio, each anion participates in two hydrogen bonding interactions with $Cu(phen)_2(H_2O)^{2+}$ units to fulfill the hydrogen bonding preference of the apical bound water molecules on the cations, whereas in the 1:2 compounds each anion can only participate in one hydrogen bonding interaction. The formation of $Cu(phen)_2(H_2O)^{2+} \cdots MF_6^{2-} \cdots Cu(phen)_2(H_2O)^{2+}$ clusters

in the 1:1 compounds allows this condition to be satisfied. These clusters form between adjacent Δu–Λd–Δu–Λd and Δd–Λu–Δd–Λu stacking chains.

To distinguish zigzag packed structures from the horizontal and diagonal packing archetypes, the symmetry of the cation must also be considered. Just as the symmetry of the C_2-symmetric $Cu(phen)_2(H_2O)^{2+}$ complexes tends to be maintained in the stacking interactions of these cations (only face-to-face or only parallel displaced), the lower symmetry of C_1-symmetric $Cu(phen)_2MF_6$ complexes is reflected in their stacking interactions, with each phen ligand involved in a distinct stacking geometry (both face-to-face and parallel displaced in the same compound). In $Cu(phen)_2MF_6$ (M = Zr, Hf) and $[Cu(phen)_2(H_2O)][SO_4]\cdot 4H_2O$, the symmetry of the cation is reduced from C_2 to C_1 owing to the tilting of the apical ligand toward the phen ligand that participates in face-to-face stacking. The tilting of the apical ligand is associated with distinct hydrogen bonding interactions found in these compounds relative to the known Cu–phen racemates with horizontal or diagonal packing. For $Cu(phen)_2MF_6$ (M = Zr, Hf), the apical $MF_6{}^{2-}$ group participates in a single hydrogen bond with a free water molecule (Figure 3.6). Similarly, in $[Cu(phen)_2(H_2O)][SO_4]\cdot 4H_2O$, the $SO_4{}^{2-}$ group bridges between adjacent $Cu(phen)_2(H_2O)^{2+}$ cations, analogous to the bridging interactions found in the horizontal packed compounds, but in this case the bridging occurs through hydrogen bonding with a single oxide ligand rather than two fluoride ligands (Figure 3.8).

The dependence of stacking geometry in chiral Cu–phen complexes on molecular symmetry is well-illustrated by $[Cu(phen)_2(SO_4)](H_2O)_2(dmf)$ (CSD refcode: MUNHOU) and $[Cu(phen)_2(SO_4)]CH_3OH$ (CSD refcode: MUNHIO). The structure of MUNHIO contains only parallel displaced stacking interactions to give a diagonal stacking arrangement as

$Cu(phen)_2(SO_4)$ molecules occupy two-fold axes and retain C_2 symmetry, which is facilitated by symmetric disorder of the apical SO_4^{2-} ligand. The symmetric disorder is supported by the disorder of the solvating methanol molecule that occupies the same two fold axes, resulting in symmetric hydrogen bonding contacts between SO_4^{2-} and methanol. In contrast, although the apical SO_4^{2-} ligand is also disordered in MUNHOU, $Cu(phen)_2(SO_4)$ molecules in this compound participate in both face-to-face and parallel displaced stacking interactions to give a zigzag stacking arrangement. In this case, the ligand participates in hydrogen bonding contacts with ordered hydrating water molecules to lower the symmetry of the $Cu(phen)_2(SO_4)$ molecule from C_2 to C_1.

3.4.3. Inversion Symmetry in Racemic $Cu(L)_2(H_2O)^{2+}$ (L = phen or bpy) Compounds

To elucidate how local π–π stacking interactions contribute to the preservation or breaking of crystallographic inversion symmetry in racemic compounds, we compared the structures of compounds based on Δ- and Λ-$Cu(phen)_2(H_2O)^{2+}$ and Δ- and Λ-$Cu(bpy)_2(H_2O)^{2+}$ complexes. Although Δ- and Λ-$Cu(L)_2(H_2O)^{2+}$ (L = bpy, phen) units in these racemates participate in both homochiral and heterochiral π–π stacking interactions, here we discuss only the heterochiral interactions as these interactions can involve symmetry relations of the second kind (inversion, mirror/glide, rotoinversion) while homochiral stacking interactions cannot.

Whereas adjacent phen ligands are always parallel (displaced and face-to-face) when involved in stacking interactions between nearest neighbor $Cu(phen)_2(H_2O)^{2+}$ complexes, parallel displaced, non-parallel displaced, and non-parallel face-to-face arrangements are observed between nearest neighbors for $Cu(bpy)_2(H_2O)^{2+}$ units. Nearest neighbor $Cu(bpy)_2(H_2O)^{2+}$ complexes are related by inversion symmetry in $[Cu(bpy)_2(H_2O)][S_5O_6]$

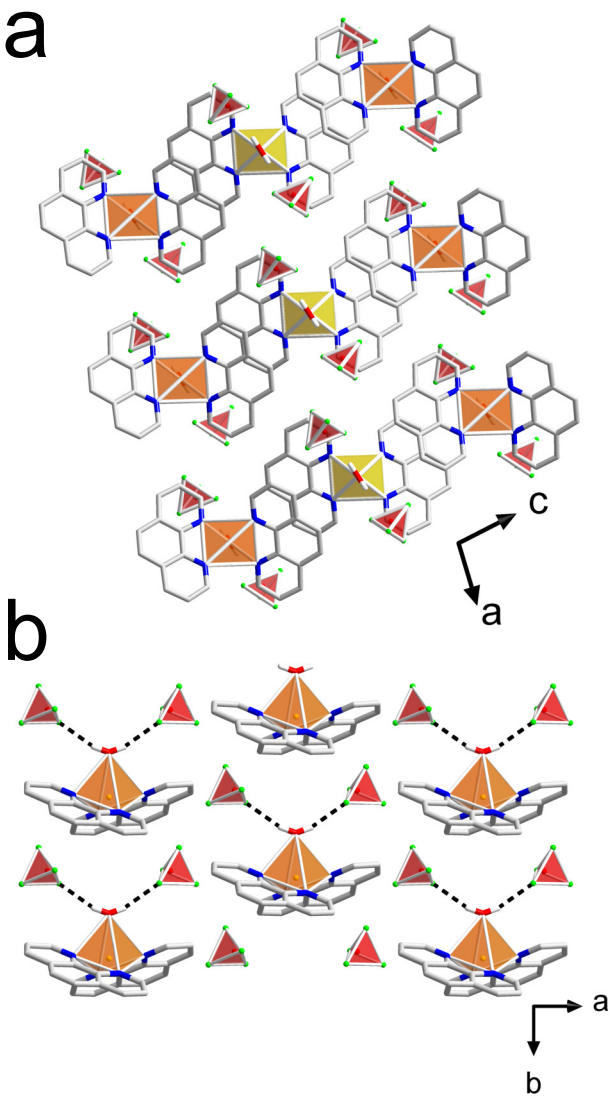

Figure 3.7. Structural diagram showing the parallel displaced stacking interactions in the structure of $[Cu(phen)_2(H_2O)][BF_4]_2$ (APOLCU) and other reported $Cu(phen)_2(H_2O)^{2+}$ compounds. (b) Hydrogen bonds within the structure are depicted as dashed lines. Orange polyhedra represent Λ-$Cu(phen)_2(H_2O)^{2+}$ cations, gold polyhedra represent Δ-$Cu(phen)_2(H_2O)^{2+}$ cations, and red polyhedra represent BF_4^- anions.

(CSD refcode: BPACUS) and $[Cu(bpy)_2(H_2O)][S_2O_6]$ (CSD refcode: BPACUT), where $\pi-\pi$ stacking interactions are absent from the structure of BPACUS and parallel displaced stacking interactions are observed in BPACUT. Non-parallel configurations of bpy ligands in

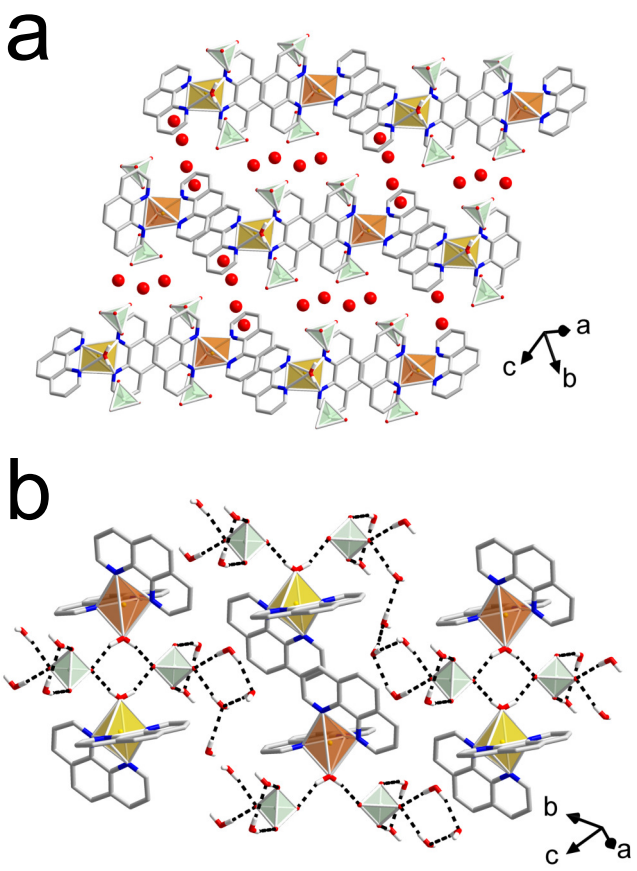

Figure 3.8. Structural diagram showing the face-to-face and parallel displaced stacking interactions in the structure of $[Cu(phen)_2(H_2O)][SO_4]\cdot 4H_2O$ (MUNHUA). (b) Hydrogen bonds within the structure are depicted as dashed lines. Orange polyhedra represent Λ-$Cu(phen)_2(H_2O)^{2+}$ cations, gold polyhedra represent Δ-$Cu(phen)_2(H_2O)^{2+}$ cations, and light green polyhedra represent $SO_4{}^{2-}$ anions.

adjacent $Cu(bpy)_2(H_2O)^{2+}$ complexes preclude the possibility of inversion centers relating nearest neighbors that are opposite enantiomers. Non-parallel arrangements between nearest neighbors can lead to non-nearest neighbors being related only by glide planes, as observed in the $[Cu(bpy)_2(H_2O)][MF_6]\cdot 1.5H_2O$ (M= Ti, Zr, Hf) family (CSD refcodes: YUGYEH, YUGYOR, YUGYIL) in which all stacking interactions are nonparallel and the structure is noncentrosymmetric.[22,112] In $[Cu(bpy)_2(H_2O)][BF_4]_2$ (CSD refcode: VIKDOJ) and

$[Cu(bpy)_2(H_2O)][PF_6]_2$ (CSD refcode: EQIQOL), the $\pi - \pi$ stacking interaction is nonparallel with the nearest neighbor but parallel with the second nearest neighbor, giving rise to a centrosymmetric structure despite the noncentrosymmetric non-parallel local arrangement. In contrast, stacking interactions between $Cu(phen)_2(H_2O)^{2+}$ are always parallel, and heterochiral pairs are most commonly arranged across inversion centers.

The difference in stacking behavior between the racemic copper(II) complexes of phen and bpy may stem from the difference in available surface area. Previous studies of metal complexes of bpy and phen have shown that the π–π interaction strength increases with increasing surface area, which suggests that stacking interactions between phen ligands are likely to be stronger than those between bpy ligands due to larger surface area. In the case of strong stacking interactions between phen ligands, a parallel geometry allows for these interactions to be optimized. For bpy ligands, however, the weaker stacking interaction allows for other interactions in the structure to direct the packing landscape and can more easily bring the stacking geometry into a nonparallel configuration that can lead to broken local inversion symmetry.[136,137]

While the presence of non-parallel stacking between chiral $Cu(L)_2(H_2O)^{2+}$ (L = bpy, phen) complexes does not guarantee inversion symmetry breaking, this reduces the number of possible configurations that lead to inversion symmetry. In both known structures where non-parallel interactions are present between nearest neighbors, local inversion symmetry is broken although the second nearest neighbors are related by inversion in the VIKDOJ and EQIQOL structures. Thus, encouraging these non-parallel stacking interactions will lead to an increased likelihood of achieving an NCS structure in racemic compounds by breaking local inversion symmetry.

3.5. Conclusions

In this study, we report the structures of six novel racemic compounds based on complexes of copper(II) and 1,10-phenanthroline. Racemic combinations of C_2-symmetric Δ- and Λ-$Cu(phen)_2(H_2O)^{2+}$ cations found in $[Cu(phen)_2(H_2O)][TiF_6]\cdot H_2O$, $[Cu(phen)_2(H_2O)][HfF_6]\cdot xH_2O$, $[Cu(phen)_2(H_2O)][ZrF_6]\cdot 0.64H_2O$, and $[Cu(phen)_2(H_2O)][HfF_6]\cdot 0.87H_2O$ display only face-to-face $\pi - \pi$ stacking interactions, which gives rise to a horizontal packing arrangement that is unique among all known racemic $Cu(phen)_2(H_2O)^{2+}$ compounds. Comparison with previously reported racemic $Cu(phen)_2(H_2O)^{2+}$ compounds with singly charged anions illustrates the key role of hydrogen bonding in determining the packing architectures in these compounds, as compounds without extended hydrogen bonding networks are arranged via only parallel displaced stacking interactions. Cation symmetry was also found to strongly influence $\pi - \pi$ stacking interactions in $Cu(phen)_2ZrF_6\cdot H_2O$ and $Cu(phen)_2HfF_6\cdot H_2O$. Racemic combinations of Δ- and Λ-$Cu(phen)_2MF_6$ (M = Zr, Hf) complexes are arranged via both face-to-face and parallel displaced $\pi - \pi$ stacking interactions as a consequence of the tilting of the apical ligand, which lowers the local point group symmetry of the chiral species to C_1.

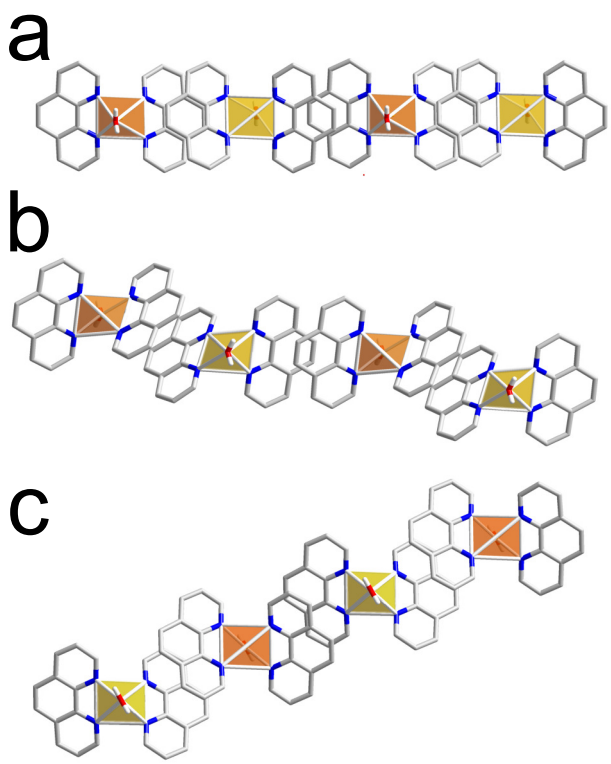

[p]

Figure 3.9. General schematic of (a) horizonal, (b) zigzag, and (c) diagonal stacking motifs observed in copper-phenanthroline racemates.

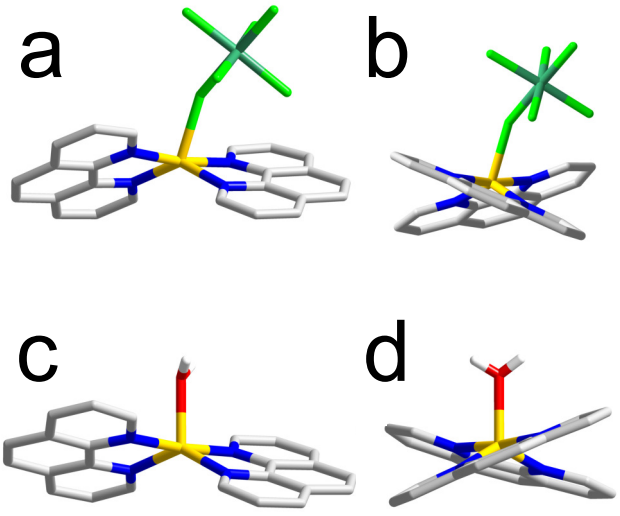

Figure 3.10. Depiction of the relative tilt of the apical ligand in (a) (b) $Cu(phen)_2MF_6$ (M = Zr, Hf) relative to (c) (d) $Cu(phen)_2(H_2O)^{2+}$.

Table 3.6. Descriptors of $\pi - \pi$ Stacking Interactions in Known $Cu(phen)_2(H_2O)^{2+}$ and $Cu(bpy)_2(H_2O)^{2+}$ Compounds

REFCODE	type	d_{ph-py} (Å)	d_{py-py} (Å)	d_{ph-ph} (Å)	interplanar angle (°)
APOLCU	Parallel displaced	3.694	4.298	4.525	0
APOLCU	Parallel displaced	5.269	4.954	6.528	0
NEHXAZ	Parallel displaced	3.832	4.047	3.786	0
MUNHUA	Face-to-face	3.797	4.443	3.548	0
MUNHUA	Parallel displaced	3.666	3.741	3.822	0
KOWFEH	Parallel displaced	3.622	4.124	4.569	0
APENCU	Parallel displaced	3.574	4.16	4.451	0
APENCU	Parallel displaced	4.79	4.301	6.242	0
GESHOD	Face-to-face	3.934	3.604	3.495	2.85
GESHOD	Parallel displaced	3.478	3.813	4.697	3.43
VIKDOJ	Face-to-face	4.2	4.917	3.556	2.86
VIKDOJ	Parallel displaced	3.601	4.053	4.619	0
MUNHIO	Parallel displaced	3.539	4.207	3.97	0
MUNHOU	Face-to-face	4.102	4.002	3.468	0
MUNHOU	Parallel displaced	3.81	3.706	5.182	0

Table 3.7. Descriptors of $\pi - \pi$ Stacking Interactions in Compounds 3.1 – 3.6

Compound number	type	interplanar distance (Å)	Cu-Cu distance (Å)	interplanar angle (°)
3.1	Face-to-face	3.386	8.426	0
3.1	Face-to-face	3.369	9.084	0
3.2	Face-to-face	3.421	8.719	0
3.2	Face-to-face	3.352	8.862	0
3.3 + 3.4	Face-to-face	3.429	8.695	0
3.3 + 3.4	Face-to-face	3.306	8.899	0
3.5 + 3.6	Face-to-face	3.362	7.912	0
3.5 + 3.6	Parallel displaced	3.41	6.986	0

CHAPTER 4

Crystal Structures of Three Copper(II)-2,2'-bipyridine (bpy) Compounds, $[Cu(bpy)_2(H_2O)][SiF_6]\cdot 4H_2O$, $Cu(bpy)_2(TaF_6)_2$, and $[Cu(bpy)_3][TaF_6]_2$, and a Related Coordination Polymer, $[Cu(bpy)(H_2O)_2(SnF_6)]_n$

This chapter was adapted with permission from:

Nisbet, M. L.; Hiralal, E.; Poeppelmeier, K. R. Crystal Structures of Three Copper(II)–2,2'-Bipyridine (Bpy) Compounds, $[Cu(Bpy)_2(H_2O)][SiF_6]\cdot 4H_2O$, $[Cu(Bpy)_2(TaF_6)_2]$ and $[Cu(Bpy)_3][TaF_6]_2$ and a Related Coordination Polymer, $[Cu(Bpy)(H_2O)_2(SnF_6)]_n$. *Acta Crystallogr., Sect. E: Crystallogr. Commun.* **2021**, 77 (2), 158–164. https://doi.org/10.1107/S2056989021000633.

4.1. Abstract

We report the hydrothermal syntheses and crystal structures of aquabis(2,2'-bipyridine)copper(II) hexafluorosilicate tetrahydrate $[Cu(bpy)_2(H_2O)][SiF_6]\cdot 4H_2O$, (compound 4.1), bis(2,2'-bipyridine-3$\kappa^4 N,N'$)-di-μ-fluoro-1:3κ^2F, 2:3$\kappa^2 F$ -decafluoro-1$\kappa^5 F$, 2κ^5F - ditantalum(V)copper(II) $Cu(bpy)_2(TaF_6)_2$, (compound 4.2), tris (2,2'-bipyridine) copper(II) hexafluorotantalate(V) $[Cu(bpy)_3][TaF_6]_2$, (compound 4.3) and *catena*-poly[diaqua (2,2'-bipyridine)copper(II)- μ-fluoro-tetrafluorotin-μ-fluoro] $[Cu(bpy)(H_2O)_2(SnF_6)]_n$, (compound 4.4). Compounds 4.1, 4.2, and 4.3 contain locally chiral copper coordination complexes with C_2, D_2, and D_3 symmetry, respectively. The extended structures of compounds

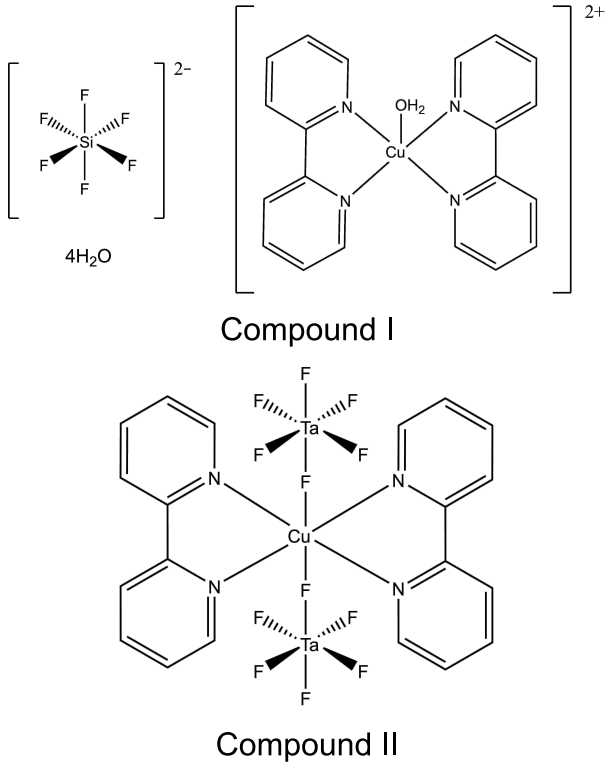

Figure 4.1. Scheme I

4.1 and 4.4 are consolidated by O—H···F and O—H···O hydrogen bonds. The structure of compound 4.3 was found to be a merohedral (racemic) twin.

4.2. Chemical Context

Copper(II) complexes of 2,2'-bipyridine (bpy) adopt a wide range of coordination geometries, including square pyramidal, trigonal bipyramidal and octahedral, depending on experimental conditions such as the ligand-to-metal ratio and pH.[111] Previous studies have shown that racemic combinations of chiral $[Cu(bpy)_2(H_2O)]^{2+}$ can crystallize in polar structures in the presence of early transition metal fluorides MF_6^{2-}, (M = Ti, Zr, Hf).[22,112]

Here, we investigate the influence of the anion on the speciation of the copper(II) complex and the arrangement of the ions in the crystal structure in a series of compounds

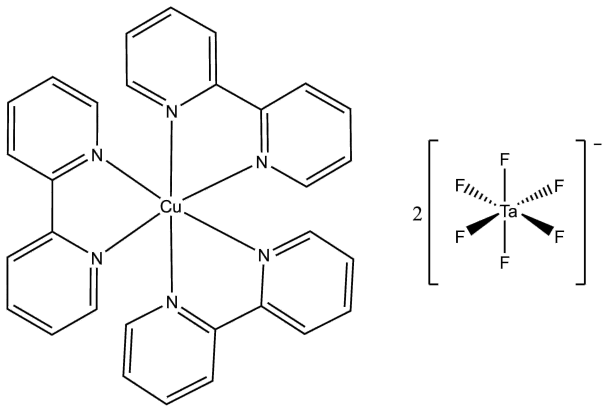

Compound III

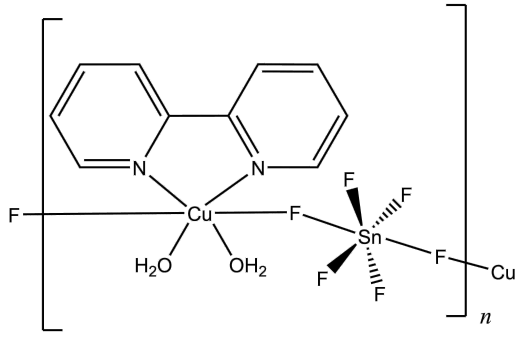

Compound IV

Figure 4.2. Scheme II

based on copper(II)–2,2'-bipyridine cations and SiF_6^{2-}, SnF_6^{2-}, and TaF_6^{-} anions. Among these hydrothermally-prepared structures we observe three distinct locally chiral copper-bipyridine complexes: C_2-symmetric cations in $[Cu(bpy)_2(H_2O)][SiF_6]\cdot 4H_2O$, (compound 4.1), D_2-symmetric $Cu(bpy)_2(TaF_6)_2$ molecules, (compound 4.2) and D_3-symmetric cations in $[Cu(bpy)_3][TaF_6]_2$, (compound 4.3). We also report the structure of a coordination polymer based on $Cu(bpy)(H_2O)_2^{2+}$ cations and SnF_6^{2-} anions, (compound 4.4), that forms under similar conditions.

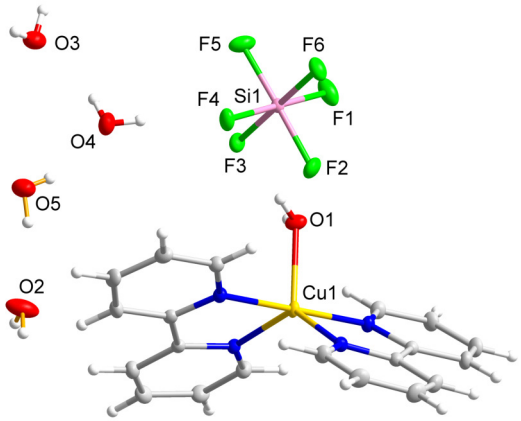

Figure 4.3. The molecular structure of compound 4.1, $[Cu(bpy)_2(H_2O)][SiF_6]\cdot 4H_2O$. Ellipsoids of non-H atoms are drawn at 50% probability. H atoms are drawn with an atomic radius of 0.135 Å.

4.3. Structural Commentary

Compound 4.1 has the formula $[Cu(bpy)_2(H_2O)][SiF_6]\cdot 4H_2O$ and crystallizes in space group $C2/c$. The structure features isolated C_2-symmetric Δ- and Λ-$[Cu(bpy)_2(H_2O)]^{2+}$ cations and octahedral SiF_6^{2-} anions (Figure 4.3). The 5-coordinate Cu^{2+} ion has a slightly distorted trigonal bipyramidal coordination environment ($\tau = 0.77$), as described by the parameter $\tau = (\beta - \alpha)/60$, where β and α are the two largest angles of the complex ($\tau = 1$ corresponds to an ideal trigonal bipyramid and $\tau = 0$ corresponds to an ideal square pyramid).[131] The average Cu—N bond length and the Cu–OH_2 bond distance in compound 4.1 are in agreement with the reported distances in other known $[Cu(bpy)_2(H_2O)]^{2+}$ complexes.[22,112,144,145]

Compound 4.2 has the formula $Cu(bpy)_2(TaF_6)_2$ and crystallizes in space group $P\bar{1}$. The structure is comprised of molecular Δ- and Λ-$Cu(bpy)_2(TaF_6)_2$ complexes with local D_2 symmetry. Each Cu(II) center is equatorially coordinated by two bpy ligands and axially coordinated by two TaF_6^- groups. Two independent $Cu(bpy)_2(TaF_6)_2$ units with the same

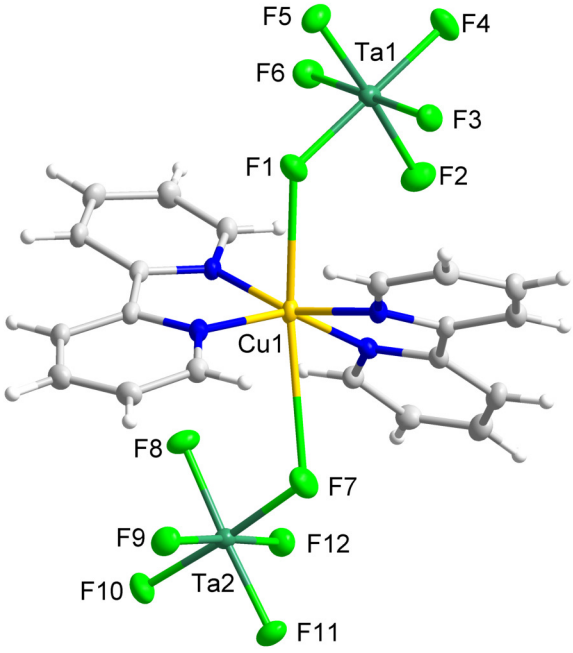

Figure 4.4. The molecular structure of compound 4.2, $Cu(bpy)_2(TaF_6)_2$. Ellipsoids of non-H atoms are drawn at 50% probability. H atoms are drawn with an atomic radius of 0.135 Å.

handedness are present within the arbitrarily chosen asymmetric unit (Figure 4.4). These complexes differ in their Cu–F bond lengths and F–Cu–F angles: Cu1–F1 = 2.537(3) Å, Cu1–F7 = 2.987(3) Å, F1–Cu1—F7 = 161.46(9)°; Cu2–F13 = 2.706(3) Å, Cu2—F19 = 2.775(3) Å, F13–Cu2–F19 = 168.21(10)°. The observed Cu–F distances fall above the upper quartile of the distribution of known Cu–F bond distances among structures in the Cambridge Structural Database (mean = 2.240 Å, standard deviation = 0.270 Å). The Cu–N and Cu–F distances in compound 4.2 are in reasonable agreement with the bond distances reported in the complex (6,6”’-dimethyl-2,2’:6’,2”:6”,2”’-quaterpyridine)-bis(tetrafluoroborate)- copper(II) (CSD refcode: UZELOC).[146]

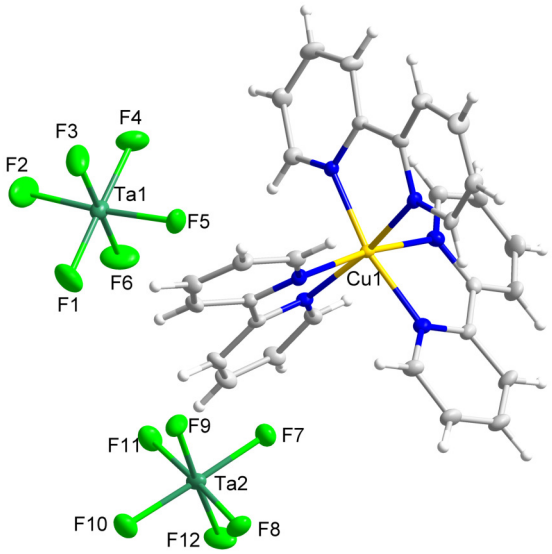

Figure 4.5. The molecular structure of compound 4.3, $[Cu(bpy)_3][TaF_6]_2$. Ellipsoids of non-H atoms are drawn at 50% probability. H atoms are drawn with an atomic radius of 0.135 Å.

Compound 4.3 has the formula $[Cu(bpy)_3][TaF_6]_2$ and crystallizes in the enantiomorphous space group $P3_2$. The structure of 4.3 contains D_3-symmetric Λ-$Cu(bpy)_3^{2+}$ cations with Cu(II) in an octahedral CuN_6 coordination environment. The Cu–N distances are in agreement with those of the $Cu(bpy)_3^{2+}$ cations in $[Cu(bpy)_3][PF_6]_2$ (CSD refcode: REZJAI) and $[Cu(bpy)_3][BF_4]_2$ (CSD refcode: RIGTEH).[147] Two distinct octahedral TaF_6^- anions are present in the asymmetric unit (Figure 4.5).

Compound 4.4 has the formula $Cu(bpy)(H_2O)SnF_6$ and crystallizes in space group $P2/n$. The structure is composed of one-dimensional coordination chains propagating in the [101] direction that can be described as alternating $Cu(bpy)(H_2O)_2^{2+}$ cations (Cu site symmetry 2) and SnF_6^{2-} anions catenated through bridging Cu–F–Sn linkages. The Sn^{4+} ion occupies a crystallographic inversion center. Intramolecular hydrogen bonding is present along the chains via O1–H1A···F2 and O1–H1B···F3 contacts (Figure 4.6; Table 4.2). The Cu–F bond

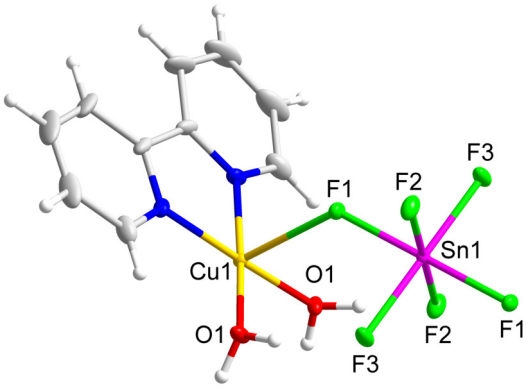

Figure 4.6. The molecular structure of compound 4.4, $[Cu(bpy)(H_2O)(SnF_6)]_n$. Ellipsoids of non-H atoms are drawn at 50% probability. H atoms are drawn with an atomic radius of 0.135 Å.

distance of 2.3830(10) Å is in agreement with those found in the reported compound Cu(4,4'-bipyridine)$_2$SiF$_6$ (CSD refcode: PETWES).[148]

4.4. Supramolecular Features

In the extended structure of 4.1, the $Cu(bpy)_2(H_2O)^{2+}$ and SiF_6^{2-} groups are linked via O—H···F hydrogen bonding between the apical water molecule and two SiF_6^{2-} ions (Table 4.1). The Δ/Λ—$Cu(bpy)_2(H_2O)^{2+}$ units participate in displaced heterochiral $\pi-\pi$ stacking interactions between the N1/C1–C5 and N2/C6–C10 rings with an interplanar angle of 1.11(11)°, centroid–centroid distance of 3.8774(12) Å, and a slippage distance of 1.490 Åto form Δup–Λdown– Δup–Λdown and Δdown–Λup–Δdown–Λup chains (up/down refers to the orientation of the Cu—O bond vector in the +a or –a direction). The water molecules of hydration are involved in O—H···F hydrogen bonding interactions with the SiF_6^{2-} anion as well as O—H···O bonds with other water molecules (Figure 4.7).

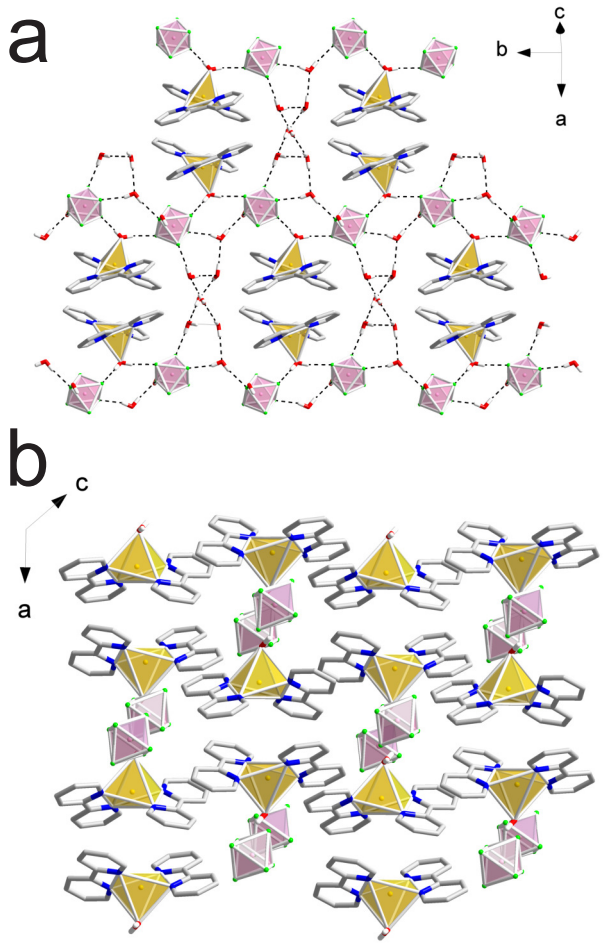

Figure 4.7. Packing diagram for compound 4.1, $[Cu(bpy)_2(H_2O)][SiF_6]\cdot 4H_2O$: yellow polyhedra represent $Cu(bpy)_2(H_2O)^{2+}$ cations and pink polyhedra represent SiF_6^{2-} anions.

The neutral $Cu(bpy)_2(TaF_6)_2$ complexes in compound 4.2 form homochiral chains in which the F—Cu—F bond axes of adjacent complexes are aligned along the a + b or b – a directions, as shown in Figure 4.8. Along the c direction, each chain is neighbored by a chain with the opposite chirality and same orientation on one side and a chain with the same chirality and opposite orientation on the other.

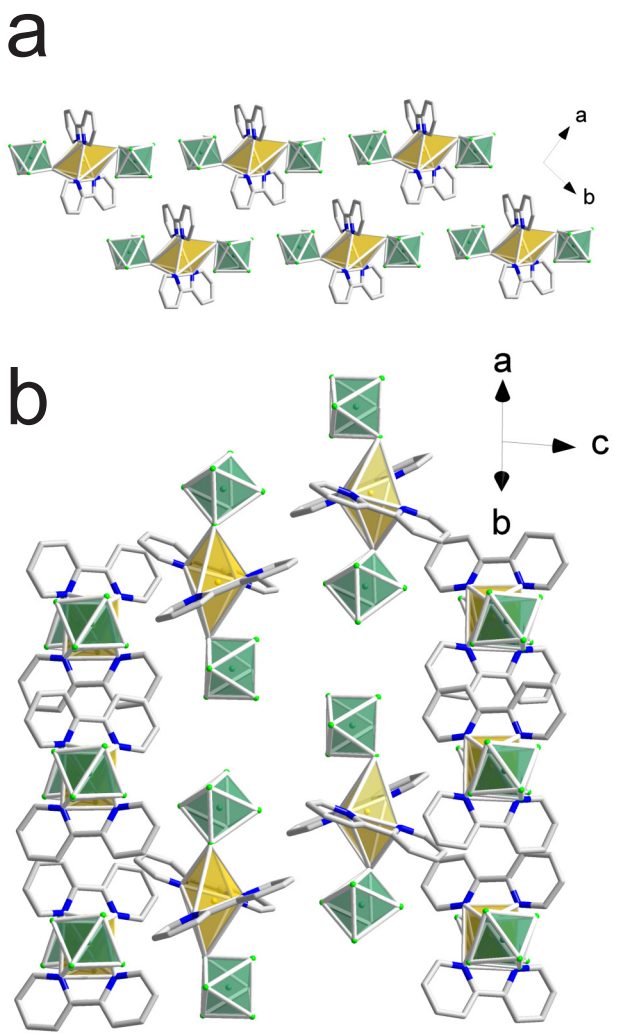

Figure 4.8. Packing diagram for compound 4.2, $Cu(bpy)_2(TaF_6)_2$: yellow polyhedra represent $Cu(bpy)_2^{2+}$ cations and green polyhedra represent TaF_6^- anions.

In compound 4.3, the Λ—$Cu(bpy)_3^{2+}$ complexes participate in displaced $\pi - \pi$ stacking interactions propagating along the 3_2 screw axes with an interplanar angle of 13.9°, centroid–centroid distance of 3.933(2) Å between adjacent N1/C1-C5 and N5/C21–C25 pyridine rings, and a horizontal shift distance of 1.970 Å. Each Λ—$Cu(bpy)_3^{2+}$ cation is surrounded by six TaF_6^- anions (Figure 4.9).

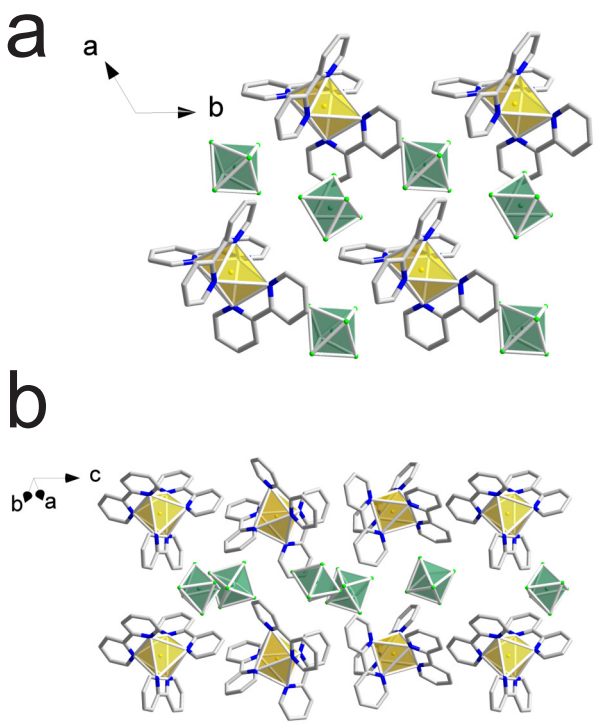

Figure 4.9. Packing diagram for compound 4.3, $[Cu(bpy)_3][TaF_6]_2$: yellow polyhedra represent $Cu(bpy)_3^{2+}$ cations and green polyhedra represent TaF_6^- anions.

The one-dimensional coordination chains in compound 4.4 pack in a brickwork arrangement via parallel displaced π–π stacking interactions (Figure 4.10). One of the stacking interactions involves parallel N1/C1–C5 pyridine rings at a centroid-centroid distance of 3.8133(12) Å and a shift distance 1.676 Å, while the other stacking interaction involves non-parallel N1/C1–C5 pyridine rings with an interplanar angle of 3.54(11)°, centroid–centroid distance of 3.5830(14) Å and a shift distance of 1.072 Å.

4.5. Database Survey

A survey of structures related to compound 4.1 reported in the Cambridge Structural Database (CSD)[142] produced five other compounds based on $[Cu(bpy)_2(H_2O)]^{2+}$ complexes

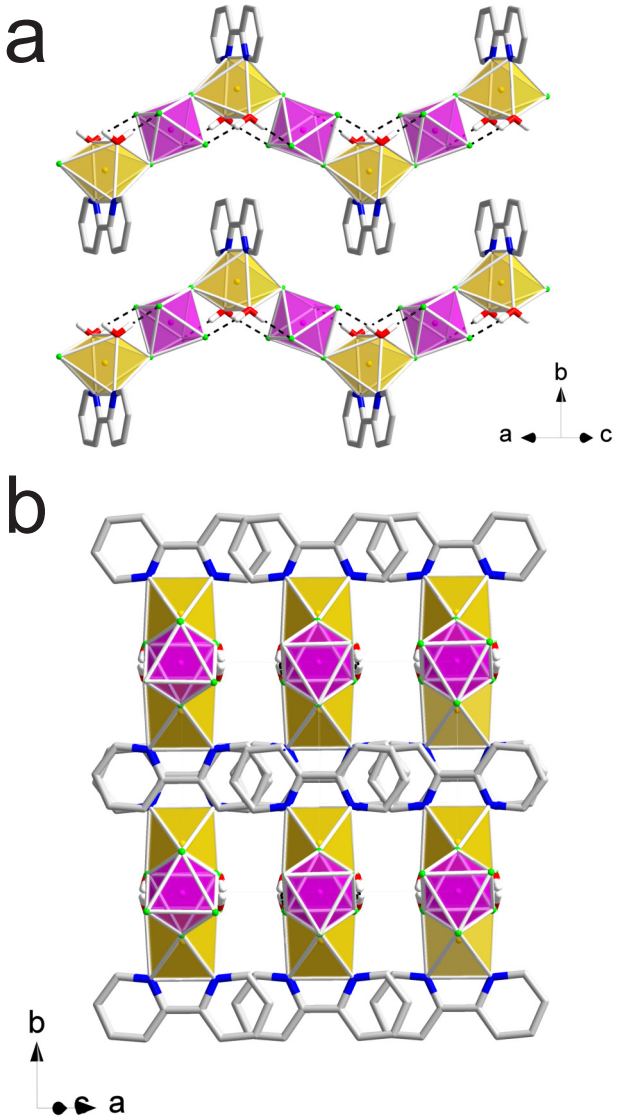

Figure 4.10. Packing diagram for compound 4.4, $[Cu(bpy)(H_2O)(SnF_6)]_n$: yellow polyhedra represent $Cu(bpy)(H_2O)_2^{2+}$ cations and magenta polyhedra represent SnF_6^{2-} anions.

and fluorinated inorganic anions: $[Cu(bpy)_2(H_2O)][BF_4]_2$ (CSD refcode: VIKDOJ),[145] $[Cu(bpy)_2(H_2O)][PF_6]_2$ (CSD refcode: EQIQOL),[144] and $[Cu(bpy)_2(H_2O)][MF_6]\cdot 3H_2O$ (M = Ti, Zr, Hf ; CSD refcodes: GESHOD, YUGYEH, YUGYIL, YUGYOR).[22,112] These compounds display a variety of packing architectures, with compounds based on singly charged

PF_6^- and BF_4^- anions displaying hydrogen-bonded clusters composed of two anions and one cation while compounds based on doubly charged MF_6^{2-} anions form extended hydrogen bonded networks. The hydrogen bonding interactions in 4.1 differ from the analogous compounds based on early transition metal fluorides in that the MF_6^{2-} anions hydrogen bonded to the $[Cu(bpy)_2(H_2O)]^{2+}$ complex are both hydrogen bonded to the same pair of $[Cu(bpy)_2)(H_2O)]^{2+}$ complexes in the ETM case whereas they are bound to two different complexes in the SiF_6^{2-} case. Further, while the $[Cu(bpy)_2(H_2O)][MF_6]\cdot 3H_2O$ (M = Ti, Zr, Hf) compounds display both face-to-face and displaced $\pi - \pi$ stacking interactions, 4.1 has only displaced stacking interactions.

A search of the CSD for structures related to 4.2 revealed no other known octahedral bis(2,2'-bipyridine)copper(II) complexes with two fluorinated anions coordinated in the apical positions. The most similar example known to the authors is (6,6"'-dimethyl-2,2':6',2":6",2"'-quaterpyridine)-bis(tetrafluoroborate)-copper(II) (CSD refcode: UZELOC).[146] This structure features copper(II) complexes arranged such that the F—Cu—F axis of each complex is oriented along the a direction. Additionally, these complexes participate in heterochiral $\pi - \pi$ stacking interactions.

Compound 4.3 is a new member of the family of compounds that includes $[A(bpy)_3][PF_6]_2$ (A = Mn, Co, Ni, Cu, Zn, Ru, and Cd) (CSD refcodes: YEGLUR, VUMTEE, WOTSAZ01, REZJAI, WOTSON, BPYRUG, XEFNOM, respectively),[132,149–151] $Zn(bpy)_3][TaF_6]_2$ (CSD refcode: HAHFII), and $[Zn(bpy)_3][NbF_6]_2$ (CSD refcodes: HAHFUU).[147] These compounds include either Δ- or Λ—$Cu(bpy)_3^{2+}$ cations arranged along 3_1 or 3_2 screw axes depending on the handedness of the $Cu(bpy)_3^{2+}$ complexes.

Compound 4.4 is isostructural to the coordination polymer Cu(bpy)(H_2O)HfF_6 (CSD refcode: YUGXOQ).[112] These compounds share identical connectivity with a series of coordination polymers with the formula M'(bpy)(H_2O)$_2MO_xF_{6-x}$ compounds (M'/M = Cu/Ti, Cu/V, Cu/Nb, Cu/Mo, Zn/Mo, and Zn/W), which display polar zigzag chains.[67]

4.6. Synthesis and Crystallization

The compounds reported here were synthesized by the hydrothermal pouch method.[69] In each reaction, reagents were heat sealed in Teflon pouches. Groups of six pouches were then placed into a 125 mL Parr autoclave with 40 mL distilled water as backfill. The autoclave was heated at a rate of 5 °C min^{-1} to 150 °C and held at 150 °C for 24 h. The autoclaves were allowed to cool to room temperature at a rate of 6 °C h^{-1} and the solid products were recovered by vacuum filtration. Compound 4.1 was synthesized in a pouch containing 1.9 mmol of $Cu(NO_3)_2{\cdot}H_2O$, 5 mmol of 2,2'-bipyridine, 1.5 mmol $(NH_4)_2SiF_6$ and 1 mL deionized H_2O. Compound 4.2 was synthesized in a pouch containing 1.7 mmol of CuO, 2.5 mmol of 2,2'-bipyridine, 0.85 mmol Ta_2O_5, 0.8 mL HF(aq),and 0.3 mL deionized H_2O. Compound 4.3 was synthesized in a pouch containing 1.7 mmol of CuO, 5.1 mmol of 2,2'-bipyridine, 0.85 mmol Ta_2O_5, 1 mL HF(aq) and 0.1 ml deionized H_2O. Compound 4.4 was synthesized in a pouch containing 1.9 mmol of $Cu(NO_3)_2{\cdot}H_2O$, 1.3 mmol of 2,2'-bipyridine, 1.7 mmol $(NH_4)_2SnF_6$ and 1 mL deionized H_2O.

4.7. Refinement

Hydrogen atom positions were assigned from difference map peaks and their positions freely refined with the exception of C—H hydrogen atoms of 2,2'-bipyridine, which were constrained to ride at distances of 0.95 Å from the associated C atoms with U_{iso}(H) =

Table 4.1. Hydrogen bonding interactions for compound 4.1.

D	H	A	d(D-H)/Å	d(H-A)/Å	d(D-A)/Å	D-H-A/°
O(1)	H(1A)	F(3)	0.76(3)	1.91(3)	2.6616(14)	177(3)
O(1)	H(1B)	$F(6)^{i}$	0.78(2)	1.93(2)	2.7053(14)	170(2)
O(2)	H(2A)	F(1)	0.75(2)	1.94(2)	2.6677(17)	164(2)
O(2)	H(2B)	$F(4)^{i}$	0.79(3)	2.00(3)	2.7807(17)	167(2)
O(3)	H(3A)	$F(5)^{ii}$	0.77(3)	1.99(3)	2.7607(18)	177(3)
O(3)	H(3B)	$O(5)^{iii}$	0.73(3)	2.06(3)	2.779(2)	171(3)
O(4)	H(4A)	O(3)	0.72(2)	2.05(2)	2.749(2)	162(2)
O(4)	H(4B)	F(4)	0.77(3)	1.98(3)	2.7462(16)	170(2)
O(5)	H(5A)	O(4)	0.69(2)	2.13(2)	2.779(2)	158(2)
O(5)	H(5B)	$O(2)^{iv}$	0.81(3)	1.99(3)	2.786(2)	169(2)

(i)1/2-X,1/2+Y,1/2-Z;(ii)1/2-X,1/2-Y,1-Z;
(iii)1-X,+Y,3/2-Z;(iv)1/2+X,1/2-Y,1/2+Z

Table 4.2. Hydrogen bonding interactions for compound 4.4.

D	H	A	d(D-H)/Å	d(H-A)/Å	d(D-A)/Å	D-H-A/°
O(1)	H(1A)	$F(2)^{i}$	0.88(3)	1.79(3)	2.6444(17)	165(3)
O(1)	H(1B)	$F(3)^{ii}$	0.81(3)	1.84(4)	2.6293(17)	164(4)

(i)-1/2+X,2-Y,1/2+Z;(ii)1-X,2-Y,1-Z

$1.2U_{eq}$(C). The measured crystal of compound 4.3 is a class II twin by merohedry about a twofold axis along the [110] direction to give apparent Laue symmetry of $3m1$. The twinning occurs with a BASF of 0.5, suggesting that both the $P3_1$ and $P3_2$ configurations are present in equal proportions within the sample.

CHAPTER 5

Hydrothermal Synthesis and Crystal Structures of $[Cu(phen)(H_2O)_3(MF_6)]\cdot H_2O$ (M = Ti, Zr, Hf) and $[Cu(phen)(H_2O)_2F]_2[HfF_6]\cdot H_2O$

This chapter was adapted with permission from:

Nisbet, M. L.; Poeppelmeier, K. R. Crystal Structures of $[Cu(Phen)(H_2O)_3(MF_6)]\cdot H_2O$ (M = Ti, Zr, Hf) and $[Cu(Phen)(H_2O)_2F]_2[HfF_6]\cdot H_2O$. *Acta Crystallogr., Sect. E: Crystallogr. Commun.* **2021**, 77 (2), 165–170. https://doi.org/10.1107/S2056989021000645.

5.1. Abstract

The crystal structures of three bridged bimetallic molecular compounds, triaqua-2κO-μ-fluoro-pentafluoro-1κF-(1,10- phenanthroline-2κ^2N,N')-titanium(IV)copper(II) monohydrate $[Cu(phen)(H_2O)_3(TiF_6)]\cdot H_2O$, triaqua-2$\kappa$O-$\mu$-fluoro-pentafluoro-1$\kappa$F-(1,10- phenanthroline-2κ^2N,N')-zirconium(IV)copper(II) monohydrate $[Cu(phen)\ (H_2O)_3(ZrF_6)]\cdot H_2O$, and triaqua-2$\kappa$O-$\mu$-fluoro-pentafluoro-1$\kappa$F-(1,10- phenanthroline-2κ^2N,N')-hafnium(IV)copper(II) monohydrate $[Cu(phen)(H_2O)_3(HfF_6)]\cdot H_2O$, and one molecular salt diquafluoro(1,10-phenanthroline)copper(II) hexafluorohafnate(IV) monohydrate $[Cu(phen)(H_2O)_2F]_2[HfF_6]\cdot H_2O$ are reported. The bridged bimetallic compounds adopt Λ-shaped configurations, with the octahedrally coordinated copper(II) center linked to the fluorinated early transition metal via a fluoride linkage. The extended structures of these Λ-shaped compounds are organized through both intra- and intermolecular hydrogen bonds and

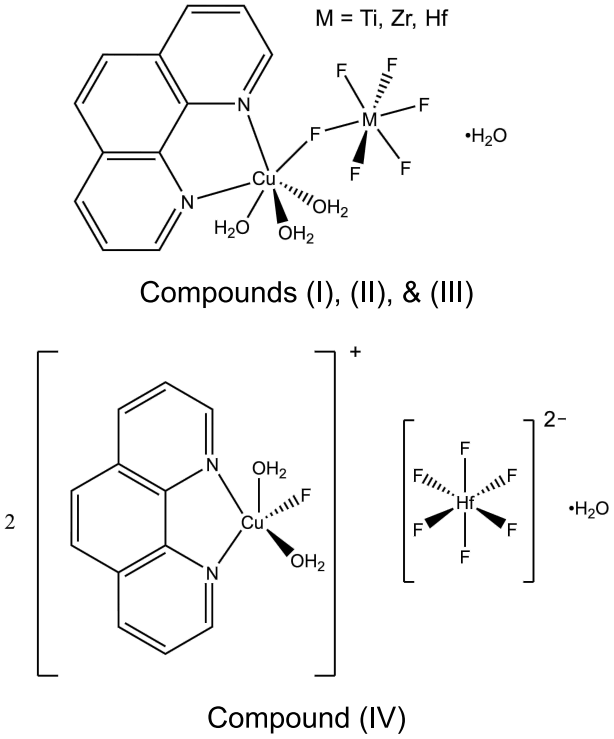

Figure 5.1. Scheme

intermolecular $\pi - \pi$ stacking. The salt compound $[Cu(phen)(H_2O)_2F]_2[HfF_6]\cdot H_2O$ displays an isolated square pyramidal $Cu(phen)(H_2O)_2F^+$ complex linked to other cationic complexes and isolated HfF_6^{2-} anions through intermolecular hydrogen bonding interactions.

5.2. Chemical Context

Lambda (Λ)-shaped molecules have been demonstrated as efficient building blocks in the synthesis of noncentrosymmetric (NCS) materials via arrangement into head-to-tail and accordion (head-to-head, tail-to-tail) structures.[152–156] Although this concept was first applied to organic Λ-shaped molecules in crystalline materials and polymers, recently NCS compounds based on inorganic bimetallic Λ-shapes have been reported, namely $K_{10}(Mo_2O_4F_7)_3X$ (X = Cl, $([Br_3][Br])_{1/2}$, $([I_3][I])_{1/2}$), $K_{10}(Nb_2O_2F_9)_3X$ (X = Br, $([Br_3][Br])_{1/2}$, $([I_3][I])_{1/2}$), and

$[Cu(H_2O)_5(VOF_4(H_2O))]\cdot H_2O$.[143,157] Here, we report the structures of three centrosymmetric compounds based on inorganic bimetallic Λ-shapes with the formula $[Cu(phen)(H_2O)_3(MF_6)]\cdot H_2O$ (M = Ti, Zr, Hf; phen = 1,10-phenanthroline). Although these compounds crystallize with inversion symmetry, the novel molecular building units are potential targets of future studies aimed to perturb their packing arrangement to form NCS structures. The salt compound $[Cu(phen)(H_2O)_2F]_2[HfF_6]\cdot H_2O$ provides a point of comparison as an unbridged analogue of $[Cu(phen)(H_2O)_3(HfF_6)]\cdot H_2O$.

5.3. Structural Commentary

Compound 5.1 has the formula $[Cu(phen)(H_2O)_3(TiF_6)]\cdot H_2O$ and crystallizes in the orthorhombic space group *Pbca* (Figure 5.2). The structure of compound 5.1 features Cu1 in a tetragonally distorted octahedral environment with elongated axial Cu1-F1 (2.3643(12) Å) and Cu1-O1 (2.2794(17) Å) bonds owing to the Jahn-Teller effect of copper(II). The Cu1 center is linked to the TiF_6^{2-} anion through the bridging F1 ligand. The octahedral coordination environment of Ti1 is slightly distorted, with Ti1-F bond lengths ranging from 1.8395(13) Å to 1.9035(3) Å. The Λ-shape, indicated by the Cu1-F1-Ti1 bond angle of 134.93(6)°, is enforced by the two intramolecular O2-H2B···F5 and O3-H3B···F6 hydrogen bonds (Table 5.1).

Compound 5.2 has the formula $[Cu(phen)(H_2O)_3(ZrF_6)]\cdot H_2O$ and crystallizes in the monoclinic space group $P2_1/n$ (Figure 5.3). The structure of compound 5.2 features Cu1 in a tetragonally distorted octahedral environment with elongated axial Cu1-F1 (2.5184(6) Å) and Cu-O1 (2.2758(7) Å) bonds owing to the Jahn-Teller effect of copper(II). The Cu1 center is linked to the ZrF_6^{2-} anion through the bridging F1 ligand. The octahedral coordination environment of Zr1 is slightly distorted, with Zr1-F bond lengths ranging from 1.9910(6) Å to

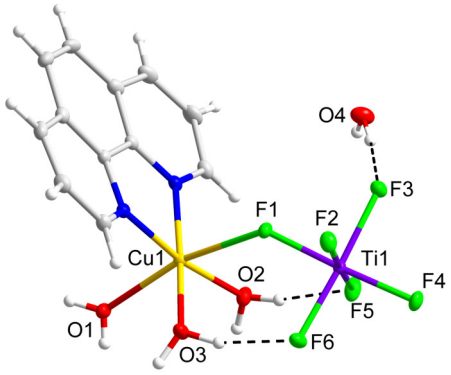

Figure 5.2. Molecular structure of compound 5.1, $[Cu(phen)(H_2O)_3(TiF_6)]\cdot H_2O$. Ellipsoids of non–H atoms are drawn at 50% probability. H atoms are drawn with an atomic radius of 0.135 Å

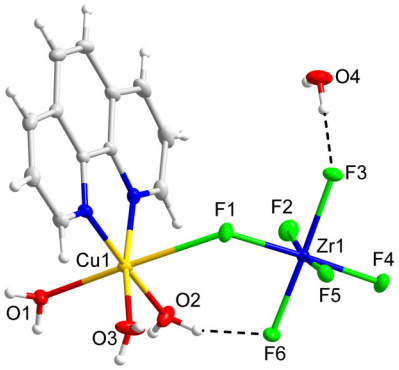

Figure 5.3. Molecular structure of compound 5.2, $[Cu(phen)(H_2O)_3(ZrF_6)]\cdot H_2O$. Ellipsoids of non–H atoms are drawn at 50% probability. H atoms are drawn with an atomic radius of 0.135 Å

2.0430(6) Å. TheΛ-shape, indicated by the Cu1-F1-Zr1 bond angle of 132.59(3)°, is enforced by an intramolecular O2-H2B···F6 hydrogen bond (Table 5.2). The single intramolecular hydrogen bond in compound 5.2 tilts the ZrF_6^{2-}- group significantly relative to the TiF_6^{2-} group in compound 5.1, which is depicted in Figure 5.6 and reflected in the F1-Cu1-N1 bond angle of 77.75(3)°angle in compound 5.2 compared to 89.45(6)°in compound 5.1.

Compound 5.3 has the formula $[Cu(phen)(H_2O)_3(HfF_6)]\cdot H_2O$ crystallizes in the monoclinic space group $P2_1/n$ (Figure 5.4). Compound 5.3 is isostructural to compound 5.2.

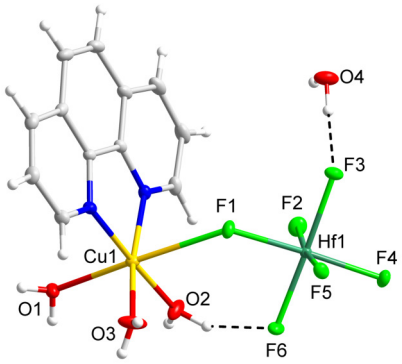

Figure 5.4. Molecular structure of compound 5.3, $[Cu(phen)(H_2O)_3(HfF_6)]\cdot H_2O$. Ellipsoids of non–H atoms are drawn at 50% probability. H atoms are drawn with an atomic radius of 0.135 Å

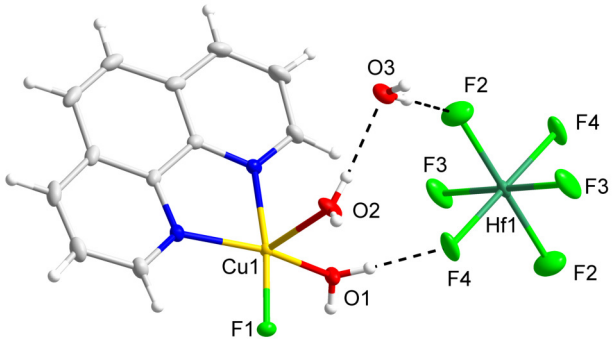

Figure 5.5. Molecular structure of compound 5.4, $[Cu(phen)(H_2O)_2F]_2[HfF_6]\cdot H_2O$. Ellipsoids of non–H atoms are drawn at 50% probability. H atoms are drawn with an atomic radius of 0.135 Å

Compound 5.4 has the formula $[Cu(phen)(H_2O)_2F]_2[HfF_6]\cdot H_2O$ crystallizes in the monoclinic space group $P2_1/n$ (Figure 5.5). The structure of compound 5.4 features isolated square pyramidal $Cu(phen)(H_2O)_2F^+$ cations and octahedral HfF_6^{2-} anions. The free HfF_6^{2-} octahedron occupies an inversion center with three distinct bond lengths ranging between 1.9863(10) Å and 1.9957(9) Å.

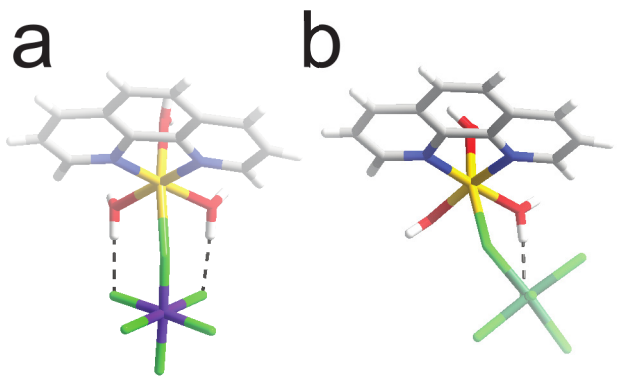

Figure 5.6. Comparison of the molecular structures of (a) compound 5.1 and (b) compound 5.3.

5.4. Supramolecular Features

The Λ-shaped building units in compounds 5.1-5.3 are arranged in head-to-tail chains via intermolecular hydrogen bonding with multiple hydrogen bonding and $\pi - \pi$ stacking contacts to adjacent chains.

Each [Cu(phen)$(H_2O)_3(TiF_6)$] complex in compound 5.1 participates in hydrogen bonding with four other [Cu(phen)$(H_2O)_3(TiF_6)$] complexes and three free water molecules (Figure5.7, Table 5.1). The complexes pack with both face-to-face and displaced $\pi - \pi$ stacking interactions (Table 5.5).

The [Cu(phen)$(H_2O)_3(MF_6)$] (M = Zr, Hf) units in compound 5.2 and compound 5.3 are involved in five hydrogen bonding contacts to adjacent [Cu(phen)$(H_2O)_3(MF_6)$] complexes and three contacts to hydrating water molecules (Figure 5.8, Table 5.2 , and Table 5.3). The [Cu(phen)$(H_2O)_3(MF_6)$] complexes participate in parallel displaced $\pi - \pi$ stacking interactions (Table 5.5).

In compound 5.4, each fluoride ligand forms two hydrogen bonds with the water ligands of adjacent Cu(phen)$(H_2O)_2F^+$ complexes (Figure 5.9). The equatorial water ligands

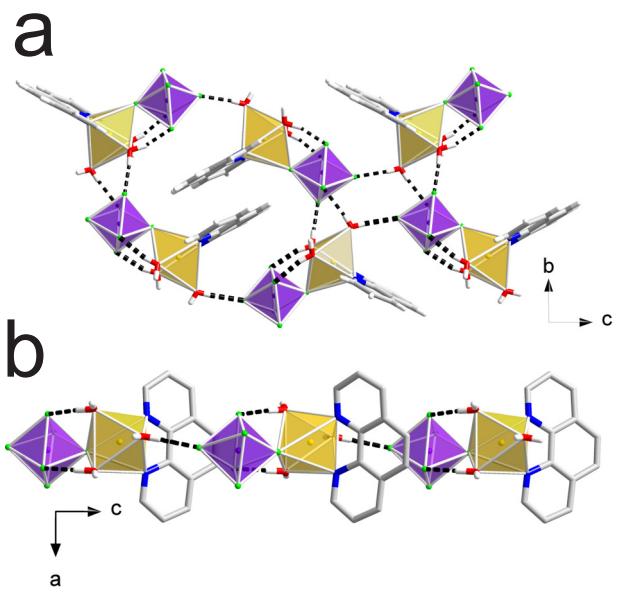

Figure 5.7. Packing diagram for compound 5.1, $[Cu(phen)(H_2O)_3(TiF_6)]\cdot H_2O$: yellow polyhedra represent $Cu(phen)(H_2O)_3^{2+}$ cations and purple polyhedra represent TiF_6^{2-} anions.

form O1-H1A···F1 hydrogen bonds with adjacent $Cu(phen)(H_2O)_2F^+$ complexes and O1-H1B···F4 hydrogen bonds with HfF_6^{2-} groups (Table 5.4). The apical water molecule forms an O2-H2B···F1 hydrogen bond to an adjacent $Cu(phen)(H_2O)_2F^+$ complex and a O2-H2A···O3 hydrogen bond with free water molecule (Table 5.4). Each MF_6^{2-} group forms hydrogen bonds with four free water molecules and two $Cu(phen)(H_2O)_2F^+$ complexes. The $Cu(phen)(H_2O)_2F^+$ complexes pack with both face-to-face and parallel displaced $\pi-\pi$ stacking interactions (Table 5.5).

5.5. Database Survey

Aside from compounds 5.1, 5.2, and 5.3, the compound $Cu(H_2O)_5(VO(H_2O)F_4)]\cdot H_2O$ is the only example of a molecular inorganic Λ-shape known to the authors.[143]

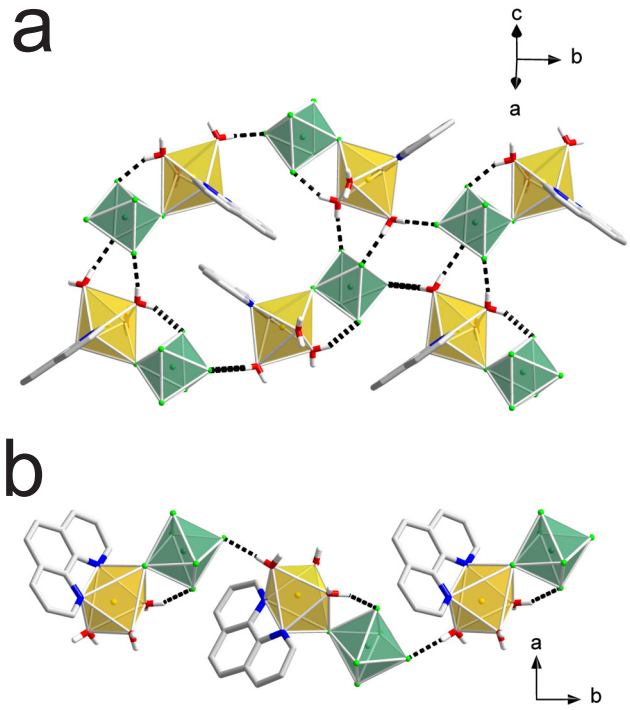

Figure 5.8. Packing diagram for compound 5.2, $[Cu(phen)(H_2O)_3(ZrF_6)]\cdot H_2O$ and compound 5.3, $[Cu(phen)(H_2O)_3(HfF_6)]\cdot H_2O$: yellow polyhedra represent $Cu(phen)(H_2O)_3^{2+}$ cations and green polyhedra represent HfF_6^{2-} anions.

$[Cu(H_2O)_5(VOF_4(H_2O))]\cdot H_2O$ contains a molecular Λ-shaped $[Cu(H_2O)_5(VOF_4(H_2O))]$ molecule that is bridged via the Cu1-O8-V1 linkage with a bond angle of 142.88°. The Λ-shape of this complex is supported by a single intramolecular hydrogen bond as well as two hydrogen bonding interactions with a free water molecule that serves as an intermolecular "bridging molecule." In contrast, the hydrating water molecules in compounds 5.1, 5.2, and 5.3 bridge between adjacent complexes rather than the same complex. The smallest O8-Cu-O bond angle in $[Cu(H_2O)_5(VOF_4(H_2O))]\cdot H_2O$ is 88.42°, meaning that the complex has a small tilt similar to compound 5.1.

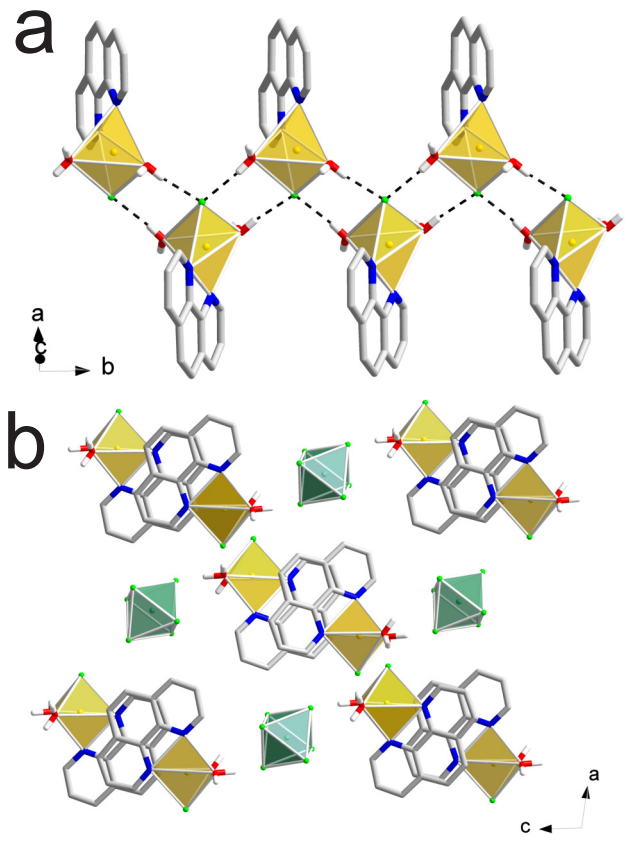

Figure 5.9. Packing diagram for compound 5.4, $[Cu(phen)(H_2O)_2F]_2[HfF_6]\cdot H_2O$: yellow polyhedra represent $Cu(phen)(H_2O)_2F^+$ cations and green polyhedra represent HfF_6^{2-} anions.

The Λ-shapes in $[Cu(H_2O)_5(VO(H_2O)F_4)]\cdot H_2O$ are arranged in a polar NCS lattice containing head-to-head/tail-to-tail chains in which the polar moments of the Λ-shaped complexes are partially aligned perpendicular to the chain direction, with head-to-tail orientations between chains. In contrast, the Λ-shapes found in compounds 5.1, 5.2, and 5.3 are arranged in nonpolar head-to-tail chains in which the polar moments of the Λ-shaped complexes are arranged in an antiparallel fashion within the chain, with a head-to-tail arrangement between chains.

5.6. Synthesis and Crystallization

The compounds reported here were synthetized by the hydrothermal pouch method.[69] In each reaction, reagents were heat sealed in Teflon pouches. Groups of six pouches were then placed into a 125 mL Parr autoclave with 40 mL distilled water as backfill. The autoclave was heated at a rate of 5 K/min to 423 K and held at 423 K for 24 h. The autoclaves were allowed to cool to room temperature at a rate of 6 K/h. Solid products were recovered by vacuum filtration. Compound 5.1 was synthesized in a pouch containing 1.69 mmol CuO, 1.69 mmol TiO_2, 2.56 mmol 1,10-phenanthroline, 1.0 mL (27.6 mmol) HF(aq) (48%), and 0.1 mL (5.5 mmol) deionized H_2O. Compound 5.2 was synthesized in a pouch containing 1.69 mmol CuO, 1.69 mmol ZrO_2, 2.56 mmol 1,10-phenanthroline, 1.0 mL (27.6 mmol) HF(aq) (48%), and 0.1 mL (5.5 mmol) deionized H_2O. Compound 5.3 was synthesized in a pouch containing 1.69 mmol CuO, 1.69 mmol HfO_2, 2.56 mmol 1,10-phenanthroline, 1.0 mL (27.6 mmol) HF(aq) (48%), and 0.1 mL (5.5 mmol) deionized H_2O. Compound 5.4 was synthesized in a pouch containing 1.69 mmol CuO, 1.69 mmol HfO_2, 2.56 mmol 1,10-phenanthroline, 0.4 mL (11.03 mmol) HF(aq) (48%), and 0.7 mL (38.85 mmol) deionized H_2O.

5.7. Refinement

Non-hydrogen atoms were refined with anisotropic displacement parameters. Hydrogen atom positions were assigned from difference map peaks with the exception of C-H hydrogen atoms of 1,10-phenanthroline, which were constrained to ride at distances of 0.95 Å from the associated C atoms with $U_{iso}(H) = 1.2\ U_{eq}(C)$ within Olex2.[96]

Table 5.1. Hydrogen bonding interactions for compound 5.1

D	H	A	d(D-H)/Å	d(H-A)/Å	d(D-A)/Å	D-H-A/°
O(2)	H(2A)	O(4)	0.83(3)	1.83(3)	2.654(2)	175(3)
O(2)	H(2B)	F(5)	0.83(4)	1.85(4)	2.666(2)	167(3)
O(3)	H(3A)	$F(3)^{i}$	0.83(4)	1.86(4)	2.683(2)	172(4)
O(3)	H(3B)	F(6)	0.91(4)	1.80(4)	2.683(2)	162(3)
O(4)	H(4A)	$F(3)^{ii}$	0.74(4)	2.00(4)	2.718(2)	163(4)
O(4)	H(4B)	$F(2)^{i}$	0.77(3)	1.97(3)	2.691(2)	156(3)
O(1)	H(1A)	$F(4)^{iii}$	0.79(4)	1.94(4)	2.726(2)	174(3)
O(1)	H(1B)	$F(2)^{i}$	0.71(4)	2.07(4)	2.775(2)	177(4)

(i)1-X,1/2+Y,1/2-Z;(ii)3/2-X,1/2+Y,+Z;
(iii)+X,3/2-Y,1/2+Z

Table 5.2. Hydrogen bonding interactions for compound 5.2

D	H	A	d(D-H)/Å	d(H-A)/Å	d(D-A)/Å	D-H-A/°
O(1)	H(1A)	$F(5)^{i}$	0.794(18)	1.943(18)	2.7338(9)	173.4(18)
O(1)	H(1B)	$F(4)^{ii}$	0.78(2)	1.93(2)	2.7147(10)	179(2)
O(2)	H(2A)	$F(3)^{i}$	0.79(2)	1.85(2)	2.6324(9)	171(2)
O(2)	H(2B)	F(6)	0.82(2)	1.87(2)	2.6491(10)	159.2(19)
O(3)	H(3A)	$F(2)^{iii}$	0.79(2)	1.84(2)	2.6327(10)	177.5(19)
O(3)	H(3B)	O(4)	0.79(2)	1.87(2)	2.6481(12)	170(2)
O(4)	H(4A)	$F(3)^{iv}$	0.799(19)	2.001(19)	2.7691(10)	160.9(18)
O(4)	H(4B)	$F(5)^{i}$	0.78(2)	2.02(2)	2.7449(11)	155(2)

(i)-1/2+X,1/2-Y,1/2+Z;(ii)1/2-X,1/2+Y,1/2-Z;
(iii)-1/2+X,1/2-Y,-1/2+Z;(iv)-1+X,+Y,+Z

Table 5.3. Hydrogen bonding interactions for compound 5.3

D	H	A	d(D-H)/Å	d(H-A)/Å	d(D-A)/Å	D-H-A/°
O(1)	H(1A)	$F(5)^{i}$	0.80(3)	1.95(3)	2.7360(13)	172(3)
O(1)	H(1B)	$F(4)^{ii}$	0.77(3)	1.95(3)	2.7136(13)	176(3)
O(2)	H(2A)	F(6)	0.86(3)	1.84(3)	2.6456(14)	154(3)
O(2)	H(2B)	$F(3)^{i}$	0.78(3)	1.87(3)	2.6361(14)	171(3)
O(3)	H(3A)	$O(4)^{iii}$	0.80(3)	1.86(3)	2.6530(17)	174(3)
O(3)	H(3B)	$F(2)^{iv}$	0.77(3)	1.86(3)	2.6331(15)	176(3)
O(4)	H(4A)	$F(5)^{v}$	0.81(3)	1.99(3)	2.7428(15)	154(3)
O(4)	H(4B)	F(3)	0.81(3)	2.00(3)	2.7703(14)	157(3)

(i)1/2+X,3/2-Y,-1/2+Z;(ii)3/2-X,-1/2+Y,1/2-Z;
(iii)1+X,+Y,+Z;(iv)1/2+X,3/2-Y,1/2+Z;(v)-1/2+X,3/2-Y,-1/2+Z

Table 5.4. Hydrogen bonding interactions for compound 5.4

D	H	A	d(D-H)/Å	d(H-A)/Å	d(D-A)/Å	D-H-A/°
O(1)	H(1A)	F(4)	0.81(3)	1.78(3)	2.5926(14)	176(3)
O(1)	H(1B)	$F(1)^{i}$	0.74(3)	1.85(3)	2.5861(13)	172(3)
O(2)	H(2A)	O(3)	0.74(3)	1.95(3)	2.6906(15)	176(3)
O(2)	H(2B)	$F(1)^{ii}$	0.80(3)	1.83(3)	2.6255(14)	175(2)
O(3)	H(3A)	F(2)	0.78(3)	1.94(3)	2.7270(17)	176(3)
O(3)	H(3B)	$F(3)^{iii}$	0.75(3)	1.96(3)	2.7020(15)	173(3)

(i)3/2-X,-1/2+Y,3/2-Z;(ii)3/2-X,1/2+Y,3/2-Z;(iii)1-X,2-Y,2-Z

Table 5.5. $\pi - \pi$ stacking interactions in compounds 5.1-5.4

Compound #	Stacking Type	d_{ph-py} (Å)	d_{py-py} (Å)	d_{ph-ph} (Å)	Interplanar Angle (°)
5.1	face-to-face	3.699	4.162	3.583	0
5.1	parallel displaced	6.042	4.128	8.111	8.68
5.2/5.3	parallel displaced	4.469	3.407	6.324	0
5.2/5.3	parallel displaced	3.51	4.472	4.035	0
5.4	face-to-face	3.664	3.48	4.07	0
5.4	parallel displaced	3.508	3.881	4.604	0

CHAPTER 6

Toward a Systematic Study of Local Structure in Early Transition Metal Oxide-Fluorides Using Nuclear Magnetic Resonance and Extended X-ray Absorption Fine Structure

6.1. Introduction

In this chapter, the syntheses and structures of ten compounds containing ETM fluorides and oxide-fluorides are reported. These materials were synthesized for use in a systematic study of local structure dynamics in ETM fluorides and oxide-fluorides using nuclear magnetic resonance (NMR) spectroscopy and extended X-ray absorption fine structure (EXAFS). Preliminary studies of local structure in ETM-centered anions with ^{19}F NMR spectroscopy in the M-NCS series (Chapter 2) lead us to question our understanding of the microscopic behavior of ETM ions in these anions. In homoleptic environments, like that of Ti in $BaTiO_3$, the ETM ion has been observed to adopt a locally rhombohedral distortion, with the long range ordering of these distortions changing as a function of temperature while the direction and magnitude of local distortions remains relatively constant.[52] This microscopic picture is not compatible with the current understanding of ETM oxide-fluorides, which are thought to adopt statically ordered configurations with reduced symmetry based on non-equivalent M-O and M-F bonds.[56] Experimental testing is required to determine if out-of-center distortions in ETM oxide-fluorides are qualitatively distinct from out-of-center structural distortions in homoleptic ETM complexes.

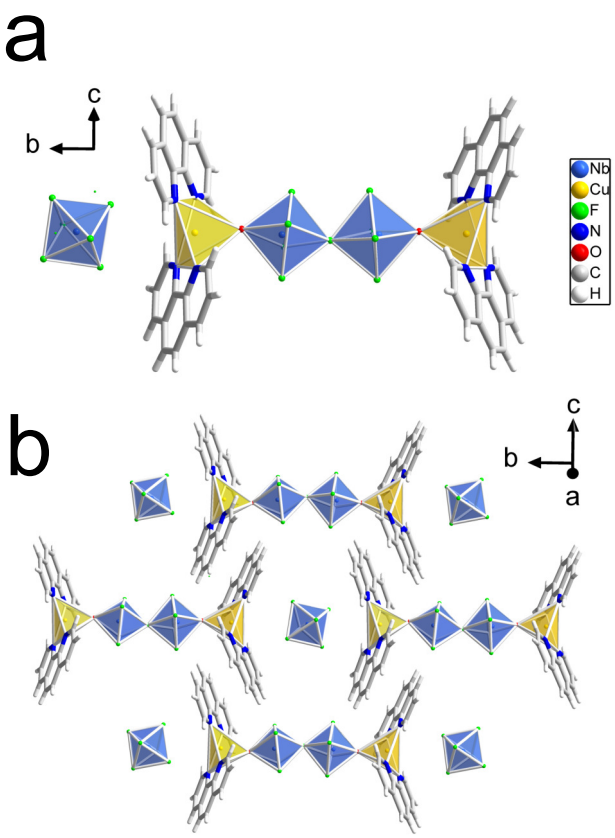

Figure 6.1. (a) Molecular structure of compounds 6.1 and 6.2, $[M(phen)_2(Nb_2O_2F_9)][NbF_6]$ (M = Cu, Zn). (b) Packing diagram of compounds 6.1 and 6.2.

6.2. Structure Descriptions

Compounds 6.1 and 6.2 are isostructural compounds with the formula $[M(phen)_2(Nb_2O_2F_9)][NbF_6]$ (M = Cu, Zn) and crystallize in the space group $P2_1/n$. The structure of these compounds features barbell-like $[M(phen)_2(Nb_2O_2F_9)]^+$ complexes arranged in alternating fashion with free $[NbF_6]^-$ anions along b (Figure 6.1). The structures of compounds 6.1 and 6.2 display heteroleptic $[NbOF_5]^{2-}$ units and a homoleptic $[NbF_6]^-$ complex. Crystallographic data for these compounds can be found in Table 6.1. The structure of compound 6.1 has been reported previously.[158]

Compound 6.3 has the formula $[Cu(phen)_2WO_2F_4]\cdot 3H_2O$ and crystallizes in the space group $P2_1/n$. The structure is composed of neutral chiral $[Cu(phen)_2WO_2F_4]$ complexes that participate in both face-to-face and parallel displaced $\pi - \pi$ stacking interactions to form a zigzag stacking pattern (Figure 6.2).[159] Crystallographic data for compound 6.3 is given in Table 6.2.

Compound 6.4 has the formula $[Zn(phen)_2(H_2O)_2][WO_2F_4]$ and crystallizes in the space group $P\bar{1}$. The structure contains molecular $[Zn(phen)_2(H_2O)_2]^{2+}$ cations and $[WO_2F_4]^{2-}$ anions (Figure 6.3). Chiral $[Zn(phen)_2(H_2O)_2]^{2+}$ complexes participate in face-to-face $\pi - \pi$ stacking interactions as well as hydrogen bonding with the $[WO_2F_4]^{2-}$ anions. Crystallographic data for compound 6.4 is given in Table 6.2.

Compound 6.5 has the formula $[Cu(phen)(H_2O)_3(MoO_2F_4)]\cdot H_2O$ and crystallizes in the space group $P\bar{1}$. The structure of 6.5 contains neutral Λ-shaped $Cu(phen)(H_2O)_3(MoO_2F_4)$ complexes that form hydrogen bonded chains with other Λ-shaped complexes and free water molecules (Figure 6.4).[160] Crystallographic data for compound 6.5 is given in Table 6.3.

Compound 6.6 has the formula $[Zn(phen)(H_2O)_4][MoO_2F_4]$ and crystallizes in the space group $P2_1/c$. The structure of 6.6 is composed of $[Zn(phen)(H_2O)_4]^{2+}$ cations and $[MoO_2F_4]^{2-}$ anions which participate in hydrogen bonding to form chains (Figure 6.5). Crystallographic data for compound 6.6 is given in Table 6.3.

Compounds 6.7 and 6.8 have the formula $M(phen)_2(Ta_2OF_{10})$ (M = Cu, Zn) and crystallize in the space group $C2/c$. The structure of these compounds is composed of one-dimensional coordination chains involving alternating $[M(phen)_2]^{2+}$ cations and $[Ta_2OF_{10}]^{2-}$ clusters, which can be described as oxo-bridged corner sharing $[TaOF_5]^-$ octahedra (Figure 6.6). Crystallographic data for these compounds can be found in Table 6.4

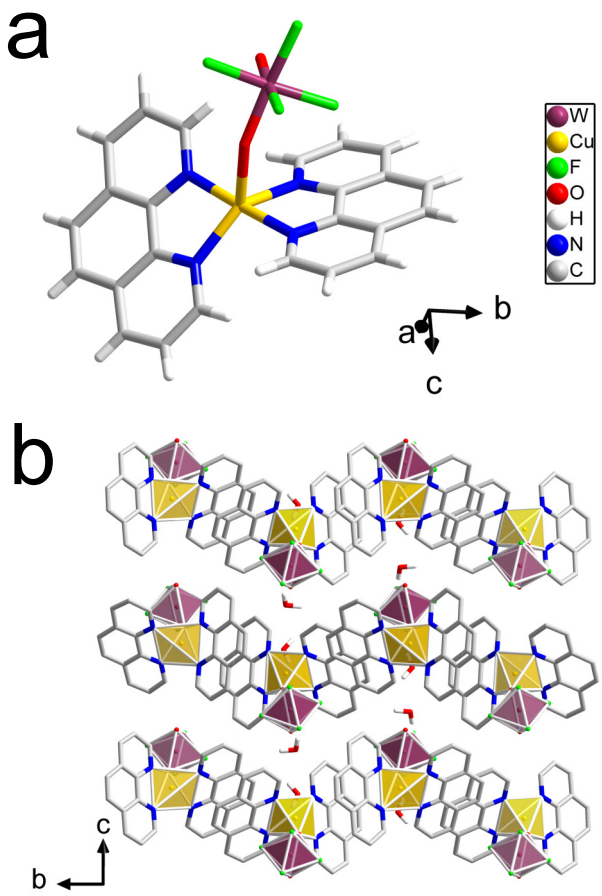

Figure 6.2. (a) Molecular structure of compound 6.3, $[Cu(phen)_2WO_2F_4]\cdot 3H_2O$. (b) Packing diagram of compound 6.3.

Compounds 6.9 and 6.10 have the formula $[Zn(phen)_2(H_2O)_2][MF_6]$ (M = Hf, Ti) and crystallize in the space group $P\bar{1}$. The structure of these compounds is based on molecular $[Zn(phen)_2(H_2O)_2]^{2+}$ cations and $[MF_6]^{2-}$ anions. Chiral $[Zn(phen)_2(H_2O)_2]^{2+}$ complexes participate in face-to-face $\pi - \pi$ stacking interactoins and form hydrogen bonds with the $[MF_6]^{2-}$ anions (Figure 6.7). Crystallographic data for these compounds can be found in Table 6.5.

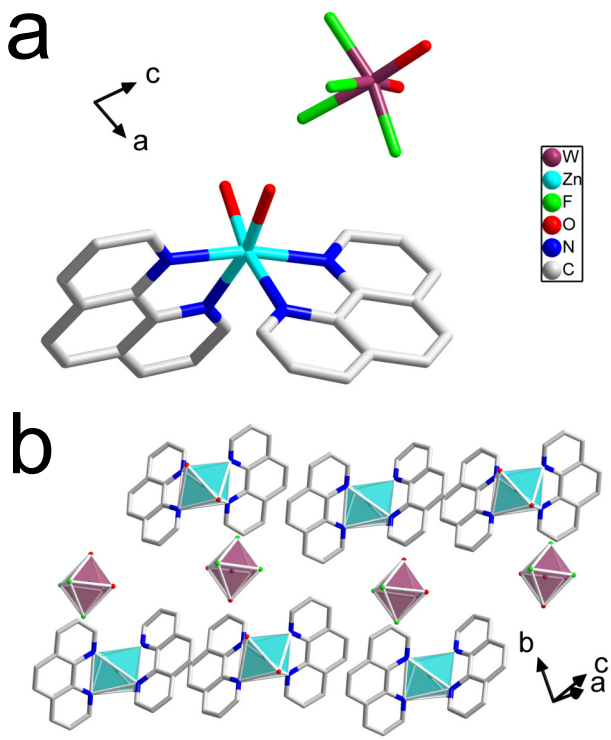

Figure 6.3. (a) Molecular structure of compound 6.4, $[Zn(phen)_2(H_2O)_2][WO_2F_4]$. (b) Packing diagram of compound 6.4.

6.3. Synthesis

Compounds 6.1 - 6.10 were synthesized via the hydrothermal pouch method.[69] After heating sealing reagents in Teflon pouches and loading pouches into Parr autoclaves, the autoclaves were heated at 150°C for 24 hours, then allowed to cool at 0.1°C/min. Crystals were recovered via vacuum filtration.

Compound 6.1 was synthesized in a pouch containing 1.69 mmol CuO, 2.56 mmol phen, 0.85 mmol Nb_2O_5, and 1 mL (27.6 mmol) HF(aq) (48%).

Compound 6.2 was synthesized in a pouch containing 1.69 mmol ZnO, 2.56 mmol phen, 0.85 mmol Nb_2O_5, and 1 mL (27.6 mmol) HF(aq) (48%).

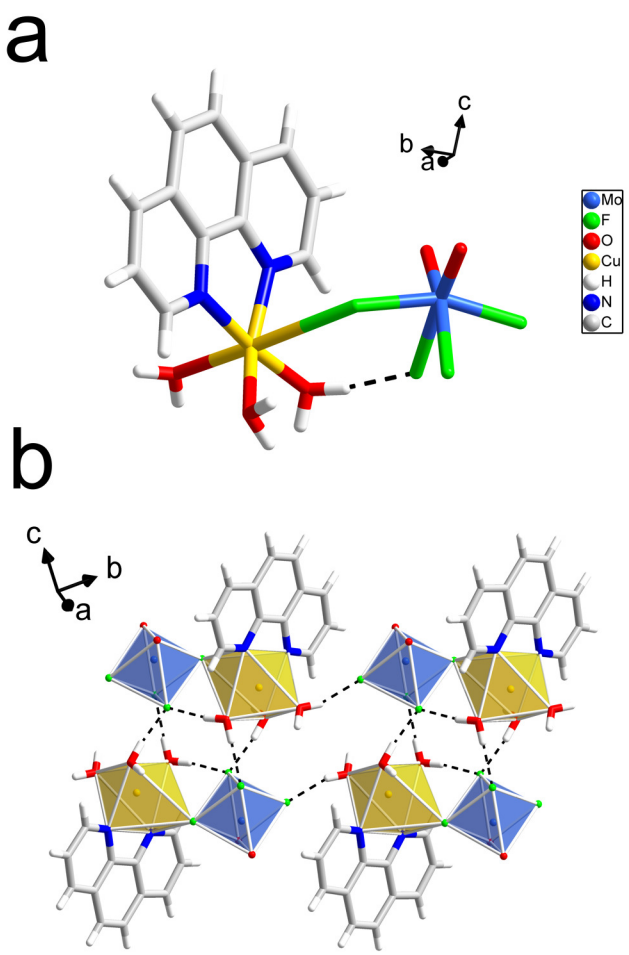

Figure 6.4. (a) Molecular structure of compound 6.5, $[Cu(phen)(H_2O)_3(MoO_2F_4)]\cdot H_2O$ (b) Packing diagram of compound 6.5.

Compound 6.3 was synthesized in a pouch containing 1.69 mmol CuO, 2.56 mmol phen, 1.69 mmol WO_3, and 1 mL (27.6 mmol) HF(aq) (48%).

Compound 6.4 was synthesized in a pouch containing 1.69 mmol ZnO, 2.56 mmol phen, 1.69 mmol WO_3, 1 mL (27.6 mmol) HF(aq) (48%).

Compound 6.5 was synthesized in a pouch containing 1.69 mmol CuO, 2.56 mmol phen, 1.69 mmol MoO_3, and 1 mL (27.6 mmol) HF(aq) (48%).

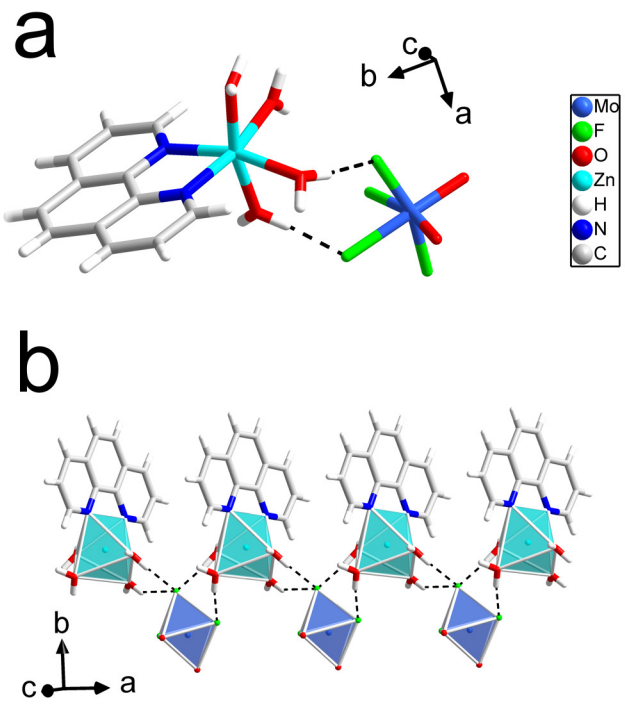

Figure 6.5. (a) Molecular structure of compound 6.6, $[Zn(phen)(H_2O)_4][MoO_2F_4]$. (b) Packing diagram of compound 6.6.

Compound 6.6 was synthesized in a pouch containing 1.69 mmol ZnO, 2.56 mmol phen, 1.69 mmol MoO_3, and 1 mL (27.6 mmol) HF(aq) (48%).

Compound 6.7 was synthesized in a pouch containing 1.69 mmol CuO, 2.56 mmol phen, 0.85 mmol Ta_2O_5, and 1 mL (27.6 mmol) HF(aq) (48%).

Compound 6.8 was synthesized in a pouch containing 1.69 mmol ZnO, 2.56 mmol phen, 0.85 mmol Ta_2O_5, and 1 mL (27.6 mmol) HF(aq) (48%).

Compound 6.9 was synthesized in a pouch containing 1.69 mmol ZnO, 3.0 mmol phen, 1.69 mmol HfO_2, 0.75 mL (20.7 mmol) HF (48%), 0.25 mL (13.8 mmol) H_2O.

Compound 6.10 was synthesized in a pouch containing 1.69 mmol ZnO, 3.0 mmol phen, 1.69 mmol TiO_2, 0.75 mL (20.7 mmol) HF (48%), 0.25 mL (13.8 mmol) H_2O.

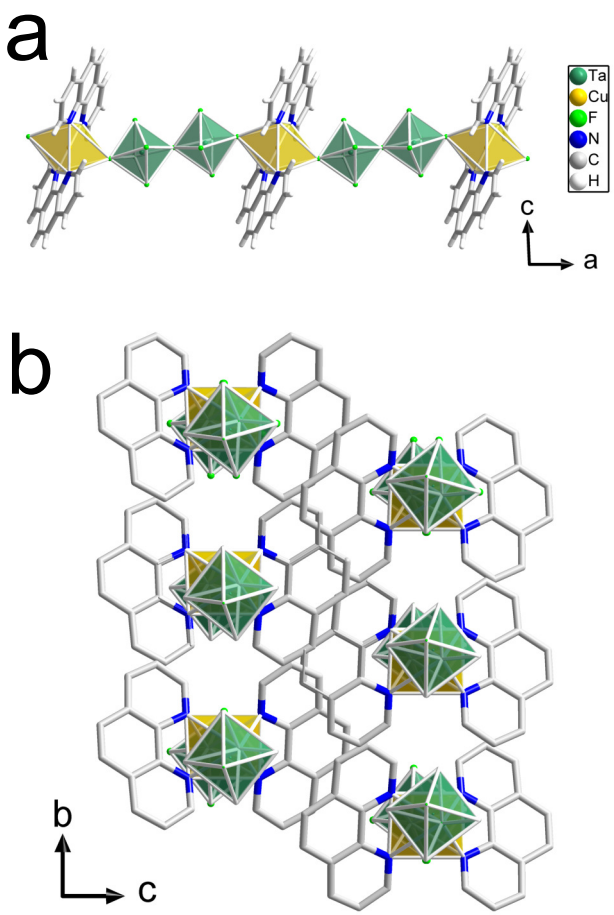

Figure 6.6. (a) Molecular structure of compounds 6.7 and 6.8, $M(phen)_2(Ta_2OF_{10})$ (M = Cu, Zn). (b) Packing diagram of compounds 6.7 and 6.8

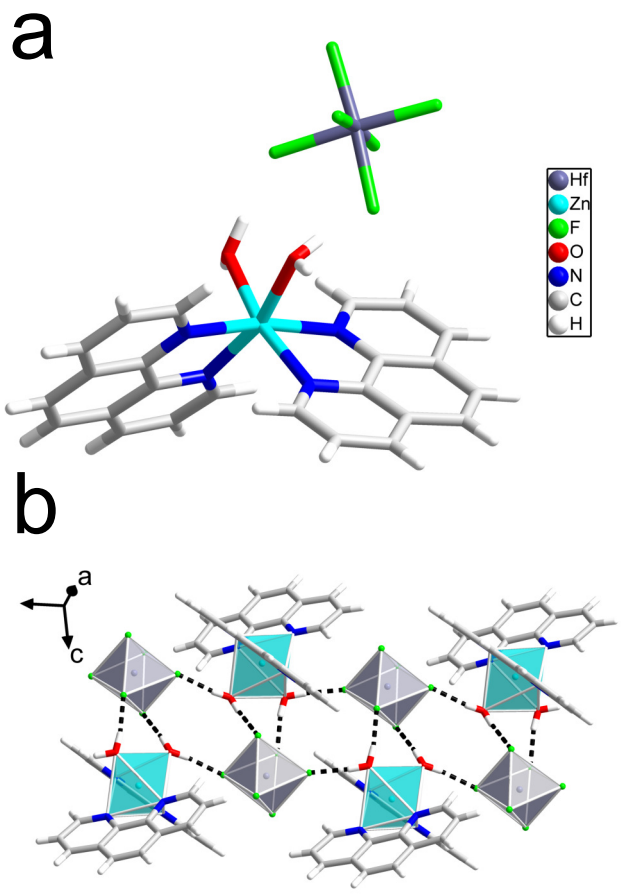

Figure 6.7. (a) Molecular structure of compounds 6.9 and 6.10, $[Zn(phen)_2(H_2O)_2][MF_6]$ (M= Hf, Ti) (b) Packing diagram of compounds 6.9 and 6.10.

Table 6.1. Crystallographic Data for Compounds 6.1 and 6.2

Identification code	MLN152B	153B
Empirical formula	$C_{48}H_{32}Cu_2F_{15}N_8Nb_3O_2$	$C_{48}H_{32}F_{15}N_8Nb_3O_2Zn_2$
Formula weight	1443.62	1446.35
Temperature/K	100.01(10)	100.01(10)
Crystal system	monoclinic	monoclinic
Space group	$P2_1/n$	$P2_1/n$
a/Å	13.3293(3)	13.2613(2)
b/Å	22.1235(4)	22.1369(3)
c/Å	17.4873(4)	17.5887(3)
α/°	90	90
β/°	109.084(2)	108.222(2)
γ/°	90	90
Volume/Å^3	4873.42(19)	4904.48(14)
Z	4	4
ρ_{calc} / g/cm^3	1.968	1.959
μ/mm^{-1}	1.651	1.749
F(000)	2832	2838
Crystal size/mm^3	0.222 × 0.198 × 0.117	0.25 × 0.21 × 0.187
Radiation	MoKα (λ = 0.71073 Å)	MoKα (λ = 0.71073 Å)
2θ range for data collection/°	4.43 to 67.892	3.854 to 61.016
Index ranges	-20 ≤ h ≤ 20, -31 ≤ k ≤ 33, -26 ≤ l ≤ 22	-18 ≤ h ≤ 18, -31 ≤ k ≤ 31, -24 ≤ l ≤ 25
Reflections collected	72767	117820
Independent reflections	17296 [R_{int} = 0.0305, R_{sigma} = 0.0301]	14955 [R_{int} = 0.0276, R_{sigma} = 0.0194]
Data/restraints/parameters	17296/0/881	14955/0/819
Goodness-of-fit on F^2	1.076	1.051
Final R indexes [I≥2σ (I)]	R_1 = 0.0403, wR_2 = 0.1096	R_1 = 0.0756, wR_2 = 0.1768
Final R indexes [all data]	R_1 = 0.0582, wR_2 = 0.1173	R_1 = 0.0880, wR_2 = 0.1849
Largest diff. peak/hole / e Å^{-3}	1.71/-1.36	2.63/-2.23
CCDC number	2059439	2062335

Table 6.2. Crystallographic Data for Compounds 6.3 and 6.4

Identification code	MLN152C	MLN153C
Empirical formula	$C_{24}H_{18}CuF_4N_4O_3W$	$C_{24}H_{20}F_4N_4O_{4.42}WZn$
Formula weight	733.81	760.38
Temperature/K	100.00(10)	100.02(10)
Crystal system	monoclinic	triclinic
Space group	$P2_1/n$	$P\bar{1}$
a/Å	8.4118(2)	9.1141(2)
b/Å	14.2866(2)	10.9862(2)
c/Å	18.3996(4)	13.2988(3)
α/°	90	74.789(2)
β/°	101.111(2)	73.216(2)
γ/°	90	83.849(2)
Volume/Å^3	2169.74(8)	1229.50(5)
Z	4	2
ρ_{calc} / g/cm^3	2.246	2.054
μ/mm^{-1}	6.351	5.722
F(000)	1412	735
Crystal size/mm^3	0.297 × 0.244 × 0.222	0.233 × 0.095 × 0.051
Radiation	MoKα (λ = 0.71073 Å)	MoKα (λ = 0.71073 Å)
2θ range for data collection/°	4.512 to 61.016	3.844 to 61.016
Index ranges	-11 ≤ h ≤ 12, -20 ≤ k ≤ 20, -26 ≤ l ≤ 26	-13 ≤ h ≤ 13, -14 ≤ k ≤ 15, -18 ≤ l ≤ 18
Reflections collected	54268	45377
Independent reflections	6620 [R_{int} = 0.0424, R_{sigma} = 0.0243]	7501 [R_{int} = 0.0811, R_{sigma} = 0.0489]
Data/restraints/parameters	6620/0/347	7501/0/379
Goodness-of-fit on F^2	1.038	1.043
Final R indexes [I≥2σ(I)]	R_1 = 0.0286, wR_2 = 0.0700	R_1 = 0.0318, wR_2 = 0.0690
Final R indexes [all data]	R_1 = 0.0345, wR_2 = 0.0724	R_1 = 0.0408, wR_2 = 0.0725
Largest diff. peak/hole / e Å^{-3}	2.94/-1.79	1.78/-1.06
CCDC number	2059438	2059444

Table 6.3. Crystallographic Data for Compounds 6.5 and 6.6

Identification code	MLN152D	MLN153D1
Empirical formula	$C_{12}H_{16}CuF_4MoN_2O_6$	$C_{12}H_{16}F_4MoN_2O_6Zn$
Formula weight	519.75	521.58
Temperature/K	100.01(10)	100.00(10)
Crystal system	triclinic	monoclinic
Space group	$P\bar{1}$	$P2_1/c$
a/Å	7.49340(10)	7.14070(10)
b/Å	9.77330(10)	23.6137(4)
c/Å	12.4348(2)	9.7238(2)
α/°	101.7570(10)	90
β/°	91.4560(10)	94.943(2)
γ/°	109.8840(10)	90
Volume/Å^3	833.96(2)	1633.51(5)
Z	2	4
ρ_{calc} / g/cm^3	2.07	2.121
μ/mm^{-1}	2.103	2.314
F(000)	514	1032
Crystal size/mm^3	0.3 × 0.269 × 0.221	0.297 × 0.183 × 0.15
Radiation	MoKα (λ = 0.71073 Å)	MoKα (λ = 0.71073 Å)
2θ range for data collection/°	4.55 to 67.532	4.544 to 67.696
Index ranges	-11 ≤ h ≤ 11, -15 ≤ k ≤ 15, -18 ≤ l ≤ 19	-9 ≤ h ≤ 10, -36 ≤ k ≤ 36, -15 ≤ l ≤ 13
Reflections collected	30480	35879
Independent reflections	6013 [R_{int} = 0.0339, R_{sigma} = 0.0271]	5837 [R_{int} = 0.0323, R_{sigma} = 0.0243]
Data/restraints/parameters	6013/15/259	5837/16/259
Goodness-of-fit on F^2	1.058	1.051
Final R indexes [I≥2σ(I)]	R_1 = 0.0255, wR_2 = 0.0682	R_1 = 0.0268, wR_2 = 0.0616
Final R indexes [all data]	R_1 = 0.0289, wR_2 = 0.0702	R_1 = 0.0326, wR_2 = 0.0639
Largest diff. peak/hole / e Å^{-3}	0.72/-0.80	1.05/-1.91
CCDC number	2059435	2059446

Table 6.4. Crystallographic Data for Compounds 6.7 and 6.8

Identification code	MLN152E	MLN153E
Empirical formula	$C_{24}H_{16}CuF_{11}N_4Ta_2$	$C_{24}H_{16}F_{11}N_4Ta_2Zn$
Formula weight	994.85	996.68
Temperature/K	100.00(10)	100.01(10)
Crystal system	monoclinic	monoclinic
Space group	$C2/c$	$C2/c$
a/Å	12.1303(2)	11.8966(2)
b/Å	13.2160(2)	13.2357(2)
c/Å	16.3754(2)	16.7407(2)
α/°	90	90
β/°	92.6240(10)	92.7450(10)
γ/°	90	90
Volume/Å^3	2622.45(7)	2632.96(7)
Z	4	4
ρ_{calc} / g/cm^3	2.52	2.514
μ/mm^{-1}	9.23	9.296
F(000)	1848	1852
Crystal size/mm^3	0.305 × 0.281 × 0.251	0.427 × 0.213 × 0.194
Radiation	MoKα (λ = 0.71073 Å)	MoKα (λ = 0.71073 Å)
2θ range for data collection/°	4.56 to 67.594	4.606 to 67.494
Index ranges	-18 ≤ h ≤ 18, -19 ≤ k ≤ 20, -24 ≤ l ≤ 24	-17 ≤ h ≤ 18, -19 ≤ k ≤ 20, -25 ≤ l ≤ 26
Reflections collected	30411	31213
Independent reflections	4759 [R_{int} = 0.0430, R_{sigma} = 0.0263]	4795 [R_{int} = 0.0353, R_{sigma} = 0.0238]
Data/restraints/parameters	4759/0/192	4795/0/191
Goodness-of-fit on F^2	1.131	1.182
Final R indexes [I≥2σ(I)]	R_1 = 0.0237, wR_2 = 0.0539	R_1 = 0.0220, wR_2 = 0.0477
Final R indexes [all data]	R_1 = 0.0257, wR_2 = 0.0546	R_1 = 0.0242, wR_2 = 0.0482
Largest diff. peak/hole / e Å^{-3}	1.88/-1.87	0.97/-1.53
CCDC number	2059434	2059445

Table 6.5. Crystallographic Data for Compounds 6.9 and 6.10

Identification code	MLN158F2	MLN159F
Empirical formula	$C_{24}H_{20}F_6HfN_4O_2Zn$	$C_{24}H_{20}F_6N_4O_2TiZn$
Formula weight	754.3	623.71
Temperature/K	101(2)	99.98(18)
Crystal system	triclinic	triclinic
Space group	$P\bar{1}$	$P\bar{1}$
a/Å	9.2480(2)	9.2775(4)
b/Å	11.3730(2)	11.1143(4)
c/Å	12.9034(3)	12.9726(5)
α/°	98.643(2)	74.682(3)
β/°	109.584(2)	69.141(4)
γ/°	99.419(2)	80.370(4)
Volume/Å^3	1230.29(5)	1201.58(9)
Z	2	2
ρ_{calc} / g/cm^3	2.036	1.724
μ/mm^{-1}	5.267	1.408
F(000)	728	628
Crystal size/mm^3	0.341 × 0.301 × 0.239	0.299 × 0.198 × 0.133
Radiation	MoKα (λ = 0.71073 Å)	MoKα (λ = 0.71073 Å)
2θ range for data collection/°	4.474 to 67.702	4.536 to 67.896
Index ranges	-13 ≤ h ≤ 12, -17 ≤ k ≤ 17, -11 ≤ l ≤ 20	-13 ≤ h ≤ 14, -16 ≤ k ≤ 16, -19 ≤ l ≤ 19
Reflections collected	8537	8230
Independent reflections	8537 [R_{int} = merged, R_{sigma} = 0.0575]	8230 [R_{int} = merged, R_{sigma} = 0.0600]
Data/restraints/parameters	8537/0/360	8230/0/360
Goodness-of-fit on F^2	1.038	1.041
Final R indexes [I≥2σ(I)]	R_1 = 0.0372, wR_2 = 0.0822	R_1 = 0.0514, wR_2 = 0.1279
Final R indexes [all data]	R_1 = 0.0429, wR_2 = 0.0842	R_1 = 0.0740, wR_2 = 0.1373
Largest diff. peak/hole / e Å^{-3}	1.87/-1.85	1.34/-0.60
CCDC number	2059436	2059437

CHAPTER 7

Future Directions and Conclusions

Our investigation of the MF_6^{2-} (M = Ti, Zr, Hf) series revealed a dramatic shift in the phase competition in the composition space of each anion that is linked to the SOJT activity of each ETM ion. Machine learning methods allowed us to leverage the data generated from exploratory synthesis, including failed or "dark reactions", to provide statistical support for the differences in phase selection between NCS and CS compounds in each composition space. Ligand K-edge XAS was employed the probe the electronic structure of each ETM anion to identify the π bonding interactions that distinguish TiF_6^{2-} from ZrF_6^{2-} and HfF_6^{2-}.

The findings of this thesis demonstrate that hydrogen bonding and $\pi-\pi$ stacking interactions dictate inversion symmetry breaking as chiral Δ- and Λ-$Cu(bpy)_2(H_2O)^{2+}$ coordination complexes assemble into the polar structure of the $[Cu(bpy)_2(H_2O)][MF_6]\cdot 1.5H_2O$ (M = Ti, Zr, Hf) family. Centrosymmetry emerges in the $[Cu(phen)_2(H_2O)][MF_6]$ (M = Ti, Zr, Hf) series via a slight reorientation of $\pi - \pi$ contacts between $Cu(phen)_2(H_2O)^{2+}$ complexes, which are always found to adopt parallel $\pi - \pi$ stacking contacts, whereas $Cu(bpy)_2(H_2O)^{2+}$ can adopt either parallel or nonparallel stacking configurations. This study illustrated how encouraging non-parallel $\pi - \pi$ stacking contacts is a necessary but insufficient condition for bulk inversion symmetry breaking. Interrogation of the main group SiF_6^{2-} and SnF_6^{2-} anions resulted in the synthesis of the CS compound $[Cu(Bpy)_2(H_2O)][SiF_6]\cdot 4H_2O$, which displays increased incorporation of hydrating water relative to its NCS ETM counterparts,

as well as the CS coordination polymer $[Cu(Bpy)(H_2O)_2SnF_6]_n$, which is isostructural to $[Cu(Bpy)(H_2O)_2HfF_6]_n$.

Further investigation is required to elucidate general principles of symmetry breaking in racemic compounds, including experimental studies of particular systems and examination of structures deposited within the Cambridge Structural Database. To gain further insight into the $[Cu(bpy)_2(H_2O)][MF_6]\cdot 1.5H_2O$ (M = Ti, Zr, Hf), ligand functionalization with methyl groups at various ring positions could allow for the adjustment of steric interactions between adjacent bpy ligands to further probe the$\pi - \pi$ stacking interactions between adjacent chiral $Cu(bpy)_2(H_2O)^{2+}$ complexes. In addition, other functional groups such as carboxylic acids or amine groups could be added to bpy ligands to introduce hydrogen bond donor/acceptor groups that could perturb the energy landscape that dictates the observed packing mode. One promising route for future synthetic work outside of the $[Cu(bpy)_2(H_2O)][MF_6]\cdot 1.5H_2O$ (n M = Ti, Zr, Hf) family would be to examine whether racemic combinations of chiral building units found in existing NCS racemates are potential hosts for incorporating polar anions or other functional building units into polar NCS structures. One system of note is DL-alanine, which adopts a AN racemic structure, as well as a known salt in which protonated D- and L-alanine molecules as well as SiF_6^{2-} anions are incorporated within a kryptoracemic polar NCS structure.[161] Composition space studies to determine whether this structure-type can accommodate ETM fluorides and oxide-fluorides could lead to novel polar compounds.

Using computational methods to identify NCS racemic compounds as well as analogous CS compounds based on the same building units would be of immense interest. For example, a targeted search of structures reported in the Cambridge Structural Database on the basis of molecular symmetry would allow for the elucidation of trends between optically active

racemates with various symmetries as well as optically inactive racemates that are NCS according to the symmetry-dependent structure property relationships summarized in Figure 1.1. Such a search could be accomplished by using Conquest,[162] which is part of the CSD software suite,,[142] to download crystallographic data files (.CIF) for compounds crystallizing in the non-enantiomorphic point groups shown in Figure 1.1 in which racemic compounds are allowed to crystallize. Once a database of compounds with appropriate crystallographic point group symmetry has been compiled, a secondary screening can be performed using a program such as SYMMOL[163,164] (implemented as MOLSYM in PLATON) to identify molecular point group symmetry within each structure. Compounds which crystallize in space groups containing improper symmetry operations (inversion, rotoinverion, mirror/glide planes) containing molecules with chiral point symmetry can be assiged as racemic. Examination of this database of AN racemic compounds would lead to the identification of chiral building units that could then be used as the starting point for the identification of pairs of NCS and CS compounds based on the same or similar building units to identify important structural features. Such a search could also lead to the identification of unixial optically active racemates that would enable the measurement of optical activity from a racemic compound for the first time. Attempts to measure optical activity have been inconclusive to this point owing to the birefringence of NCS racemates available to the authors.

Although the performance of NCS racemates has been shown to be comparable to their enantiomerically pure counterparts in some cases, the question remains whether racemates have clear advantages or distinct behaviors relative to conventional NCS materials. One potential advantage is the inherent quasi-phase matching that some racemates may possess on the basis of the equal and opposite nonlinear optical coefficients of chiral molecules with opposite handedness.[165] This concept has been demonstrated in Langmuir-Blodgett films

but has not yet been realized in a bulk material. If a suitable material can be identified, inherent quasi-phase matching would represent a significant advantage over conventional quasi-phase matched materials, such as periodically poled lithium niobate, which must be post-synthetically poled via external electric fields.

Beyond controlling bulk crystallographic symmetry, future investigation of local structure in NCS materials could lead to new design rules for improved properties. Chapter 2 of this thesis presents the example of NMR revealing the local dynamic motion of MF_6^{2-} (M = Ti, Zr, Hf) anions that were previously thought to behave as rigid, static polyhedra. Further studies of the compounds presented in Chapter 6 via NMR and EXAFS could provide critical insight in identifying structural features, such as hydrogen bonding contacts, that facilitate local dynamics. Studies of local atomic structure should be supplemented by examination of the local electronic structure using ligand K-edge X-ray absorption spectroscopy. Studies of this type will allow for elucidation of the differential in covalency in M-O and M-F bonds that is thought to lead to out-of-center distortions in ETM oxide-fluorides. Detailed examination of the local atomic and electronic structure are needed for the development of an experimentally-verified microscopic theory for local structure in ETM fluorides and oxide-fluorides.

Materials with broken inversion symmetry will play a key role in developing new technology in the near future. Achieving cooperative interactions between chirality and polarity would have immense technological consequences in multiferroics, spin polarization materials, optical switching and polarization modulation. Noncentrosymmetric materials have transformed numerous aspects of society, yet vast potential for new applications and increased implementation remains. In particular, photonic materials are highly sought after to take advantage of the ability to control the phase, amplitude, and polarization states

for optical communication systems. Materials with lower processing costs and higher performance/efficiency will be highly valuable as next generation technologies, such as optical communications systems and ferroelectric memories, are implemented. One example of ongoing efforts to discover NCS materials that enable new applications is the push to break the so-called "200 nm wall". Nonlinear optical crystals with transparency in the deep-UV (DUV) are highly sought after for short wave lasers. DUV lasers have been critical in realizing laboratory angle-resolved photoelectron spectroscopy (ARPES) experiments, which conventionally rely on synchrotron radiation sources, as well as industrial applications such as micro-machining and photolithography.[166–169] Another area of recent rapid improvement in the field of NCS materials has been the development of materials based on the combination of multiple anionic groups within a single molecular building unit, which are known as poly-anions.[170] By controlling the arrangement of poly-anions as a single entity rather than as independent moieties, numerous high-efficiency NLO materials have been realized.

References

[1] J. F. Nye, *Physical Properties of Crystals: Their Representation by Tensors and Matrices*, Clarendon Press - Oxford, **1985**.

[2] P. S. Halasyamani, K. R. Poeppelmeier. Noncentrosymmetric Oxides. *Chem. Mater.* **1998**, *10*, 2753–2769.

[3] R. Masse, J. Zyss. A new approach in the design of polar crystals for quadratic nonlinear optics exemplified by the synthesis and crystal structure of 2-amino-5-nitropyridinium dihydrogen monophosphate (2A5NPDP). *Mol. Eng.* **1991**, *1*, 141–152.

[4] J. Zyss, J. F. Nicoud, M. Coquillay. Chirality and hydrogen bonding in molecular crystals for phase-matched second-harmonic generation: N-(4-nitrophenyl)-(L)-prolinol (NPP). *J. Chem. Phys.* **1984**, *81*, 4160–4167.

[5] J. Zyss, D. S. Chemla, J. F. Nicoud. Demonstration of efficient nonlinear optical crystals with vanishing molecular dipole moment: Second-harmonic generation in 3-methyl-4-nitropyridine-1-oxide. *J. Chem. Phys.* **1981**, *74*, 4800–4811.

[6] J. Zyss. Engineering new organic crystals for nonlinear optics: from molecules to oscillator. *J. Phys. D: Appl. Phys.* **1993**, *26*, B198.

[7] J. Zyss, I. Ledoux. Nonlinear optics in multipolar media: theory and experiments. *Chem. Rev.* **1994**, *94*, 77–105.

[8] H.-Y. Zhang, Y.-Y. Tang, P.-P. Shi, R.-G. Xiong. Toward the Targeted Design of Molecular Ferroelectrics: Modifying Molecular Symmetries and Homochirality. *Acc. Chem. Res.* **2019**, *52*, 1928–1938.

[9] P.-F. Li, W.-Q. Liao, Y.-Y. Tang, W. Qiao, D. Zhao, Y. Ai, Y.-F. Yao, R.-G. Xiong. Organic enantiomeric high-T_c ferroelectrics. *PNAS* **2019**, *116*, 5878–5885.

[10] H.-Y. Ye, Y.-Y. Tang, P.-F. Li, W.-Q. Liao, J.-X. Gao, X.-N. Hua, H. Cai, P.-P. Shi, Y.-M. You, R.-G. Xiong. Metal-free three-dimensional perovskite ferroelectrics. *Science* **2018**, *361*, 151–155.

[11] D.-W. Fu, H.-L. Cai, Y. Liu, Q. Ye, W. Zhang, Y. Zhang, X.-Y. Chen, G. Giovannetti, M. Capone, J. Li, R.-G. Xiong. Diisopropylammonium Bromide Is a High-Temperature Molecular Ferroelectric Crystal. *Science* **2013**, *339*, 425–428.

[12] D.-W. Fu, H.-Y. Ye, Q. Ye, K.-J. Pan, R.-G. Xiong. Ferroelectric metal–organic coordination polymer with a high dielectric constant. *Dalton Trans.* **2008**, *0*, 874–877.

[13] Y.-M. You, W.-Q. Liao, D. Zhao, H.-Y. Ye, Y. Zhang, Q. Zhou, X. Niu, J. Wang, P.-F. Li, D.-W. Fu, Z. Wang, S. Gao, K. Yang, J.-M. Liu, J. Li, Y. Yan, R.-G. Xiong. An organic-inorganic perovskite ferroelectric with large piezoelectric response. *Science* **2017**, *357*, 306–309.

[14] W. Zhang, R.-G. Xiong. Ferroelectric Metal–Organic Frameworks. *Chem. Rev.* **2012**, *112*, 1163–1195.

[15] P.-P. Shi, Y.-Y. Tang, P.-F. Li, W.-Q. Liao, Z.-X. Wang, Q. Ye, R.-G. Xiong. Symmetry breaking in molecular ferroelectrics. *Chem. Soc. Rev.* **2016**, *45*, 3811–3827.

[16] Q. Ye, D.-W. Fu, H. Tian, R.-G. Xiong, P. W. H. Chan, S. D. Huang. Multiferroic Homochiral Metal-Organic Framework. *Inorg. Chem.* **2008**, *47*, 772–774.

[17] J. Jacques, A. Collet, S. H. Wilen, *Enantiomers, racemates, and resolutions*, Krieger Pub. Co., **1994**.

[18] E. A. Muller, R. J. Cannon, A. N. Sarjeant, K. M. Ok, P. S. Halasyamani, A. J. Norquist. Directed Synthesis of Noncentrosymmetric Molybdates. *Cryst. Growth Des.* **2005**, *5*, 1913–1917.

[19] T. R. Veltman, A. K. Stover, A. Narducci Sarjeant, K. M. Ok, P. S. Halasyamani, A. J. Norquist. Directed Synthesis of Noncentrosymmetric Molybdates Using Composition Space Analysis. *Inorg. Chem.* **2006**, *45*, 5529–5537.

[20] D. J. Hubbard, A. R. Johnston, H. S. Casalongue, A. N. Sarjeant, A. J. Norquist. Synthetic Approaches for Noncentrosymmetric Molybdates. *Inorg. Chem.* **2008**, *47*, 8518–8525.

[21] E. C. Glor, S. M. Blau, J. Yeon, M. Zeller, P. Shiv Halasyamani, J. Schrier, A. J. Norquist. [R-$C_7H_{16}N_2$][$V_2Te_2O_{10}$] and [S-$C_7H_{16}N_2$][$V_2Te_2O_{10}$]; new polar templated vanadium tellurite enantiomers. *J. Solid State Chem.* **2011**, *184*, 1445–1450.

[22] R. Gautier, A. J. Norquist, K. R. Poeppelmeier. From Racemic Units to Polar Materials. *Cryst. Growth Des.* **2012**, *12*, 6267–6271.

[23] R. Gautier, K. R. Poeppelmeier. Preservation of Chirality and Polarity between Chiral and Polar Building Units in the Solid State. *Inorg. Chem.* **2012**, *51*, 10613–10618.

[24] H. D. Flack. Chiral and Achiral Crystal Structures. *HCA* **2003**, *86*, 905–921.

[25] T. Rekis. Crystallization of chiral molecular compounds: what can be learned from the Cambridge Structural Database? *Acta Cryst. B* **2020**, *76*, 307–315.

[26] B. Dalhus, C. H. Görbitz. Non-centrosymmetric racemates: space-group frequencies and conformational similarities between crystallographically independent molecules. *Acta Crystallogr., Sect. B: Struct. Sci.* **2000**, *56*, 715–719.

[27] K. E. Rieckhoff, W. L. Peticolas. Optical Second-Harmonic Generation in Crystalline Amino Acids. *Science* **1965**, *147*, 610–611.

[28] V. V. Lemanov. Ferroelectric and piezoelectric properties of protein amino acids and their compounds. *Phys. Solid State* **2012**, *54*, 1841–1842.

[29] V. V. Lemanov, S. N. Popov, G. A. Pankova. Piezoelectricity in protein amino acids. *Phys. Solid State* **2011**, *53*, 1191–1193.

[30] S. Guerin, J. O'Donnell, E. U. Haq, C. McKeown, C. Silien, F. M. F. Rhen, T. Soulimane, S. A. M. Tofail, D. Thompson. Racemic Amino Acid Piezoelectric Transducer. *Phys. Rev. Lett.* **2019**, *122*, 047701.

[31] S. A. Martin Britto Dhas, S. Natarajan. Growth and characterization of dl-Alanine — A new NLO material from the amino acid family. *Materials Letters* **2008**, *62*, 2633–2636.

[32] D. Vasilescu, R. Cornillon, G. Mallet. Piezoelectric Resonances in Amino-acids. *Nature* **1970**, *225*, 635–635.

[33] L. Fabian, C. P. Brock. A list of organic kryptoracemates. *Acta Crystallogr., Sect. B: Struct. Sci.* **2010**, *66*, 94–103.

[34] I. Bernal, S. Watkins. A list of organometallic kryptoracemates. *Acta Crystallogr., Sect. C: Cryst. Struct. Chem.* **2015**, *71*, 216–221.

[35] S. Clevers, G. Coquerel. Kryptoracemic compound hunting and frequency in the Cambridge Structural Database. *CrystEngComm* **2020**, Publisher: The Royal Society of Chemistry.

[36] C. Chen. An Ionic Grouping Theory of the Electro-Optical and Non-linear Optical Effects of Crystals - A Theoretical Calculation of Electro-optical and Second Harmonic

Coefficients of Barium Titanate Crystals Based on a Deformed Oxygen-Octahedra. *Acta Physica Sinica* **1976**, *25*, 146–161.

[37] C. Chen, Y. Wu, R. Li. The anionic group theory of the non-linear optical effect and its applications in the development of new high-quality NLO crystals in the borate series. *Int. Rev. Phys. Chem.* **1989**, *8*, 65–91.

[38] C. Randall, R. Newnham, L. Cross. History of the first ferroelectric oxide, $BaTiO_3$. *Materials Research Institute, The Pennsylvania State University, University Park, Pa, USA* **2004**, *1*.

[39] L. Cross, R. Newnham. History of ferroelectrics. *Ceramics and civilization* **1987**, *3*, 289–305.

[40] A. Lüker. A short history of ferroelectricity. *Instituto Superior Técnico Departamento de Física* **2011**.

[41] B. Jaffe, R. S. Roth, S. Marzullo. Piezoelectric Properties of Lead Zirconate-Lead Titanate Solid-Solution Ceramics. *Journal of Applied Physics* **1954**, *25*, 809–810.

[42] G. D. Stucky, M. L. F. Phillips, T. E. Gier. The potassium titanyl phosphate structure field: a model for new nonlinear optical materials. *Chem. Mater.* **1989**, *1*, 492–509.

[43] M. E. Hagerman, K. R. Poeppelmeier. Review of the Structure and Processing-Defect-Property Relationships of Potassium Titanyl Phosphate: A Strategy for Novel Thin-Film Photonic Devices. *Chem. Mater.* **1995**, *7*, 602–621.

[44] R. S. Weis, T. K. Gaylord. Lithium niobate: Summary of physical properties and crystal structure. *Appl. Phys. A* **1985**, *37*, 191–203.

[45] U. Opik, M. H. L. Pryce. Studies of the Jahn-Teller Effect. I. A Survey of the Static Problem. *Proceedings of the Royal Society A: Mathematical, Physical and Engineering Sciences* **1957**, *238*, 425–447.

[46] R. G. Pearson. The second-order Jahn-Teller effect. *Journal of Molecular Structure: THEOCHEM* **1983**, *103*, 25–34.

[47] R. E. Cohen. Origin of ferroelectricity in perovskite oxides. *Nature* **1992**, *358*, 136.

[48] M. Kunz, I. D. Brown. Out-of-Center Distortions around Octahedrally Coordinated d^0 Transition Metals. *J. Solid State Chem.* **1995**, *115*, 395–406.

[49] I. B. Bersuker. Pseudo-Jahn–Teller Effect—A Two-State Paradigm in Formation, Deformation, and Transformation of Molecular Systems and Solids. *Chem. Rev.* **2013**, *113*, 1351–1390.

[50] I. B. Bersuker, V. Polinger. Perovskite Crystals: Unique Pseudo-Jahn–Teller Origin of Ferroelectricity, Multiferroicity, Permittivity, Flexoelectricity, and Polar Nanoregions. *Condensed Matter* **2020**, *5*, 68.

[51] I. B. Bersuker. Jahn–Teller and Pseudo-Jahn–Teller Effects: From Particular Features to General Tools in Exploring Molecular and Solid State Properties. *Chem. Rev.* **2021**, *121*, 1463–1512.

[52] E. A. Stern. Character of Order-Disorder and Displacive Components in Barium Titanate. *Phys. Rev. Lett.* **2004**, *93*, 037601.

[53] E.-a. Kim, D. W. Lee, K. M. Ok. Centrosymmetric $[N(CH_3)_4]_2TiF_6$ vs. noncentrosymmetric polar $[C(NH_2)_3]_2TiF_6$: A hydrogen-bonding effect on the out-of-center distortion of TiF_6 octahedra. *J. Solid State Chem.* **2012**, *195*, 149–154.

[54] M. L. Nisbet, I. M. Pendleton, G. M. Nolis, K. J. Griffith, J. Schrier, J. Cabana, A. J. Norquist, K. R. Poeppelmeier. Machine-Learning-Assisted Synthesis of Polar Racemates. *J. Am. Chem. Soc.* **2020**, *142*, 7555–7566.

[55] M. E. Welk, A. J. Norquist, C. L. Stern, K. R. Poeppelmeier. The Ordered $[WO_2F_4]^{2-}$ Anion. *Inorg. Chem.* **2001**, *40*, 5479–5480.

[56] M. E. Welk, A. J. Norquist, F. P. Arnold, C. L. Stern, K. R. Poeppelmeier. Out-of-Center Distortions in d^0 Transition Metal Oxide Fluoride Anions. *Inorg. Chem.* **2002**, *41*, 5119–5125.

[57] M. E. Welk, A. J. Norquist, C. L. Stern, K. R. Poeppelmeier. The Structure-Directing Properties of $[VOF_5]^{2-}$. *Inorg. Chem.* **2000**, *39*, 3946–3947.

[58] H. Lu, R. Gautier, M. D. Donakowski, L. Fuoco, Z. Liu, K. R. Poeppelmeier. Specific Chemistry of the Anions: $[TaOF_5]^{2-}$, $[TaF_6]^{-}$, and $[TaF_7]^{2-}$. *Cryst. Growth Des.* **2014**, *14*, 844–850.

[59] M. R. Marvel, J. Lesage, J. Baek, P. S. Halasyamani, C. L. Stern, K. R. Poeppelmeier. Cation-Anion Interactions and Polar Structures in the Solid State. *J. Am. Chem. Soc.* **2007**, *129*, 13963–13969.

[60] R. Gautier, M. D. Donakowski, K. R. Poeppelmeier. Orientational order of $[VOF_5]^{2-}$ and $[NbOF_5]^{2-}$ polar units in chains. *J. Solid State Chem.* **2012**, *195*, 132–139.

[61] P. A. Maggard, T. S. Nault, C. L. Stern, K. R. Poeppelmeier. Alignment of acentric $MoO_3F_3^{3-}$ anions in a polar material: $(Ag_3MoO_3F_3)(Ag_3MoO_4)Cl$. *J. Solid State Chem.* **2003**, *175*, 27–33.

[62] M. D. Donakowski, A. I. Vinokur, K. R. Poeppelmeier. The Dimeric $[V_2O_4F_6]^{4-}$ Vanadium Oxide-Fluoride Anion in $Na_2(M(H_2O)_2)(V_2O_4F_6)$ ($M = Co^{2+}$, Ni^{2+}, and Cu^{2+}). *Z. Anorg. Allg. Chem.* **2012**, *638*, 1991–1995.

[63] K. R. Heier, A. J. Norquist, P. S. Halasyamani, A. Duarte, C. L. Stern, K. R. Poeppelmeier. The Polar $[WO_2F_4]^{2-}$ Anion in the Solid State. *Inorg. Chem.* **1999**, *38*, 762–767.

[64] M. D. Donakowski, R. Gautier, H. Lu, T. T. Tran, J. R. Cantwell, P. S. Halasyamani, K. R. Poeppelmeier. Syntheses of Two Vanadium Oxide–Fluoride Materials That Differ in Phase Matchability. *Inorg. Chem.* **2015**, *54*, 765–772.

[65] H. Lu, R. Gautier, M. D. Donakowski, T. Tran, B. W. Edwards, J. C. Nino, P. S. Halasyamani, Z. Liu, K. R. Poeppelmeier. Nonlinear Active Materials: An Illustration of Controllable Phase Matchability. *J. Am. Chem. Soc.* **2013**, *135*, 11942–11950.

[66] R. Gautier, R. Gautier, K. B. Chang, K. R. Poeppelmeier. On the Origin of the Differences in Structure Directing Properties of Polar Metal Oxyfluoride $[MO_xF_{6-x}]^{2-}$ (x = 1, 2) Building Units. *Inorg. Chem.* **2015**, *54*, 1712–1719.

[67] R. Gautier, K. R. Poeppelmeier. Alignment of Acentric Units in Infinite Chains: A "Lock and Key" Model. *Cryst. Growth Des.* **2013**, *13*, 4084–4091.

[68] A. Rabenau. The Role of Hydrothermal Synthesis in Preparative Chemistry. *Angew. Chem. Int. Ed. Engl.* **1985**, *24*, 1026–1040.

[69] W. T. A. Harrison, T. M. Nenoff, T. E. Gier, G. D. Stucky. Tetrahedral-atom 3-ring groupings in 1-dimensional inorganic chains: beryllium arsenate hydroxide hydrate ($Be_2AsO_4OH \cdot 4H_2O$) and sodium zinc hydroxide phosphate hydrate ($Na_2ZnPO_4OH \cdot H_2O$). *Inorg. Chem.* **1993**, *32*, 2437–2441.

[70] J. C. Jacco, *$KTiOPO_4$ (KTP) Past, Present, And Future* in *Ceramics and Inorganic Crystals for Optics, Electro-Optics, and Nonlinear Conversion*, International Society for Optics and Photonics, pp. 93–100.

[71] A. von Hippel. Ferroelectricity, Domain Structure, and Phase Transitions of Barium Titanate. *Rev. Mod. Phys.* **1950**, *22*, 221–237.

[72] K. Nassau, H. J. Levinstein, G. M. Loiacono. Ferroelectric lithium niobate. 1. Growth, domain structure, dislocations and etching. *J. Phys. Chem. Solids* **1966**, *27*, 983–988.

[73] K. M. Rabe, C. H. Ahn, J.-M. Triscone (Eds.), *Physics of ferroelectrics: a modern perspective*, of *Topics in applied physics*, Springer, Berlin ; New York, **2007**.

[74] R. A. Wheeler, M. H. Whangbo, T. Hughbanks, R. Hoffmann, J. K. Burdett, T. A. Albright. Symmetric vs. asymmetric linear M-X-M linkages in molecules, polymers, and extended networks. *J. Am. Chem. Soc.* **1986**, *108*, 2222–2236.

[75] J. K. Harada, N. Charles, K. R. Poeppelmeier, J. M. Rondinelli. Heteroanionic Materials by Design: Progress Toward Targeted Properties. *Adv. Mater.* **2019**, *31*, 1805295.

[76] H. Kageyama, K. Hayashi, K. Maeda, J. P. Attfield, Z. Hiroi, J. M. Rondinelli, K. R. Poeppelmeier. Expanding frontiers in materials chemistry and physics with multiple anions. *Nat Commun* **2018**, *9*.

[77] J. R. Gutnick, E. A. Muller, A. Narducci Sarjeant, A. J. Norquist. $[C_5H_{14}N_2][(MoO_3)_3(SO_4)]$*$H_2O$: Sulfated alpha-Molybdena Chains. *Inorg. Chem.* **2004**, *43*, 6528–6530.

[78] H. A. Levy, R. B. Corey. The Crystal Structure of dl-Alanine. *J. Am. Chem. Soc.* **1941**, *63*, 2095–2108.

[79] L. Lo Presti, M. Sist, L. Loconte, A. Pinto, L. Tamborini, C. Gatti. Rationalizing the Lacking of Inversion Symmetry in a Noncentrosymmetric Polar Racemate: An Experimental and Theoretical Study. *Cryst. Growth Des.* **2014**, *14*, 5822–5833.

[80] P. S. Carvalho, J. Ellena, D. S. Yufit, J. A. K. Howard. Rare Case of Polymorphism in a Racemic Fluoxetine Nitrate Salt: Phase Behavior and Relative Stability. *Cryst. Growth Des.* **2016**, *16*, 3875–3883.

[81] B. Ravikumar, B. Sridhar, R. K. Rajaram. dl-Phenyl-alaninium di-hydrogen phosphate. *Acta Cryst E* **2001**, *57*, o1078–o1080.

[82] S. Kumar, K. Subramanian, A. M. Schreurs, J. Kroon, T. Steiner. Racemic γ-2-cis-6-diphenyl-trans-3-ethylpiperidin-4-one oxime, a crystal structure with Z' = 8. *J. Chem. Crystallogr.* **2001**, *31*, 411–416.

[83] R. Gautier, J. M. Klingsporn, R. P. Van Duyne, K. R. Poeppelmeier. Optical activity from racemates. *Nat. Mater.* **2016**, *15*, 591–592.

[84] B. Kahr, A. T. Martin, K.-H. Ernst. On the chiroptical properties of racemic crystals. *Chirality* **2018**.

[85] P. Halasyamani, M. J. Willis, C. L. Stern, P. M. Lundquist, G. K. Wong, K. R. Poeppelmeier. Composition Space of the $(CuO, 1/2Nb_2O_5)/(HF)_x$. pyridine/H_2O System.

Structure and Synthesis of $[pyH^+]_2[CuNb_2(py)_4O_2F_{10}]^{2-}$ and $CuNb(py)_4OF_5$. *Inorg. Chem.* **1996**, *35*, 1367–1371.

[86] A. J. Norquist, K. R. Heier, C. L. Stern, K. R. Poeppelmeier. Composition Space Diagrams for Mixed Transition Metal Oxide Fluorides. *Inorg. Chem.* **1998**, *37*, 6495–6501.

[87] T. Mueller, A. G. Kusne, R. Ramprasad, *Machine Learning in Materials Science* in *Reviews in Computational Chemistry*, John Wiley & Sons, Ltd, **2016**, pp. 186–273.

[88] Y. S. Abu-Mostafa, M. Magdon-Ismail, H.-T. Lin, *Learning From Data*, AMLBook, S.l., **2012**.

[89] P. Raccuglia, K. C. Elbert, P. D. F. Adler, C. Falk, M. B. Wenny, A. Mollo, M. Zeller, S. A. Friedler, J. Schrier, A. J. Norquist. Machine-learning-assisted materials discovery using failed experiments. *Nature* **2016**, *533*, 73–76.

[90] A. S. Vinogradov, S. I. Fedoseenko, S. A. Krasnikov, A. B. Preobrajenski, V. N. Sivkov, D. V. Vyalikh, S. L. Molodtsov, V. K. Adamchuk, C. Laubschat, G. Kaindl. Low-lying unoccupied electronic states in $3d$ transition-metal fluorides probed by NEXAFS at the F $1s$ threshold. *Phys. Rev. B* **2005**, *71*.

[91] F. de Groot, G. Vankó, P. Glatzel. The $1s$ x-ray absorption pre-edge structures in transition metal oxides. *J. Phys.: Condens. Matter* **2009**, *21*, 104207.

[92] G. M. Sheldrick. Crystal structure refinement with SHELXL. *Acta Crystallogr., Sect. C: Struct. Chem.* **2015**, *71*, 3–8.

[93] *SAINT V8.38A; Bruker Analytical X-ray Instruments: Madison, WI, USA*, **2016**.

[94] G. M. Sheldrick, *SADABS; University of Göttingen: Göttingen, Germany*, **2002**.

[95] A. L. Spek. Single-crystal structure validation with the program PLATON. *J. Appl. Crystallogr.* **2003**, *36*, 7–13.

[96] O. V. Dolomanov, L. J. Bourhis, R. J. Gildea, J. a. K. Howard, H. Puschmann. OLEX2: a complete structure solution, refinement and analysis program. *J. Appl. Crystallogr.* **2009**, *42*, 339–341.

[97] I. M. Pendleton, G. Cattabriga, Z. Li, M. A. Najeeb, S. A. Friedler, A. J. Norquist, E. M. Chan, J. Schrier. Experiment Specification, Capture and Laboratory Automation Technology (ESCALATE): a software pipeline for automated chemical experimentation and data management. *MRS Communications* **2019**, *9*, 846–859.

[98] M. J. Frisch, G. W. Trucks, J. R. Cheeseman, G. Scalmani, M. Caricato, H. P. Hratchian, X. Li, V. Barone, J. Bloino, G. Zheng, T. Vreven, J. A. Montgomery, G. A. Petersson, G. E. Scuseria, H. B. Schlegel, H. Nakatsuji, A. F. Izmaylov, R. L. Martin, J. L. Sonnenberg, J. E. Peralta, J. J. Heyd, E. Brothers, F. Ogliaro, M. Bearpark, M. A. Robb, B. Mennucci, K. N. Kudin, V. N. Staroverov, R. Kobayashi, J. Normand, A. Rendell, R. Gomperts, V. G. Zakrzewski, M. Hada, M. Ehara, K. Toyota, R. Fukuda, J. Hasegawa, M. Ishida, T. Nakajima, Y. Honda, O. Kitao, H. Nakai, *Gaussian 09*, Gaussian Inc. Wallingford CT 2009.

[99] M. Bühl, H. Kabrede. Geometries of Transition-Metal Complexes from Density-Functional Theory. *J. Chem. Theory Comput.* **2006**, *2*, 1282–1290, Publisher: American Chemical Society.

[100] A. V. Marenich, S. V. Jerome, C. J. Cramer, D. G. Truhlar. Charge Model 5: An Extension of Hirshfeld Population Analysis for the Accurate Description of Molecular Interactions in Gaseous and Condensed Phases. *J. Chem. Theory Comput.* **2012**, *8*, 527–541.

[101] F. Pedregosa, G. Varoquaux, A. Gramfort, V. Michel, B. Thirion, O. Grisel, M. Blondel, P. Prettenhofer, R. Weiss, V. Dubourg, J. Vanderplas, A. Passos, D. Cournapeau, M. Brucher, M. Perrot, É. Duchesnay. Scikit-learn: Machine Learning in Python. *J. Mach. Learn. Res.* **2011**, *12*, 2825–2830.

[102] A. Bielecki, D. P. Burum. Temperature Dependence of ^{207}Pb MAS Spectra of Solid Lead Nitrate. An Accurate, Sensitive Thermometer for Variable-Temperature MAS. *J. Magn. Reson. A* **1995**, *116*, 215–220.

[103] P. A. Beckmann, C. Dybowski. A Thermometer for Nonspinning Solid-State NMR Spectroscopy. *J. Magn. Reson.* **2000**, *146*, 379–380.

[104] R. Gautier, K. Oka, T. Kihara, N. Kumar, A. Sundaresan, M. Tokunaga, M. Azuma, K. R. Poeppelmeier. Spin Frustration from *cis* -Edge or -Corner Sharing Metal-Centered Octahedra. *J. Am. Chem. Soc.* **2013**, *135*, 19268–19274.

[105] C. Legein, F. Fayon, C. Martineau, M. Body, J.-Y. Buzaré, D. Massiot, E. Durand, A. Tressaud, A. Demourgues, O. Péron, B. Boulard. ^{19}F High Magnetic Field NMR Study of β-ZrF_4 and CeF_4: From Spectra Reconstruction to Correlation between Fluorine Sites and ^{19}F Isotropic Chemical Shifts. *Inorg. Chem.* **2006**, *45*, 10636–10641.

[106] M. Biswal, M. Body, C. Legein, A. Sadoc, F. Boucher. NbF_5 and TaF_5: Assignment of ^{19}F NMR resonances and chemical bond analysis from GIPAW calculations. *J. Solid State Chem.* **2013**, *207*, 208–217.

[107] M. Murakami, Y. Noda, K. Takegoshi. Terminal and bridging fluorine ligands in TiF_4 as studied by ^{19}F NMR in solids. *Solid State Nucl. Magn. Reson.* **2019**, *101*, 82–88.

[108] N. F. Ramsey. Magnetic shielding of nuclei in molecules. *Physica* **1951**, *17*, 303–307.

[109] A. Saika, C. P. Slichter. A Note on the Fluorine Resonance Shifts. *J. Chem. Phys.* **1954**, *22*, 26–28.

[110] A. J. Pell, G. Pintacuda, C. P. Grey. Paramagnetic NMR in solution and the solid state. *Prog. Nucl. Magn. Reson. Spectrosc.* **2019**, *111*, 1–271.

[111] E. Garribba, G. Micera, D. Sanna, L. Strinna-Erre. The Cu(II)-2,2'-bipyridine system revisited. *Inorg. Chim. Acta* **2000**, *299*, 253–261.

[112] M. L. Nisbet, I. M. Pendleton, G. M. Nolis, K. J. Griffith, J. Schrier, J. Cabana, A. J. Norquist, K. R. Poeppelmeier, *Machine-learning-assisted Synthesis of Polar Racemates*, **2020**. DOI: 10.18126/VNHJ-JAZ5.

[113] B. Blaiszik, K. Chard, J. Pruyne, R. Ananthakrishnan, S. Tuecke, I. Foster. The Materials Data Facility: Data Services to Advance Materials Science Research. *JOM* **2016**, *68*, 2045–2052.

[114] B. Blaiszik, L. Ward, M. Schwarting, J. Gaff, R. Chard, D. Pike, K. Chard, I. Foster. A data ecosystem to support machine learning in materials science. *MRS Communications* **2019**, *9*, 1125–1133, Publisher: Cambridge University Press.

[115] F. M. F. de Groot, M. Grioni, J. C. Fuggle, J. Ghijsen, G. A. Sawatzky, H. Petersen. Oxygen 1*s* x-ray-absorption edges of transition-metal oxides. *Phys. Rev. B* **1989**, *40*, 5715–5723.

[116] E. I. Solomon, B. Hedman, K. O. Hodgson, A. Dey, R. K. Szilagyi. Ligand K-edge X-ray absorption spectroscopy: covalency of ligand–metal bonds. *Coord. Chem. Rev.* **2005**, 33.

[117] T. Glaser, B. Hedman, K. O. Hodgson, E. I. Solomon. Ligand K-Edge X-ray Absorption Spectroscopy: A Direct Probe of Ligand-Metal Covalency. *Acc. Chem. Res.* **2000**, *33*, 859–868.

[118] F. de Groot, A. Kotani, *Core Level Spectroscopy of Solids*, Vol. 6 of *Advances in Condensed Matter Science*, CRC Press, **2008**.

[119] A. S. Vinogradov, A. Y. Dukhanyakov, V. Ipatov, D. Onopko, A. Pavlychev, S. Titov. Fine structure of x-ray absorption of the $(TiF_6)^{2-}$ radical. *Sov. Phys. Solid State* **1982**, *24*, 803.

[120] A. S. Vinogradov, S. I. Fedoseenko, D. V. Vyalikh, S. L. Molodtsov, V. K. Adamchuk, C. Laubschat, G. Kaindl. High resolution F1s absorption spectra of solid fluorides of 3d elements. *Opt. Spectrosc.* **2002**, *93*, 862–869.

[121] A. Vinogradov, S. Fedoseenko, D. Vyalikh, S. L. Molodtsov, V. K. Adamchuk, C. Laubschat, G. Kaindl. F 1s absorption study of hybridization and collapse of 3d electronic states of first-row transition-metal fluorides. *BESSY Annual Report* **2001**, 168.

[122] R. A. Levenson, R. J. G. Dominguez. Crystal field approach to pentagonal-bipyramidal seven-coordinate complexes. Electronic structure of heptacyanovanadate(III). *Inorg. Chem.* **1973**, *12*, 2342–2345.

[123] G. Lucovsky, C. Fulton, Y. Zhang, Y. Zou, J. Luning, L. Edge, J. Whitten, R. Nemanich, H. Ade, D. Schlom, V. Afanase'v, A. Stesmans, S. Zollner, D. Triyoso, B. Rogers. Conduction band-edge States associated with the removal of d-state degeneracies by the Jahn-Teller effect. *IEEE Trans. Device Mater. Relib.* **2005**, *5*, 65–83.

[124] X. Zhao, S. Huang, Y. Liu, J. Li, W. Zhu. Effects of noncovalent interactions on the impact sensitivity of HNS-based cocrystals: A DFT study. *Cryst. Growth Des.* **2018**.

[125] T. Chen, M. Li, J. Liu. π–π Stacking Interaction: A Nondestructive and Facile Means in Material Engineering for Bioapplications. *Cryst. Growth Des.* **2018**, *18*, 2765–2783.

[126] S. Datta, M. L. Saha, P. J. Stang. Hierarchical Assemblies of Supramolecular Coordination Complexes. *Acc. Chem. Res.* **2018**, *51*, 2047–2063.

[127] T. Steiner. The Hydrogen Bond in the Solid State. *Angew. Chem. Int. Ed.* **2002**, *41*, 48–76.

[128] B.-H. Ye, M.-L. Tong, X.-M. Chen. Metal-organic molecular architectures with 2,2'-bipyridyl-like and carboxylate ligands. *Coord. Chem. Rev.* **2005**, *249*, 545–565.

[129] Y. Ma, A. Zhang, C. Zhang, D. Jiang, Y. Zhu, C. Zhang. Crystal Packing of Low-Sensitivity and High-Energy Explosives. *Cryst. Growth Des.* **2014**, *14*, 4703–4713.

[130] C.-S. Lim, J. Jankolovits, J. W. Kampf, V. L. Pecoraro. Chiral Metallacrown Supramolecular Compartments that Template Nanochannels: Self-Assembly and Guest Absorption. *Chem. Asian J.* **2010**, *5*, 46–49.

[131] E. Melnic, E. B. Coropceanu, O. V. Kulikova, A. V. Siminel, D. Anderson, H. J. Rivera-Jacquez, A. E. Masunov, M. S. Fonari, V. C. Kravtsov. Robust Packing Patterns and Luminescence Quenching in Mononuclear [Cu(II)(phen)$_2$] Sulfates. *J. Phys. Chem. C* **2014**, *118*, 30087–30100.

[132] J. Breu, H. Domel, A. Stoll. Racemic Compound Formation versus Conglomerate Formation with $[M(bpy)_3](PF_6)_2$ (M = Ni, Zn, Ru); Molecular and Crystal Structures. *Eur. J. Inorg. Chem.* **2000**, *2000*, 2401–2408.

[133] J. Breu, H. Domel, P.-O. Norrby. Racemic Compound Formation versus Conglomerate Formation with $[M(bpy)_3](PF_6)_2$ (M = Ni, Zn, Ru); Lattice Energy Minimisations and Implications for Structure Prediction. *Eur. J. Inorg. Chem.* **2000**, *2000*, 2409–2419.

[134] C. A. Hunter, J. K. M. Sanders. The nature of .pi.-.pi. interactions. *J. Am. Chem. Soc.* **1990**, *112*, 5525–5534.

[135] C. A. Hunter. Quantifying Intermolecular Interactions: Guidelines for the Molecular Recognition Toolbox. *Angew. Chem. Int. Ed.* **2004**, *43*, 5310–5324.

[136] G. V. Janjić, P. V. Petrović, D. B. Ninković, S. D. Zarić. Geometries of stacking interactions between phenanthroline ligands in crystal structures of square-planar metal complexes. *J. Mol. Model.* **2011**, *17*, 2083–2092.

[137] P. V. Petrović, G. V. Janjić, S. D. Zarić. Stacking Interactions between Square-Planar Metal Complexes with 2,2'-Bipyridine Ligands. Analysis of Crystal Structures and Quantum Chemical Calculations. *Cryst. Growth Des.* **2014**, *14*, 3880–3889.

[138] H. Nakai, Y. Deguchi. The Crystal Structure of Monoaquobis(1,10-phenanthroline)copper(II) Nitrate, $[Cu(H_2O)(phen)_2](NO_3)_2$. *Bull. Chem. Soc. Jpn.* **1975**, *48*, 2557–2560.

[139] H. Nakai, Y. Noda. The Crystal Structure of Monoaquabis(1,10-phenanthroline)copper(II) Tetrafluoroborate $[Cu(H_2O)(phen)_2](BF_4)_2$. *Bull. Chem. Soc. Jpn.* **1978**, *51*, 1386–1390.

[140] G. Murphy, C. Murphy, B. Murphy, B. Hathaway. Crystal structures, electronic properties and structural pathways of two $[Cu(phen)_2(OH_2)][Y]_2$ complexes (phen = 1,10-phenanthroline, Y = $CF_3SO_3^-$ or ClO_4^-). *J. Chem. Soc., Dalton Trans.* **1997**, 2653–2660.

[141] *CrysAlisPro; Rigaku Oxford Diffraction/Agilent Technologies UK Ltd: Yarnton, England*, **2019**.

[142] C. R. Groom, I. J. Bruno, M. P. Lightfoot, S. C. Ward. The Cambridge Structural Database. *Acta Crystallogr., Sect. B: Struct. Sci., Cryst. Eng. Mater.* **2016**, *72*, 171–179.

[143] M. D. Donakowski, R. Gautier, J. Yeon, D. T. Moore, J. C. Nino, P. S. Halasyamani, K. R. Poeppelmeier. The Role of Polar, Lamdba (Λ)-Shaped Building Units in Noncentrosymmetric Inorganic Structures. *J. Am. Chem. Soc.* **2012**, *134*, 7679–7689.

[144] Y. Shi, B. B. Toms, N. Dixit, N. Kumari, L. Mishra, J. Goodisman, J. C. Dabrowiak. Cytotoxicity of Cu(II) and Zn(II) 2,2'-Bipyridyl Complexes: Dependence of IC50 on Recovery Time. *Chem. Res. Toxicol.* **2010**, *23*, 1417–1426, Publisher: American Chemical Society.

[145] M.-M. Yu, Y.-N. Zhang, L.-H. Wei. Aquabis(2,2-bipyridine- $\kappa^2 N$, N')copper(II) bis(tetrafluoridoborate). *Acta Crystallographica Section E Structure Reports Online* **2007**, *63*, m2380–m2380.

[146] A. Adamski, M. Osińska, M. Kubicki, Z. Hnatejko, G. Consiglio, V. Patroniak. Molecular Switching of Copper Complexes with Quaterpyridine. *Eur. J. Inorg. Chem.* **2017**, *2017*, 859–872.

[147] R. Gautier, K. R. Poeppelmeier. Packing of Helices: Is Chirality the Highest Crystallographic Symmetry? *Crystals* **2016**, *6*, 106.

[148] P. Nugent, V. Rhodus, T. Pham, B. Tudor, K. Forrest, L. Wojtas, B. Space, M. Zaworotko. Enhancement of CO_2 selectivity in a pillared pcu MOM platform through pillar substitution. *Chem. Commun.* **2013**, *49*, 1606–1608.

[149] P. M. Björemark, J. Jönsson, M. Håkansson. Absolute Asymmetric Synthesis: Viedma Ripening of $[Co(bpy)_3]^{2+}$ and Solvent-Free Oxidation to $[Co(bpy)_3]^{3+}$. *Chem. Eur. J.* **2015**, *21*, 10630–10633.

[150] L. Wang, X.-Y. Yang, W. Huang. Tris(2,2'-bipyridyl-κ^2N,N')copper(II) hexafluoridophosphate. *Acta Cryst E* **2007**, *63*, m835–m836.

[151] N. Kundu, D. Mandal, M. Chaudhury, E. R. T. Tiekink. Luminescence characteristics and X-ray crystal structure of $[Cd(bipy)_3][PF_6]_2$ (bipy = 2,2'-bipyridine). *Appl. Organomet. Chem.* **2005**, *19*, 1268–1270.

[152] H. Yamamoto, S. Katogi, T. Watanabe, H. Sato, S. Miyata, T. Hosomi. New molecular design approach for noncentrosymmetric crystal structures: Lambda (Λ)-shaped molecules for frequency doubling. *Appl. Phys. Lett.* **1992**, *60*, 935–937.

[153] X. T. Tao, T. Watanabe, S. Shimoda, D. C. Zou, H. Sato, S. Miyata. .LAMBDA.-Type Main-Chain Polymers for Second Harmonic Generation. *Chem. Mater.* **1994**, *6*, 1961–1966.

[154] X. T. Tao, T. Watanabe, D. C. Zou, S. Shimoda, H. Usui, H. Sato, S. Miyata. Phase-matched second-harmonic generation in poled polymer waveguide based on a main chain polymer. *J. Polym. Sci., Part B: Polym. Phys.* **1995**, *33*, 2205–2210.

[155] V. Ostroverkhov, R. G. Petschek, K. D. Singer, R. J. Twieg. Λ-like chromophores for chiral non-linear optical materials. *Chem. Phys. Lett.* **2001**, *340*, 109–115.

[156] P.-H. Chang, J.-Y. Chen, H.-C. Tsai, G.-H. Hsiue. Molecular design of nonlinear optical polymer based on DCM to enhance the NLO efficiency and thermal stability. *J. Polym. Sci., Part A: Polym. Chem.* **2009**, *47*, 4937–4949.

[157] M. Holland, M. D. Donakowski, E. A. Pozzi, A. M. Rasmussen, T. T. Tran, S. E. Pease-Dodson, P. S. Halasyamani, T. Seideman, R. P. Van Duyne, K. R. Poeppelmeier. Polar Alignment of Λ-Shaped Basic Building Units within Transition Metal Oxide Fluoride Materials. *Inorg. Chem.* **2014**, *53*, 221–228.

[158] K. Alimaje, M. Liu, J. Peng, P. Zhang, X. Wang, M. Zhu, D. Wang, C. Meng. Hydrothermal synthesis, crystal structure and property of a barbell-like copper complex with $\{(\mu\text{-F})[(\mu\text{-O})_2(NbF_4)_2]\}$ as the handle bar. *Inorg. Chem. Commun.* **2011**, *14*, 1209–1211.

[159] M. L. Nisbet, Y. Wang, K. R. Poeppelmeier. Symmetry-Dependent Intermolecular π–π Stacking Directed by Hydrogen Bonding in Racemic Copper-Phenanthroline Compounds. *Crystal Growth & Design* **2021**, *21*, 552–562, Publisher: American Chemical Society.

[160] M. L. Nisbet, K. R. Poeppelmeier. Crystal structures of $[Cu(phen)H_2\ O)_3(MF_6)]\cdot H_2$ (M = Ti, Zr, Hf) and $[Cu(phen)(H_2O)_2F_2[HfF_6]\cdot H_2O$. *Acta Crystallogr., Sect. E: Crystallogr. Commun.* **2021**, *77*, 165–170.

[161] V. V. Ghazaryan, M. Fleck, A. M. Petrosyan. Hexafluorosilicates of alanine. *Z. Kristallogr.* **2012**, *227*, 646–655.

[162] I. J. Bruno, J. C. Cole, P. R. Edgington, M. Kessler, C. F. Macrae, P. McCabe, J. Pearson, R. Taylor. New software for searching the Cambridge Structural Database and visualizing crystal structures. *Acta Crystallogr B Struct Sci* **2002**, *58*, 389–397.

[163] T. Pilati, A. Forni. SYMMOL: a program to find the maximum symmetry group in an atom cluster, given a prefixed tolerance. *Journal of Applied Crystallography* **1998**, *31*, 503–504.

[164] T. Pilati, A. Forni. SYMMOL – a program to find the maximum symmetry in an atom cluster: an upgrade. *J Appl Cryst* **2000**, *33*, 417–417.

[165] B. Busson, M. Kauranen, C. Nuckolls, T. J. Katz, A. Persoons. Quasi-Phase-Matching in Chiral Materials. *Phys. Rev. Lett.* **2000**, *84*, 79–82.

[166] Y. He, I. M. Vishik, M. Yi, S. Yang, Z. Liu, J. J. Lee, S. Chen, S. N. Rebec, D. Leuenberger, A. Zong, C. M. Jefferson, R. G. Moore, P. S. Kirchmann, A. J. Merriam, Z.-X. Shen. Invited Article: High resolution angle resolved photoemission with tabletop 11 eV laser. *Rev. Sci. Instrum.* **2016**, *87*, 011301.

[167] J. Zhou, H. Wu, H. Yu, S. Jiang, Z. Hu, J. Wang, Y. Wu, P. S. Halasyamani. $BaF_2TeF_2(OH)_2$: A UV Nonlinear Optical Fluorotellurite Material Designed by Band-Gap Engineering. *J. Am. Chem. Soc.* **2020**, *142*, 4616–4620.

[168] M. Mutailipu, M. Zhang, Z. Yang, S. Pan. Targeting the Next Generation of Deep-Ultraviolet Nonlinear Optical Materials: Expanding from Borates to Borate Fluorides to Fluorooxoborates. *Acc. Chem. Res.* **2019**, *52*, 791–801.

[169] F. Ding, W. Zhang, M. L. Nisbet, W. Zhang, P. S. Halasyamani, Z. Yang, S. Pan, K. R. Poeppelmeier. $NaRb_3B_6O_9(OH)_3(HCO_3)$: A Borate-Bicarbonate Nonlinear Optical Material. *Inorg. Chem.* **2020**, *59*, 759–766.

[170] H. Yu, M. L. Nisbet, K. R. Poeppelmeier. Assisting the Effective Design of Polar Iodates with Early Transition-Metal Oxide Fluoride Anions. *J. Am. Chem. Soc.* **2018**, *140*, 8868–8876.

APPENDIX A

$[Cu(phen)(OH)]_2[ZrF_6]\cdot 2H_2O$, a One-Dimensional Coordination Polymer with Potential Spin Frustration

$[Cu(phen)(OH)]_2[ZrF_6]\cdot 2H_2O$ crystallizes in the space group $P\bar{1}$. The structure contains infinite one-dimensional chains composed of repeating $Cu(phen)(OH)^+$ complexes linked through bridging hydroxide groups to give Cu–Cu distances of 2.969 and 3.186 Å. Free water molecules and isolated ZrF_6^{2-} anions occupy the spaces in between adjacent chains, which do not participate in $\pi - \pi$ stacking with one another. Along the chain direction, bridging hydroxide groups form alternating hydrogen bonds to ZrF_6^{2-} anions and free water molecules. The ZrF_6^{2-} anions also form hydrogen bonds to free water molecules. Within each chain, the $Cu(phen)(OH)^+$ units participate in two parallel displaced $\pi - \pi$ stacking interactions (interplanar angle: 0.47°, phenyl-pyridine distance of 3.506 Å). Given the geometry of chains within $[Cu(phen)(OH)]_2[ZrF_6]\cdot 2H_2O$, which contain triangular arrangements of paramagnetic Cu(II) centers, this compound may display magnetic frustration and therefore is an attractive target for investigation of its magnetic ordering, or lack thereof, at low temperature.

$[Cu(phen)(OH)]_2[ZrF_6]\cdot 2H_2O$ was synthesized via the hydrothermal pouch method using 1.69 mmol CuO, 1.69 mmol ZrO_2, 2.56 mmol 1,10-phenanthroline, 0.2 mL (5.5 mmol) HF(aq), and 0.9 mL (50 mmol) H_2O.

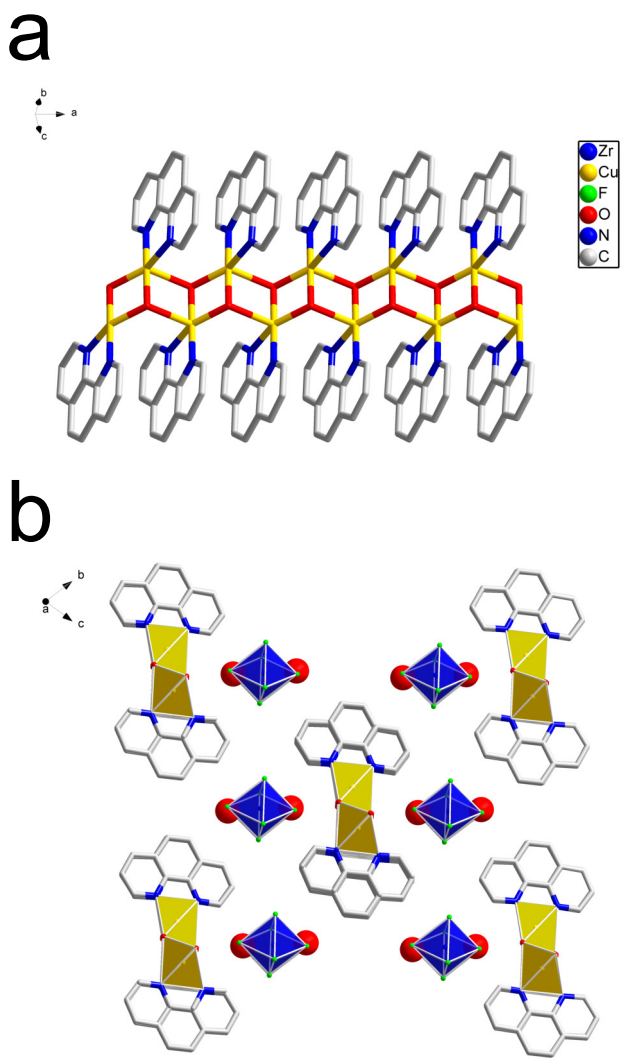

Figure A.1. (a) Chain structure of $[Cu_2(phen)_2(OH)_2][ZrF_6]\cdot 2H_2O$. (b) Packing diagram of $[Cu(phen)(OH)]_2[ZrF_6]\cdot 2H_2O$.

Table A.1. Crystallographic Data for $[Cu(phen)(OH)]_2[ZrF_6]\cdot 2H_2O$

Empirical formula	$C_{24}H_{22}Cu_2F_6N_4O_4Zr$
Formula weight	762.75
Temperature/K	99.98
Crystal system	triclinic
Space group	$P\bar{1}$
a/Å	7.2733(4)
b/Å	13.0950(7)
c/Å	13.7629(7)
α/°	73.7400(10)
β/°	83.5790(10)
γ/°	85.0500(10)
Volume/Å^3	1248.43(12)
Z	2
ρ_{calc} / g/cm^3	2.029
μ/mm^{-1}	2.185
F(000)	756
Crystal size/mm^3	0.388 × 0.199 × 0.13
Radiation	MoKα (λ = 0.71073 Å)
2θ range for data collection/°	3.096 to 60.272
Index ranges	-10 ≤ h ≤ 9, -18 ≤ k ≤ 18, -19 ≤ l ≤ 19
Reflections collected	83524
Independent reflections	7230 [R_{int} = 0.0217, R_{sigma} = 0.0110]
Data/restraints/parameters	7230/0/458
Goodness-of-fit on F^2	1.226
Final R indexes [I≥2σ(I)]	R_1 = 0.0303, wR_2 = 0.0860
Final R indexes [all data]	R_1 = 0.0323, wR_2 = 0.0868
Largest diff. peak/hole / e Å^{-3}	1.13/-0.80
CCDC number	2061418

Vita

MATTHEW L. NISBET

Department of Chemistry, Northwestern University
2145 Sheridan Road
Evanston, IL, 60208, USA

work phone	+1 (847) 491-4228	Google Scholar	Profile
work email	nisbet@u.northwestern.edu	ORCID	0000-0001-9531-9193
personal phone	+1 (931) 239-8097		
personal email	mattnisbet931@gmail.com		

EDUCATION

2016 – **Doctor of Philosophy**, Chemistry, *Northwestern University,* Evanston, IL, USA
expected March 2021

2012 – 2016 **Bachelor of Science**, Chemistry and Mathematics, *Centre College,* Danville, KY, USA
magna cum laude

RESEARCH EXPERIENCE

11/2016 – **Graduate Research Assistant**, Advisor: Kenneth R. Poeppelmeier, *Northwestern University*, Evanston, IL, USA
Thesis: Achiral Noncentrosymmetric Racemates

5/2015 – 8/2015 **NSF REU Participant**, Advisor: R. J. Hinde, *University of Tennessee, Knoxville*, Knoxville, TN, USA
Research: Modeling the potential energy surface of the Ne-HBr van der Waals dimer

6/2014 – 8/2014 **Research Assistant**, Advisor: John E. Anthony, *University of Kentucky*, Lexington, KY, USA
Research: Synthesis of organic photovoltaic materials

AWARDS

Northwestern University

2020 Donald E. Smith Award for Excellence in 300-Level Teaching

2018 Honorable Mention - NSF Graduate Research Fellowship Program

Centre College

2016 Phi Beta Kappa

2016 Rufus Preston Carter Chemistry Prize

2015 T. Hunton Rogers Memorial Scholarship Prize

2014 Analytical Chemistry Award

2014 Mathematics Program Prize

2013 General Chemistry Award

TEACHING EXPERIENCE

Northwestern University

9/2020 **Teaching Assistant Training Program – Workshop Facilitator**
Facilitated a workshop for new graduate students entitled, "Safety for Teaching Labs and Other Teaching Assignments"
Offered advice to incoming graduate students on how to prioritize safety while managing undergraduate laboratory exercises.

1/2019 – **Research Mentor**
Supervised an undergraduate student in the synthesis of novel crystalline materials.
Led a weekly ZOOM journal club during COVID-19 pandemic.

10/2019 – 12/2019 **Teaching Assistant**, Inorganic Chemistry (Chem 333)
Presented lectures on symmetry, group theory, and molecular orbital theory.
Hosted weekly office hours.
Developed course content, including lecture slides and interactive learning activities.

1/2019 – 3/2019 **Teaching Assistant**, X-ray Crystallography (Chem 432)
Answered questions about fundamental principles of crystallography and use of structure solution software.
Demonstrated collection of single crystal data for groups of students.

1/2018 – 3/2018 **Teaching Assistant**, Advanced Laboratory (Chem 350)
Developed laboratory exercises involving superconductors, metal-organic frameworks, and zeolite materials.
Provided consultation to advanced laboratory students on experimental planning and data analysis for independent research projects.

9/2016 – 3/2017 **Teaching Assistant**, General Chemistry (Chem 122, 181)
Presented pre-laboratory lectures to review experimental techniques and safety.
Graded laboratory reports and exams.

Centre College

8/2014 – 5/2016 **Teaching Assistant**, General Chemistry (Chem 131, 132, 241, & 242)
Advised students on safety information, lab technique, and concept comprehension.
Hosted weekly tutor hours.

PUBLICATIONS

1. *Crystal Structures of [Cu(Phen)(H_2O)$_3$(MF_6)] · H_2O (M = Ti, Zr, Hf) and [Cu(Phen)(H_2O)$_2$F]$_2$[HfF_6] · H_2O.* **M. L. Nisbet,** K. R. Poeppelmeier. Acta Crystallogr. E Cryst. Commun. 77, 165-170 (2021). DOI: 10.1107/S2056989021000645

2. *Crystal Structures of Three Copper(II)–2,2′-Bipyridine (Bpy) Compounds, [Cu(Bpy)$_2$(H_2O)][SiF_6] · 4H_2O, [Cu(Bpy)$_2$(TaF_6)$_2$] and [Cu(Bpy)$_3$][TaF_6]$_2$ and a Related Coordination Polymer, [Cu(Bpy)(H_2O)$_2$$SnF_6$]$_n$.* **M. L. Nisbet**, E. Hiralal, K. R. Poeppelmeier. Acta Crystallogr. E Cryst. Commun. 77, 158–164 (2021). DOI: 10.1107/S2056989021000633.

3. *Symmetry-Dependent Intermolecular π-π Stacking Directed by Hydrogen Bonding in Racemic Copper-Phenanthroline Compounds.* **M. L. Nisbet**, Y. Wang, K. R. Poeppelmeier. Cryst. Growth Des., 21, 552-562 (2021). DOI: 10.1021/acs.cgd.0c01355

4. *Multimodal Structure Solution with ^{19}F NMR Crystallography of Spin Singlet Molybdenum Oxyfluorides*, F. Ding, K. J. Griffith, C. P. Kocer, R. J. Saballos, Y. Wang, C. Zhang, **M. L. Nisbet,** A. J. Morris, J. M. Rondinelli, K. R. Poeppelmeier, J. Am. Chem. Soc., 142, 12288-12298 (2020). DOI: 10.1021/jacs.0c04019

5. *$LiIn_2SbO_6$: A new Rutile-Related Structure-type with Ion Transport Pathways*, S. Flynn, S. Sanghvi, **M. L. Nisbet**, K. J. Griffith, W. Zhang, P. S. Halasyamani, S. M. Haile, K. R. Poeppelmeier, Chem. Mater., 32, 4785–4794 (2020). DOI: 10.1021/acs.chemmater.0c01491

6. *Machine-learning Assisted Synthesis of Polar Racemates*, **M. L. Nisbet,** I. Pendleton, G. Nolis, K. J. Griffith, J. Schrier, J. Cabana, A. J. Norquist, K. R. Poeppelmeier, J. Am. Chem. Soc., 142, 7555–7566 (2020). DOI: 10.1021/jacs.0c01239

7. *Periodic Tendril Perversion and Helices in the $AMoO_2F_3$ (A = K, Rb, NH_4, Tl) Family*, J. C. Hancock, **M. L. Nisbet**, W. Zhang, P. S. Halasyamani, K. R. Poeppelmeier, J. Am. Chem. Soc. 142, 6375–6380 (2020). DOI: 10.1021/jacs.0c01218

8. *$NaRb_3B_6O_9(OH)_3(HCO_3)$: A Borate-Bicarbonate Nonlinear Optical Material*, F. Ding, W. Zhang, **M. L. Nisbet**, W. Zhang, P. S. Halasyamani, Z. Yang, S. Pan, K. R. Poeppelmeier, Inorg. Chem., 59, 759–766 (2020). DOI: 10.1021/acs.inorgchem.9b03026

9. *Why Some Noncentrosymmetric Borates Do Not Make Good Nonlinear Optical Materials: A Case Study with $K_3B_5O_8(OH)_2$,* F. Ding, **M. L. Nisbet,** W. Zhang, P. S. Halasyamani, L. Chai, K. R. Poeppelmeier, Inorg. Chem., 57, 11801–11808 (2018). DOI: 10.1021/acs.inorgchem.8b01965

10. *Assisting the Effective Design of Polar Iodates with Early Transition-Metal Oxide Fluoride Anions*, H. Yu, **M. L. Nisbet,** K. R. Poeppelmeier, J. Am. Chem. Soc., 140, 8868–8876 (2018). DOI: 10.1021/jacs.8b04762

11. *Syntheses, Structures, and Properties of Non-Centrosymmetric Quaternary Tellurates $BiMTeO_6$ (M = Al, Ga)*, F. Ding, **M. L. Nisbet,** H. Yu, W. Zhang, L. Chai, P. S. Halasyamani, P. K. R. Poeppelmeier, Inorg. Chem., 57, 7950–7956 (2018). DOI: 10.1021/acs.inorgchem.8b01087

PRESENTATIONS

1. *Machine-learning-assisted Synthesis of Polar Racemates,* ACS National Meeting, Philadelphia, PA (March 23, 2020 – meeting cancelled owing to COVID-19)
   Oral Presentation

2. *Second-Order Jahn-Teller Effects in Early Transition Metal Octahedra*, Basolo-Ibers-Pearson Inorganic Chemistry Seminar, Evanston, IL (February 21, 2020)
   Oral Presentation

3. *Pseudo-Jahn-Teller Effects in the Synthesis of Polar Racemates,* North American Solid State Chemistry Conference, Golden, CO (July 31, 2019)
   Poster Presentation

4. *Do Weakly Polar Anions Break Inversion Symmetry in Racemates?*, ACS National Meeting, Orlando, FL (April 2, 2019)
   Poster Presentation

5. *Breaking Inversion Symmetry in Racemates*, Basolo-Ibers-Pearson Inorganic Chemistry Seminar, Evanston, IL (January 11, 2019)
Oral Presentation

6. *Hydrothermal Synthesis of Non-centrosymmetric Racemates,* Gordon Research Conference for Crystal Engineering, Newry, ME (June 24, 2018)
Poster Presentation

7. *Optically Active Noncentrosymmetric Materials from Racemic Units,* Basolo-Ibers-Pearson Inorganic Chemistry Seminar, Evanston, IL (February 12, 2018)
Oral Presentation

SERVICE & OUTREACH

2/2017 – **Science in the Classroom**, Volunteer, *Hayt Elementary School*, Chicago, IL, USA
Teach science lessons to 3rd and 4th grade students at Hayt Elementary School with other graduate students.
Lead small groups of 4-5 students through hands-on learning exercises that demonstrate new ideas and help students engage with unfamiliar concepts.

8/2018 – 7/2019 **Phi Lambda Upsilon**, Treasurer, *Northwestern University*, Evanston, IL, USA
Developed an organizational budget.
Tracked expenses for programs including career panels and social events.

9/2017 – 5/2018 **Mentorship Opportunities for Research Engagement**, Volunteer, *Niles West High School*, Skokie, IL, USA
Collaborated with a high school student to develop an independent research project, including guidance for planning and presenting the research.
Discussed future educational plans and STEM career paths with high school students from traditionally underserved communities.

SKILLS

Laboratory

X-ray crystallography (single crystal and powder)
Hydrothermal crystal growth
Thermal analysis (TGA/DTA)
X-ray absorption spectroscopy
Transmission electron microscopy
Vibrational spectroscopy
NMR spectroscopy

Computer

Adobe Illustrator
Apex3
ConQuest
CrysAlisPro
Diamond
Java
Mathematica
MATLAB
MDI Jade
Mercury
Microsoft Office
Olex2
Python
Scikit-learn